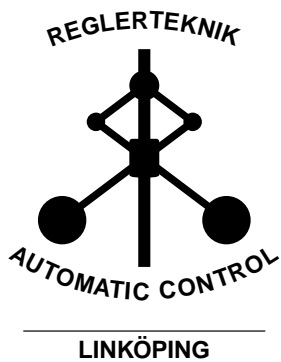


Linköping studies in science and technology. Thesis.
No. 1581

Localization using Magnetometers and Light Sensors

Niklas Wahlström



Division of Automatic Control
Department of Electrical Engineering
Linköping University, SE-581 83 Linköping, Sweden
<http://www.control.isy.liu.se>
nikwa@isy.liu.se

Linköping 2013

This is a Swedish Licentiate's Thesis.

Swedish postgraduate education leads to a Doctor's degree and/or a Licentiate's degree.

A Doctor's Degree comprises 240 ECTS credits (4 years of full-time studies).

A Licentiate's degree comprises 120 ECTS credits,
of which at least 60 ECTS credits constitute a Licentiate's thesis.

Linköping studies in science and technology. Thesis.

No. 1581

Localization using Magnetometers and Light Sensors

Niklas Wahlström

nikwa@isy.liu.se

www.control.isy.liu.se

Department of Electrical Engineering

Linköping University

SE-581 83 Linköping

Sweden

ISBN 978-91-7519-663-3

ISSN 0280-7971

LIU-TEK-LIC-2013:15

Copyright © 2013 Niklas Wahlström

Printed by LiU-Tryck, Linköping, Sweden 2013

Till Nicky!

Abstract

Localization is essential in a variety of applications such as navigation systems, aerospace and surface surveillance, robotics and animal migration studies to mention a few. There are many standard techniques available, where the most common are based on information from satellite or terrestrial radio beacons, radar networks or vision systems. In this thesis, two alternative techniques are investigated.

The first localization technique is based on one or more magnetometers measuring the induced magnetic field from a magnetic object. These measurements depend on the position and the magnetic signature of the object and can be described with models derived from the electromagnetic theory. For this technology, two applications have been analyzed. The first application is traffic surveillance, which has a high need for robust localization systems. By deploying one or more magnetometer in the vicinity of the traffic lane, vehicles can be detected and classified. These systems can be used for safety purposes, such as detecting wrong-way drivers on highways, as well as for statistical purposes by monitoring the traffic flow. The second application is indoor localization, where a mobile magnetometer measures the stationary magnetic field induced by magnetic structures in indoor environments. In this work, models for such magnetic environments are proposed and evaluated.

The second localization technique uses light sensors measuring light intensity during day and night. After registering the time of sunrise and sunset from this data, basic formulas from astronomy can be used to locate the sensor. The main application is localization of small migrating animals. In this work, a framework for localizing migrating birds using light sensors is proposed. The framework has been evaluated on data from a common swift, which during a period of ten months was equipped with a light sensor.

Populärvetenskaplig sammanfattning

Förmågan att kunna bestämma var ett objekt befinner sig är viktigt inom många olika tillämpningar, till exempel inom flyg- och sjöbevakning, robotik och studier av djurs flyttvägar, för att nämna några. Det är speciellt önskvärt att kunna utföra denna positionering utan mänsklig inblandning, antingen för att kunna positionera objekt som en människa inte skulle klara av att göra, eller för att effektivisera arbetet. För att automatiskt bestämma en position behövs sensorer, som mäter olika saker i dess omgivning och omvandlar detta till en elektrisk signal. Med ett datorprogram kan denna elektriska signal i sin tur sedan omvandlas till en position. Det finns många standardteknologier tillgängliga som använder sig av olika typer av sensorer som mäter olika saker. De vanligaste är baserade på satellitnavigering (GPS), radiovågor, radar och kameror. I denna avhandling har två alternativa teknologier undersökts som i vissa tillämpningar har olika fördelar gentemot standardteknologierna.

Den första teknologin för att positionera ett objekt är baserad på en eller flera sensorer som känner av magnetfältet från objekt som innehåller mycket metall, till exempel fordon. Från detta magnetfält kan man bestämma position och även storlek på objektet. Med denna teknologi som grund har två tillämpningar analyserats. Den första tillämpningen är trafikövervakning, där det finns ett stort behov av teknologi som kan bestämma position på bilar. Genom att placera ut en eller flera sensorer längs vägrenen kan man känna av bilar som kommer i närheten. Dessa system kan användas för säkerhetsändamål, som att varna för bilar som kör i fel riktning på motorvägar, eller för statistiska ändamål genom att övervaka trafikflödet. Den andra tillämpningen handlar om att bestämma position för ett objekt i en inomhusmiljö. I många byggnader finns det många objekt som innehåller metall. Dessa objekt omges av ett magnetfält. Genom att i en inomhusmiljö vandra runt med en sensor, så kommer den att känna av olika starka magnetfält beroende på var i byggnaden man befinner sig. I denna avhandling kommer vi undersöka matematiska modeller för att beskriva sådana magnetiska objekt.

Den andra teknologin använder ljussensorer för att studera till vilka områden som flyttfåglar flyger. Fågeln utrustas med en ljussensor som mäter ljusstyrka under hela dygnet. Därefter släpps fågeln iväg och förhoppningsvis hittar man den ett år senare igen så att all information från sensorn kan analyseras. Från dessa mätningar kan man i efterhand beräkna vid vilken tidpunkt som soluppgången och solnedgången har inträffat. Därefter kan fågels flyttväg bestämmas med hjälp av formler från astronomin. I detta arbete föreslås en metod för hur denna information kan analyseras. Metoden har utvärderats på data från en tornseglare som under en period på tio månader flyttat till Afrika och sedan tillbaka till Sverige igen.

Acknowledgments

First of all I want to thank my supervisor Prof. Fredrik Gustafsson for your guidance and encouragement. Your efficiency and source of ideas are really amazing. Not only your scientific skills are impressive. Also your entrepreneurial mindset inspires!

Dr. Thomas Schön has lately been a great source of inspiration for my work. I appreciate your genuine interest in teaching and research. Your feedback has been really encouraging. Even many fruitful discussions with Dr. Emre Özkan have given me new insights and ideas. I want to thank you both! I also want to thank Lic. Roland Hostettler for the collaboration we have had for the last couple of years.

I joined the RT-corridor's everyday life already with my master's thesis. This gave me inspiration to continue. Therefore, I am very grateful that Prof. Fredrik Gustafsson and Prof. Lennart Ljung invited me to be part of the Automatic Control group. Since then, the group has been skillfully headed by Prof. Svante Gunnarsson, the division coordinator Ninna Stensgård and her predecessor Åsa Karmelind. I also want to acknowledge the Swedish Foundation for Strategic Research, SSF, for their financial support under the project Cooperative Localization in the program on Software Intensive Systems.

In the aforementioned RT-corridor many colleagues are contributing to the truly enjoyable working atmosphere. I appreciate passing by the room of Manon Kok and Lic. Zoran Sjanic for both scientific and entertaining discussions, and the boardgames events at Tohid Ardeshiri's and Michael Roth's places are always a treat. Thank you Jonas Linder for every time I have had the pleasure beating you at badminton and Lic. Sina Khoshfetrat Pakazad for organizing cheerful evenings. I also appreciate all help that I have received from Lic. Daniel Petersson regarding computer related issues. I want to thank my roommates Marek Syldatk and Dr. Mehmet Burak Guldogan for pleasant company, and the bridge-group consisting of Prof. Anders Hansson, Tohid Ardeshiri and Manon Kok for all playful Wednesday-evenings. Special thanks also go to Prof. Fredrik Gustafsson, Dr. Thomas Schön, Dr. Emre Özkan, Manon Kok, Jonas Linder and Linus Envall who have been proofreading various parts of this thesis.

Finally, I would like to show my deepest gratitude to my family. Without your support and encouragement this would not have been possible. Nicky, thank you for all your love and patience!

*Linköping, February 2013
Niklas Wahlström*

Contents

Notation	xv
I Background	
1 Introduction	3
1.1 Standard Localization Techniques	4
1.1.1 Existing Techniques	4
1.1.2 Sensor Fusion	5
1.2 Alternative Localization Techniques	6
1.2.1 Magnetic Localization	6
1.2.2 Light Levels	7
1.3 Applications and Collaborations	9
1.3.1 Traffic Surveillance	9
1.3.2 Interaction in Public Environments	10
1.3.3 Indoor Localization and Mapping	11
1.3.4 Bird Localization	12
1.4 Thesis Outline	12
1.5 Other Publications	16
1.6 Contributions	16
2 Electromagnetic Theory	17
2.1 Maxwell's Equations	17
2.2 Quasi-Static Approximation	18
2.3 Magnetic Dipole Moment	19
2.4 Magnetization	20
2.5 Magnetizing Field	21
2.6 Magnetic Materials	22
2.6.1 Soft Iron	22
2.6.2 Hard Iron	23
2.7 Summary and Connections	23
3 Astronomy	25

3.1	Kepler's Laws	25
3.2	Spherical Astronomy	26
3.2.1	Spherical Geometry	27
3.2.2	Coordinate Systems	28
3.3	Time	34
3.4	Simplified Model	34
3.5	Summary and Connections	35
4	Concluding Remarks	37
4.1	Conclusions	37
4.2	Future Work	38
A	Dipole Derivation	41
	Bibliography	43

II Publications

A	Magnetometer Modeling and Validation for Tracking Metallic Targets	49
1	Introduction	51
2	Theoretical Sensor Model	53
2.1	Single Sensor Point Target Model	53
2.2	Multiple Sensor Model	54
2.3	Extended Target Model	54
2.4	Uniformly Linear Array of Dipoles	56
2.5	Target Orientation Dependent Model	56
2.6	General Sensor Model	58
3	Constant Velocity Tracking Model	59
3.1	Sensor Model for Constant Velocity	59
3.2	Anderson function expansion for constant velocity	60
3.3	Comparison	62
4	Magnetometer Potential for Localization and Tracking	62
4.1	Single Sensor Observability	63
4.2	Single Sensor Observability with Prior Information	65
4.3	Multi Sensor Observability	66
4.4	Comparison	67
4.5	Cramér Rao Lower Bound	67
5	Estimation	68
5.1	Sensor Noise Covariance	68
5.2	Parameter Estimation using Constant Velocity Model	68
5.3	Model Validation	69
5.4	State and Parameter Estimation	69
6	Sensor Model Validation	70
6.1	Experimental Setup	70
6.2	Sensor Noise Covariance	70
6.3	Point Target Model Validation	71

6.4	Extended Target Model Validation	72
6.5	Validation of Direction Dependent Target Model	74
7	Conclusions	78
	Bibliography	79
B Classification of Driving Direction in Traffic Surveillance using Magnetometers		81
1	Introduction	83
2	Signal Model	85
3	Likelihood Test	87
3.1	Single Sensor	87
3.2	Sensor Fusion	89
4	Integral Feature	89
4.1	Measurement Data Example	89
4.2	Simulated Example	90
4.3	Deterministic Analysis	91
5	Cross-Correlation based Classifier	93
5.1	Cross-Correlation with Lag One	93
5.2	Cross-Correlation with Arbitrary Lag	95
5.3	Optimizing the Lag	98
5.4	Multiple Sensors	98
6	Simulation	99
6.1	Estimate and Variance Estimate	99
6.2	Dependency of P_E on SNR and p	99
6.3	Comparison with Likelihood Test	100
7	Experimental Results and Discussion	102
7.1	Experiment Setup	102
7.2	Results	103
7.3	Discussion	107
8	Conclusions	108
A	Distributions	108
B	Fusion of Conditional Bernoulli Random Variables	110
	Bibliography	111
C Modeling Magnetic Fields using Gaussian Processes		113
1	Introduction	115
2	Magnetic Fields	116
3	Gaussian Processes	118
3.1	Mean Function	119
3.2	Vector-Valued Covariance Functions	119
3.3	Regression	120
3.4	Estimating Hyperparameters	120
4	Modeling	121
5	Results	122
5.1	Simulated Experiment	122
5.2	Real World Experiment	124

6	Conclusion and Future Work	125
	Bibliography	126
D	A Voyage to Africa by Mr Swift	129
1	Introduction	131
2	Models	134
	2.1 Sunrise and Sunset Models	134
	2.2 Sensor Error Model	136
	2.3 Kinematic Model	137
3	State estimation	138
4	Results from Real World Data	140
	4.1 The data	140
	4.2 Results	142
5	Conclusion and Future Work	147
	Bibliography	150

Notation

OPERATORS

Notation	Meaning
A^T	Transpose of matrix A
$\text{tr } A$	Trace of matrix A
E	Expected value
Var	Variance
Cov	Covariance
\triangleq	Defined as
$\frac{\partial y}{\partial x}$	Partial derivative of y with respect to x

ELECTROMAGNETIC THEORY

Notation	Meaning
\mathbf{E}	Electric field, [V m^{-1}]
\mathbf{D}	Electric displacement field, [C m^{-2}]
\mathbf{B}	Magnetic field, [T]
\mathbf{H}	Magnetizing field, [A m^{-1}]
μ_0	Permeability of free space, [H m^{-1}]
ϵ_0	Permittivity of free space, [F m^{-1}]
ρ	Charge density, [C m^{-3}]
\mathbf{J}	Current density, [A m^{-2}]
\mathbf{J}_m	Magnetization current density, [A m^{-2}]
\mathbf{J}_f	Free current density, [A m^{-2}]
\mathbf{M}	Magnetization, [A m^{-1}]
\mathbf{A}	Magnetic vector potential, [A m^{-1}]
\mathbf{m}	Magnetic dipole moment, [A m^2]
$\nabla \cdot \mathbf{E}$	Divergence of vector field \mathbf{E}
$\nabla \times \mathbf{E}$	Curl of vector field \mathbf{E}

ASTRONOMY

Notation	Meaning
A	Azimuth
h	Altitude
d	Declination
α	Right ascension
β	Ecliptic latitude
λ	Ecliptic longitude
H	Local hour angle
ε	Obliquity of the ecliptic
Θ	Sidereal time
Θ_G	Sidereal time at Greenwich
Υ	Vernal equinox
f	True anomaly
E	Eccentric anomaly
M	Mean anomaly
e	Orbital eccentricity
P	Orbital period

ESTIMATION

Notation	Meaning
\mathbf{x}	State
\mathbf{y}	Measurement
\mathbf{u}	Input
\mathbf{w}	Process noise
\mathbf{e}	Measurement noise
T	Sampling time
$\mathcal{N}(\cdot, \cdot)$	Gaussian distribution with mean and covariance
$\mathcal{GP}(\cdot, \cdot)$	Gaussian process with mean and covariance function
P	State covariance matrix
Q	Process noise covariance matrix
R	Measurement noise covariance matrix
\mathcal{I}	Fischer information matrix

GEOMETRY AND DYNAMICS

Notation	Meaning
\mathbf{r}	Position
\mathbf{v}	Velocity
x	Cartesian x -coordinate
y	Cartesian y -coordinate
z	Cartesian z -coordinate

ABBREVIATIONS

Abbreviation	Meaning
GNSS	Global navigation satellite system
GPS	Global positioning system
WLAN	Wireless local area networks
IMU	Inertial measurement unit
WSN	Wireless sensor network
SLAM	Simultaneous localization and mapping
CPA	Closest point of approach
SNR	Signal to noise ratio
GLRT	Generalized likelihood ratio test
PDF	Probability density function
CRLB	Cramér-Rao lower bound
FIM	Fischer information matrix
BFGS	Broyden-Fletcher-Goldfarb-Shanno
GP	Gaussian process
SE	Squared exponential

Part I

Background

1

Introduction

Position is a fundamental quantity. Answering questions like *Where am I?* and *Where is it?* are important to be able to make decisions and to understand the world around us. *Localization* is the process of answering these questions in an automated fashion.

1.1 Definition (Localization). The process of automatically determining the position of an object. _____

To be able to accomplish this automatically, appropriate technology has to be used. There exist many well-established technologies such as GPS, radar and cameras, which are very well suited for certain applications. However, all technologies have their advantages and disadvantages which can be measured in terms like cost, accuracy, range, reliability, flexibility, weight and size. For some applications these technologies are unfavorable and other alternative systems exist. In this thesis, two alternative localization technologies will be investigated:

- *Magnetic localization*, i.e., localization based on the magnetic field induced by magnetic objects.
- Localization with *light levels*, i.e., localization based on sunrise and sunset events extracted from light intensity data.

All localization technologies have in common that they rely on one or more sensors providing measurements which are related to the position. An important component of such a localization technology is to describe the relation between these measurements and the position, which we do using models. Throughout this thesis, a main focus will lie on models that can be used in the two areas presented above. Before presenting the two localization technologies and their applications, a short overview of existing standard localization techniques is given.

1.1 Standard Localization Techniques

According to Deak et al. (2012), localization techniques can be categorized as either active or passive: (1) techniques requiring the object of interest to participate actively; and (2) techniques using passive localization. With active we mean that the object of interest carries a sensor collecting data which is used for the localization. In passive localization techniques these sensors are deployed in the surrounding environment. In this context, the following techniques are worth mentioning.

1.1.1 Existing Techniques

Global navigation satellite system

A *global navigation satellite system* (GNSS) is based on multiple satellites orbiting around the earth. Using a receiver, signals from the satellites can be detected and the position is determined via triangulation. The most common GNSS system is the *Global Positioning System* (GPS), which provides position information to anyone with a GPS receiver. The commercial-use receivers have an accuracy within 10 meters and are nowadays integrated in most modern smart phones.

The receiver requires a line of sight to at least four GPS satellites to work. This is a limitation, especially in indoor environments, where this sight is obscured. Due to the positioning uncertainty, the technology is also not well suited for localization in smaller volumes where higher accuracy is required. Other disadvantages are its sensitivity to jamming, the high energy consumption and high cost.

Radio

Radiolocation and *radio navigation* systems use one or more properties of electromagnetic waves emitted by a transmitter and measured by a receiver. Different setups are possible depending on how the receiver and transmitter are deployed and which type of electromagnetic waves is being transmitted. Many electromagnetic waves being used by radio positioning systems are not designed to support localization, for example signals from *Wireless Local Area Networks* (WLAN), *television broadcast* and *cellular networks*. Such technologies are common in indoor applications (Torres-Solis et al., 2010; Deak et al., 2012) and their main advantage is the reduced cost due to the use of already available infrastructure. *Ultra-wideband* is a passive radiolocation system, which has increased in popularity in indoor localization due to its high accuracy. However, the price of the system is high (Gu et al., 2009).

Radar

Radar (RADIO Detection And Ranging) is a specific radio positioning system consisting of a transmitter emitting radio waves which are reflected on objects with high electrical conductivity. The reflections are measured by a receiver which usually (but not necessarily) is situated in the same position as the transmitter.

The most common application is to localize ships, airplanes and missiles and is as such a passive system. Radars can also be used as an active localization system

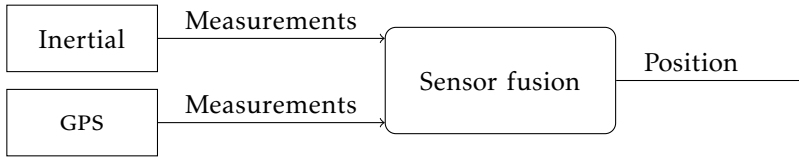


Figure 1.1: Illustration of sensor fusion between IMU and GPS for computing a position.

on ships to locate landmarks in order to determine its own position, which is investigated by Karlsson and Gustafsson (2006).

Vision

A *vision sensor* consists of an optical system providing an analog image, which is digitalized by an image sensor. By capturing sequential images from a moving object its position can be determined by preprocessing the images. As such, it is a passive system. It can also be used to localize the vision sensor itself by comparing the sequential images with each other. However, vision comes with many challenges such as occlusion, varying light conditioning and different perspectives. This makes it also sensitive to changing weather conditions.

Inertial

An *inertial measurement unit* (IMU) consists of an accelerometer and a gyroscope. The unit can be used to determine the orientation of an object as well as the position relative to a known starting point (Woodman, 2007). The position is computed by integrating the information from the two sensors. In a short period the computed position is accurate. However, due to this integration, the accuracy will decrease with time if not aided with another system providing absolute position information.

1.1.2 Sensor Fusion

We are not necessarily restricted to rely on only one localization technique. Two or more of them can be combined in order to make use of their specific advantages and to compensate for their disadvantages. To make two or more localization techniques cooperate, their measurements have to be combined in a certain manner. This process is called *sensor fusion*, see Figure 1.1 for an example.

For example, IMU is a popular component in sensor fusion due to its high accuracy in shorter periods. By fusing the IMU with the GPS, a localization system is obtained, which both has a high accuracy and provides absolute position information. This has been studied, for example in (Caron et al., 2006). The IMU can also be fused with vision, which not only increases the localization performance, but also enables for calibration of the system (Hol et al., 2010).

1.2 Alternative Localization Techniques

Two alternative localization techniques have been investigated in this thesis. By comparing them with each other, their properties are very different; Table 1.1 displays some figures. The two techniques will be presented in more detail below.

Table 1.1: *Properties of two alternative localization techniques investigated in this thesis.*

	Magnetic localization	Light levels
Coverage	Vicinity of the sensor	The whole earth
Accuracy	> 5 mm	150 km
Update frequency	100 Hz (sensor dependent)	Twice a day

1.2.1 Magnetic Localization

Magnetic sensors a.k.a. *magnetometers* are instruments measuring strength and mostly also the direction of magnetic fields. They have various applications ranging from finding land mines and shipwrecks to predicting weather (via solar cycles) and reading out magnetic memories. In navigation, magnetic sensors are most commonly used as a compass measuring the bearing of an object. However, in this thesis we will use the property that magnetic objects induce a magnetic field. Such an approach is used in *magnetic anomaly detectors* for detecting ferromagnetic objects, see Lenz and Edelstein (2006) for an overview of the problem and other applications.

In this thesis, we are not only interested in detecting magnetic objects, but also in determining their position, direction of motion, magnetic signature and geometrical shape. This will be accomplished by defining relevant mathematical models relating these quantities to the measured magnetic field. As an example, in Figure 1.2 an estimated trajectory of a magnet is presented using a network of four magnetometers. In contrast to GPS, laser range sensor and computer vision, this localization technology is not dependent of unobstructed line of sight between the sensors and the object. In fact, magnetic fields propagate in all direction before reaching the sensor. Therefore, it is nearly impossible to eliminate the magnetic signature of a magnetic object. This makes the sensors insensitive to jamming, which is important in military applications. In addition, the magnetic sensing is also almost independent of weather conditions.

Recently, magnetometers have become smaller and cheaper, which makes an extensive usage of magnetometers more interesting, for example, in localization of magnetic objects. However, the sensor range is for many application limiting. With commercial-use magnetometers a car can be sensed from a distance of approximately 10 m and a 1 cm long neodymium magnet from a distance of approximately 1 m. Further, magnetic sensors are superpositional, meaning that they measure the sum of the magnetic signatures from all present magnetic objects. In contrast to radar and vision, more objects do not create more measurements,

which makes a multi target tracking framework more challenging than for non-superpositional sensors.

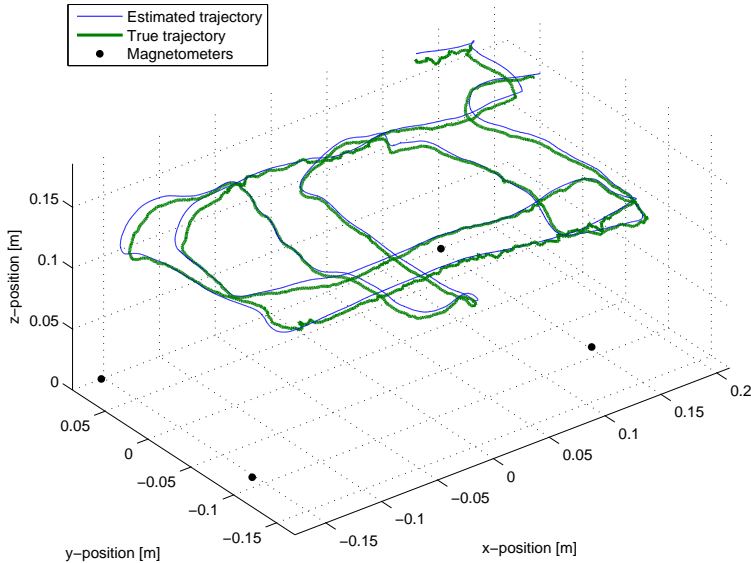


Figure 1.2: Localization performance of a magnet in a sensor network with four magnetometers deployed in the corners of a 20 cm \times 30 cm rectangle. The root mean square error is approximately 5 mm. The true trajectory has been captured using an optical reference system (Vicon)¹.

1.2.2 Light Levels

The position of celestial bodies (the sun, the moon, a planet or a star) has for hundreds of years been used by sailors in order to navigate. The angle between the celestial body and the horizon (altitude) reveals the longitude and latitude of the observer. Partial information about the altitude of the sun can be captured using a *light sensor* measuring the light intensity, see Figure 1.4. The event of sunrise and sunset can be detected. The events occur when the sun geometrically is a bit below the horizon depending on which light intensity threshold is chosen as definition for these events. Localization using light levels is for example discussed by Hill (1994); Stutchbury et al. (2009); Ekstrom (2004).

The big advantage with light intensity sensors is their low weight and low energy consumption in comparison to the GPS. It allows to construct devices under 1.5 g (including sensor, memory, battery and clock) lasting for many years, see

¹High accuracy reference measurements are provided through the use of the Vicon real-time tracking system courtesy of the UAS Technologies Lab, Artificial Intelligence and Integrated Computer Systems Division (AIICS) at the Department of Computer and Information Science (IDA), Linköping University, Sweden. <http://www.ida.liu.se/divisions/aiics/aiicssite/index.en.shtml>



Figure 1.3: A light logger consisting of a battery, memory clock and a light sensor with a weight of less than one gram, suited for bird localization ².

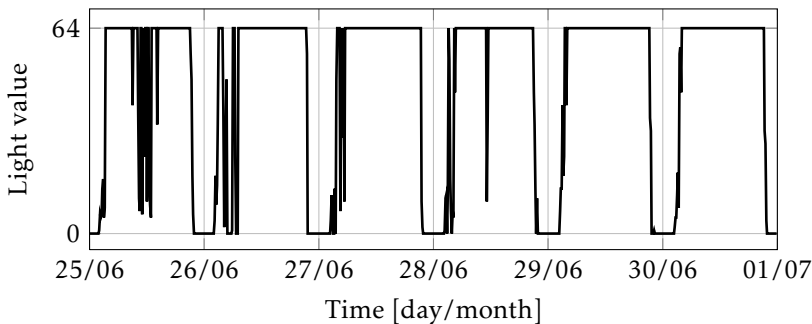


Figure 1.4: Light intensity sampled from a sensor mounted on a Common Murre (sv. Sillgrissla) from Karlsöarna in the Baltic see during the summer of 2010. The light sensor saturates during the day time and the night time. The measurements are also corrupted due to shading. The sampling time is 10 minutes.

Figure 1.3. The sensor is also more cost efficient and smaller than the GPS. Like GPS, the technology can be used over the whole earth, except close to the North Pole and South Pole during the winter solstice and summer solstice, since the sun will then never rise. This makes it to an attractive solution in applications where weight, cost and global coverage are important, for example, to localize small migrating animals.

On the other hand, the accuracy of approximately 150 km is much lower than for other technologies and depends on weather conditions and proximity to equinox and equator. The technology is also challenged by shading of foliage and other vegetation, which might cause false detection of the sunrise and sunset events.

²Source: Forskning & Framsteg 5/6 - 2012.

1.3 Applications and Collaborations

With the alternative localization techniques introduced above as basis, four main application areas have been investigated. Three of them - traffic surveillance, indoor localization and bird localization - are represented in this thesis, whereas one of them - interaction in public environments - is represented in the patent Gustafsson and Wahlström (2012). All four applications are introduced below.

1.3.1 Traffic Surveillance

Localization and tracking of vehicles are primary concerns in automated traffic surveillance systems. The information can be used for statistical purposes by road administrations, urban planners or traffic management centers to improve the road infrastructure. The information can also be used in safety systems, for example to detect wrong-way drivers on highways.

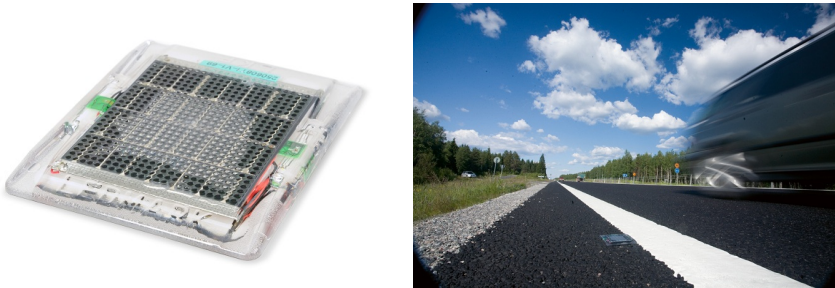


Figure 1.5: Sensor unit including 2-axis magnetometer and accelerometer powered with solar energy. The unit is glued on the road surface to sustain harsh weather conditions. Measurements from this unit have been used in Paper B. The photos have been provided by GEVEKO ITS. (www.gevekoits.dk)

Vehicles have a large content of ferromagnetic material and will therefore induce a magnetic field, which can be measured by magnetometers. By deploying one or more of these sensors in the vicinity of the traffic lane, the vehicle can be localized. For this application, the magnetometers have the advantage of being less sensitive to weather conditions in comparison to other technologies in automated surveillance systems, such as cameras. Their energy efficiency makes it possible also to integrate them in a wireless sensor node powered by solar energy. These nodes can be easily deployed at points of interest making the technology very flexible.

In Paper A different models for estimation of position, velocity and extension of vehicles using magnetometers will be analyzed. In Figure 1.6, the tracking performance is presented using one of these models.

Parts of the work in this thesis have also been accomplished in collaboration with Luleå University of Technology working with a sensor unit, see Figure 1.5, suited

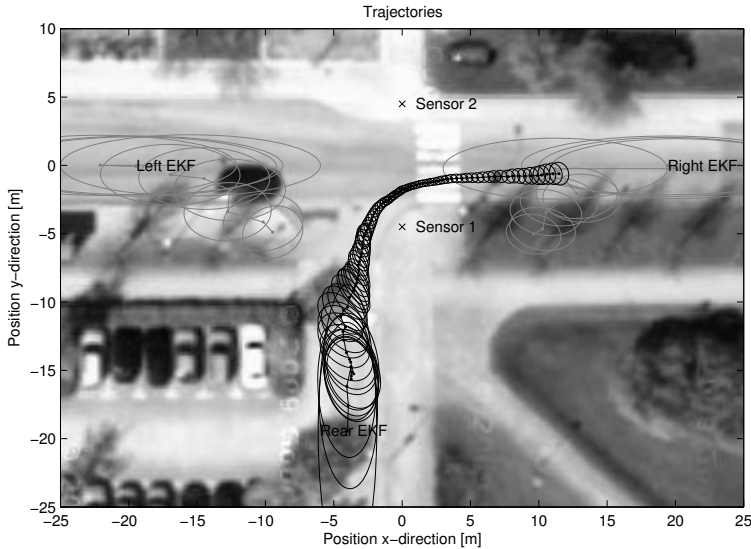


Figure 1.6: Results from a tracking experiment with two magnetometers and three differently initialized filters. The vehicle is coming from the bottom of the figure and makes a right turn. The ellipses represent a confidence interval of 90%. One can also observe that the uncertainty decreases in time as the vehicle gets closer to the sensor. The results have been reported by Wahlström et al. (2011).

for standing the harsh weather conditions present in northern Sweden. In this cooperation a robust classification of driving direction has been implemented and analyzed. This work is presented in Paper B. Except for the magnetometer, this sensor unit also contains an accelerometer enabling detection and estimation using road surface vibration, which has been investigated by Hostettler et al. (2012).

1.3.2 Interaction in Public Environments

Museums and science centers have a high need for technology enabling interactive exhibits that encourage visitors to experiment and explore. In exhibits where spatial information is important a localization system is required. Such systems have high requirements on robustness and have to be intuitive for the visitors to control and interact.

A network of magnetometers can be used to localize a permanent magnet attached to a tool operated by a visitor. Both its position and orientation can be computed without using any extra equipment commonly used, except for the magnet. In comparison to touch screens, which are common to enable interaction in these applications, this increases the level of interaction. Further, in contrast to vision based localization, the user does not have to operate relative to any special camera position.

The magnetic localization technique (Gustafsson and Wahlström, 2012) was used in an exhibition case mimicking water color painting, see Figure 1.7. The software for this exhibition case is a result of a master's thesis project by Correia and Jonsson (2012) that was supervised by the author of this thesis. The resulting system can today be seen in the science center *Visualiseringscenter C* in Norrköping.



Figure 1.7: Virtual watercolor painting application where the painting is displayed on a screen. The user interacts using a regular painting brush equipped with a permanent magnet. A sensor network of four magnetometers is mounted under the screen sensing the position and orientation of the brush. The user can paint and splash color on the virtual canvas and select new colors from the palette and wet the brush in the (virtual) water glass.

1.3.3 Indoor Localization and Mapping

Localization in indoor environments has in the past decade received an increasing attention. The applications are plenty, such as operating emergency personnel, navigation in shopping malls and positioning of autonomous vacuum cleaners. As explained earlier, the GPS system does not work in indoor environments. Therefore, many alternative localization techniques have been discussed and analyzed. Deak et al. (2012) give a survey of different indoor localization systems.

In recent years, the use of the magnetic disturbances present in indoor environments have been considered as a source for localization, see e.g. Vissière et al. (2007); Vallivaara et al. (2011); Zhang and Martin (2011); Le Grand and Thrun (2012). These disturbances are induced by metallic structures present in most buildings and carry enough information to be used for localization. The disturbances can be measured with a magnetometer and the localization might be aided using other sensors such as accelerometers and gyroscopes. In contrast to the two previous applications, this is an active localization system where the magnetic sources are stationary and the sensor is moving.

The modeling of such magnetic environments is challenging. Unlike the two previous application areas, the magnetic content is not limited to be in a small region (i.e. within a vehicle or within a permanent magnet). In Paper C the modeling of such complex magnetic environments will be addressed.

1.3.4 Bird Localization

Localization of migrating birds is important for evaluating theories about their migration strategies, the genetics and the evolution behind these strategies. For smaller birds, the weight of the localization equipment attached to the bird is crucial. As a rule of thumb, the sensor can weigh at most 5% of a bird's weight. Therefore, the use of light levels (as explained in Section 1.2.2) is an attractive localization technique, providing absolute position of small birds that other techniques cannot accomplish with these weight requirements.



Figure 1.8: Common swifts³.

With this technology, the migration pattern of the *common swift*, see Figure 1.8, has just recently been revealed by researcher from Lund University using data from light loggers mounted on different swifts, see (Åkesson et al., 2012). The common swift is a medium sized bird with a weight of 40 g in average, limiting the maximum allowed sensor equipment to 2 g.

In Paper D, the estimation of migration path will be formulated as a nonlinear filtering problem where the position is updated at each sunrise and sunset. The study is performed in collaboration with the aforementioned biologists from Lund University, who also have provided the real data presented in the work.

1.4 Thesis Outline

The thesis is divided into two parts, with edited versions of published and submitted papers in the second part. The first part introduces the theory needed for the models presented in this thesis. This is divided into two chapters representing the two localization techniques that are analyzed. Chapter 2 introduces the relevant electromagnetic theory describing the relation between magnetic objects and their induced magnetic field, and Chapter 3 introduces the astronomy that is needed in doing localization based on light levels. The first part ends with Chapter 4 summarizing the conclusions and further work.

The second part consists of edited versions of four papers: Wahlström and Gustafsson (2012) in Paper A, Wahlström et al. (2012c) in Paper B, Wahlström et al. (2013) in Paper C and Wahlström et al. (2012a) in Paper D, which all have been presented and mentioned above. Paper A, B and C are all under revision whereas Paper D is published. Note that earlier versions of Paper A is published in Wahlström et al. (2010) and partly in Wahlström et al. (2011). An early version of Paper B is published in Wahlström et al. (2012b).

Below is a summary of each paper:

³Source: http://en.wikipedia.org/wiki/Common_swift

Paper A: Magnetometer Modeling and Validation for Tracking Metallic Targets

N. Wahlström and F. Gustafsson. Magnetometer modeling and validation for tracking metallic targets. *IEEE Transactions on Signal Processing*, 2012. Under revision.

Summary: In this paper, a sensor model for three-axis magnetometers is presented, suitable for localization and tracking as required in intelligent transportation systems and security applications. The model depends on a physical magnetic dipole model of the target and its relative position to the sensor. Both point target and extended target models are provided as well as a target orientation dependent model. The suitability of magnetometers for tracking is analyzed in terms of local observability and the Cramér Rao lower bound as a function of the sensor positions in a two sensor scenario. The models are validated with real field test data taken from various road vehicles which indicate excellent localization as well as identification of the magnetic target model suitable for target classification. These sensor models can be combined with a standard motion model and a standard nonlinear filter to track metallic objects in a magnetometer network.

Background and contribution: This contribution is to a large extent based on the author's master's thesis (Wahlström, 2010). The experimental results are the same as in that thesis, but the theoretical part has since then been extended. The author of the thesis wrote the major part of the paper.

Paper B: Classification of Driving Direction in Traffic Surveillance using Magnetometers

N. Wahlström, R. Hostettler, F. Gustafsson, and W. Birk. Classification of driving direction in traffic surveillance using magnetometers. *IEEE Transactions on Intelligent Transportation Systems*, 2012c. Submitted.

Summary: We present an approach for computing the driving direction of a vehicle by processing measurements from one 2-axis magnetometer. The proposed method relies on a non-linear transformation of the measurement data comprising only two inner products. Deterministic analysis of the signal model reveals how the driving direction affects the measurement signal and the proposed classifier is analyzed in terms of its statistical properties. The method is compared with a model based likelihood test using both simulated and experimental data. The experimental verification indicates that good performance is achieved under the presence of saturation, measurement noise, and near field effects.

Background and contribution: The cooperation with Roland Hostettler was initiated at Reglermöte (Swedish control conference) 2010 and in the fall data was collected together. Later, the author of this thesis came up with the core idea presented in this paper. In all other aspects the work has been accomplished jointly including data collection, theoretical analysis, coding and writing. Prof. Fredrik Gustafsson and Dr. Wolfgang Birk have acted as supervisors.

Paper C: Modeling Magnetic Fields using Gaussian Processes

N. Wahlström, M. Kok, T.B. Schön, and F. Gustafsson. Modeling magnetic fields using Gaussian processes. In *Proceedings of the the 38th International Conference on Acoustics, Speech, and Signal Processing (ICASSP)*, Vancouver, Canada, May 2013. Submitted.

Summary: Starting from the electromagnetic theory, we derive a Bayesian non-parametric model allowing for joint estimation of the magnetic field and the magnetic sources in complex environments. The model is a Gaussian process which exploits the divergence- and curl-free properties of the magnetic field by combining well-known model components in a novel manner. The model is estimated using magnetometer measurements and spatial information implicitly provided by the sensor. The model and the associated estimator are validated on both simulated and real world experimental data producing Bayesian nonparametric maps of magnetized objects.

Background and contribution: The author of the thesis came up with the modeling idea presented in this paper after a PhD course in machine learning. The measurements have been collected together with Manon Kok and the author of this thesis has done the coding and has written the majority of the text.

Paper D: A Voyage to Africa by Mr Swift

N. Wahlström, F. Gustafsson, and S. Åkesson. A Voyage to Africa by Mr Swift. In *Proceedings of the 15th International Conference on Information Fusion (FUSION)*, pages 808–815, Singapore, July 2012a.

Summary: A male common swift *Apus apus* was equipped with a light logger on August 5, 2010, and again captured in his nest 298 days later. The data stored in the light logger enables analysis of the fascinating travel he made in this time period. The state of the art algorithm for geolocation based on light loggers consists in computing first sunrise and sunset from the logged data, which are then converted to midday (gives longitude) and day length (gives latitude). This approach has singularities at the spring and fall equinoxes, and gives a bias for fast day transitions in the east-west direction. We derive a flexible particle filter solution, where sunset and sunrise are processed separately in two different measurement updates, and where the motion model has two modes, one for migration and one for stationary long time visits, which are designed to fit the flying pattern of the swift. This approach circumvents the aforementioned problems with singularity and bias, and provides realistic confidence bounds on the geolocation as well as an estimate of the migration mode.

Background and contribution: Prof. Fredrik Gustafsson came up with the initial idea to treat this application as a filtering problem and Prof. Susanne Åkesson has provided the data and expertise in migrating birds. The author of this thesis has developed the framework and has written the majority of the text.

1.5 Other Publications

Publication of related interest, but not included in this thesis:

E. Almqvist, D. Eriksson, A. Lundberg, E. Nilsson, N. Wahlström, E. Frisk, and M. Krysander. Solving the ADAPT benchmark problem - A student project study. In *21st International Workshop on Principles of Diagnosis (DX-10)*, Portland, Oregon, USA, October 2010.

N. Wahlström, J. Callmer, and F. Gustafsson. Magnetometers for tracking metallic targets. In *Proceedings of 13th International Conference on Information Fusion (FUSION)*, Edinburgh, Scotland, July 2010.

N. Wahlström, J. Callmer, and F. Gustafsson. Single target tracking using vector magnetometers. In *Proceedings of the International Conference on Acoustics, Speech and Signal Processing (ICASSP)*, pages 4332–4335, Prague, Czech Republic, May 2011.

N. Wahlström, R. Hostettler, F. Gustafsson, and W. Birk. Rapid classification of vehicle heading direction with two-axis magnetometer. In *Proceedings of the International Conference on Acoustics, Speech and Signal Processing (ICASSP)*, pages 3385–3388, Kyoto, Japan, March 2012b.

F. Gustafsson and N. Wahlström. Method and device for pose tracking using vector magnetometers, 2012. Patent. Under revision.

M. Kok, N. Wahlström, T.B. Schön, and F. Gustafsson. MEMS-based inertial navigation based on a magnetic field map. In *Proceedings of the 38th International Conference on Acoustics, Speech, and Signal Processing (ICASSP)*, Vancouver, Canada, May 2013. Submitted.

1.6 Contributions

The main contributions of this thesis are focused on models used for various localizations applications. These are:

- **Parametric magnetic model:** Models describing moving magnetic objects. In Paper A, a variety of different models are presented including a point target model, an extended target model and a target orientation dependent model. Paper B focuses on a model for estimating the driving direction of the vehicle.
- **Nonparametric magnetic model:** Models describing complex magnetic environments suitable for indoor localization are described in Paper C.
- **Light level model:** Models describing light level data suitable for localizing migrating birds. This is the main contribution of Paper D.

2

Electromagnetic Theory

This chapter introduces the electromagnetic theory. Special interest will be given to the magnetic field and its properties when currents are steady. The material presented this chapter is to a great extent based on the theory as presented by Jackson (1998) and Cheng (1989).

Even though electromagnetic phenomena were known to the ancient Greeks, its development as a quantitative subject started first in the end of the 18th century with Cavendish' and Columbus' experiments and research. Fifty years later Faraday was studying time-varying electromagnetic phenomena. By 1865 James Clerk Maxwell had published his famous paper (Maxwell, 1865) on a dynamical theory of the electromagnetic field. In that paper, the original set of four equations first appeared. These equations will be our theoretical starting point.

2.1 Maxwell's Equations

All electromagnetic phenomena are governed by *Maxwell's equations*,

$$\nabla \cdot \mathbf{E} = \frac{\rho}{\epsilon_0}, \quad (2.1a)$$

$$\nabla \times \mathbf{B} - \mu_0 \epsilon_0 \frac{\partial \mathbf{E}}{\partial t} = \mu_0 \mathbf{J}, \quad (2.1b)$$

$$\nabla \times \mathbf{E} + \frac{\partial \mathbf{B}}{\partial t} = \mathbf{0}, \quad (2.1c)$$

$$\nabla \cdot \mathbf{B} = 0, \quad (2.1d)$$

where \mathbf{E} is the *electric field*, ρ is the *charge density*, \mathbf{B} is the *magnetic field* and \mathbf{J} is the *current density*. The equations (2.1) are given in SI units. Apart from the

fields \mathbf{E} and \mathbf{B} and their sources ρ and \mathbf{J} , the equations also include the constants ϵ_0 and μ_0 , which are the *permittivity* and *permeability* of free space respectively. The permeability of free space μ_0 has a defined value

$$\mu_0 = 4\pi \times 10^{-7} \text{ F m}^{-1} = 1.257 \times 10^{-6} \text{ F m}^{-1}, \quad (2.2)$$

and the permittivity of free space is defined by

$$\epsilon_0 = 1/(\mu_0 c_0^2) = 8.854 \times 10^{-12} \text{ H m}^{-1}, \quad (2.3)$$

where c_0 is the *speed of light* in vacuum. Table 2.1 summarizes the meaning of each symbol and the SI unit of measure.

Table 2.1: Definitions and units.

Symbol	Meaning	SI unit
\mathbf{E}	Electric field	Volt per meter [V m^{-1}]
\mathbf{B}	Magnetic field	Tesla [T]
ρ	Charge density	Coulombs per cubic meter [C m^{-3}]
\mathbf{J}	Current density	Amperes per square meter [A m^{-2}]
ϵ_0	Permittivity of free space	Farads per meter [F m^{-1}]
μ_0	Permeability of free space	Henries per meter [H m^{-1}]
c_0	Speed of light in vacuum	Meter per second [m s^{-1}]

2.2 Quasi-Static Approximation

In this thesis, the magnetic field \mathbf{B} is of special interest, since that is the quantity that will be measured. In general, it is coupled with the electric field \mathbf{E} through their time derivatives (2.1b) and (2.1c). However, in the stationary case the terms $\partial\mathbf{E}/\partial t$ and $\partial\mathbf{B}/\partial t$ can be neglected, and Maxwell's equations will be decoupled. The magnetic field will therefore obey the *magnetostatic equations*

$$\nabla \times \mathbf{B} = \mu_0 \mathbf{J}, \quad (2.4a)$$

$$\nabla \cdot \mathbf{B} = 0. \quad (2.4b)$$

From these equations it is clear that the current density \mathbf{J} can be regarded as the source causing the magnetic field \mathbf{B} . If the current density is time-dependent, the static assumption does not hold and the full solution of Maxwell's equations has to be considered. However, if these changes are sufficiently small, a *quasi-static approximation* can be made, in which the magnetostatic equations (2.4) still hold. In this approximation, (2.4a) states that any variation in the current density \mathbf{J} is instantaneously communicated to the magnetic field \mathbf{B} , implying that the velocity of propagation is infinite. Hence, this approximation is only valid if the time lag produced by the finite velocity of propagation is very small in comparison with the time interval in which the currents undergo relevant changes. If the changes are periodical with a certain frequency the condition of quasi-stationarity can be

expressed as

$$\text{size of the physical system} \times \text{frequency} \ll c_0.$$

This can be illustrated with the following example borrowed from Di Bartolo (2004).

2.1 Example

For a transformer with the characteristic size of 30 cm and a frequency of 50 Hz we have

$$\text{size} \times \text{frequency} = 0.3 \text{ m} \times 50 \text{ s}^{-1} = 15 \text{ m s}^{-1} \ll c_0 = 300\,000\,000 \text{ m s}^{-1}$$

Thus, in this transformer, the quasi-static approximation is valid.

2.3 Magnetic Dipole Moment

Having a complete knowledge of the current density \mathbf{J} enables us to find the solution for the magnetic field \mathbf{B} using the magnetostatic equations (2.4). However, its solution is not trivial and further approximations have to be applied. In many scenarios of interest the current density is zero except in one small region, see Figure 2.1. Instead of solving the full system (2.4), we can represent this region

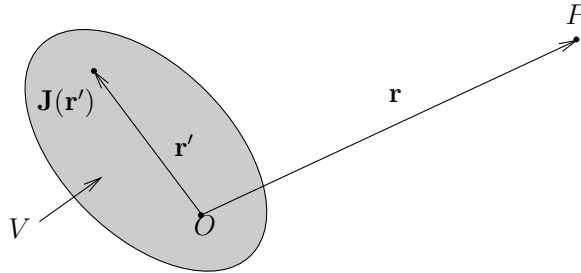


Figure 2.1: Localized current density $\mathbf{J}(\mathbf{r}')$ in the region V gives rise to a magnetic induction at the point P with coordinate \mathbf{r} . Outside the region V the current density is zero $\mathbf{J}(\mathbf{r}') = \mathbf{0}$.

V (further on referred to as the *object*) with its *magnetic dipole moment* \mathbf{m} at point O , which is related to the current density as

$$\mathbf{m} \triangleq \frac{1}{2} \int_V \mathbf{r}' \times \mathbf{J}(\mathbf{r}') d^3 r' \quad [\text{A m}^2], \quad (2.5)$$

where \mathbf{r}' is a integration variable, $d^3 r' = dx' dy' dz'$ is a three dimensional volume element at \mathbf{r}' and $\mathbf{J}(\mathbf{r}')$ is the current density at position \mathbf{r}' . The big advantage with this formulation is that we can derive an analytical expression relating the

magnetic dipole moment to the magnetic field, namely the magnetic dipole field

$$\mathbf{B}(\mathbf{r}) = \frac{\mu_0}{4\pi} \frac{3(\mathbf{r} \cdot \mathbf{m})\mathbf{r} - \|\mathbf{r}\|^2 \mathbf{m}}{\|\mathbf{r}\|^5} = \underbrace{\frac{\mu_0}{4\pi\|\mathbf{r}\|^5} (3\mathbf{r}\mathbf{r}^\top - \|\mathbf{r}\|^2 \mathbf{I}_3)}_{\triangleq \mathbf{C}(\mathbf{r})} \mathbf{m} = \mathbf{C}(\mathbf{r})\mathbf{m} \quad (2.6)$$

where \mathbf{r} is a vector from the object O to the point P where the magnetic field is being observed (further on referred to as the *observer*). Note, that this expression is only valid for the magnetic field outside the region V of the object. The derivation of this dipole field can be found in Appendix A and requires a Taylor expansion which is only valid if the distance to the observer is large in comparison to the size of the object, i.e. if $\|\mathbf{r}\| \gg \|\mathbf{r}'\|$ in (2.1). This dipole model will be the theoretical starting point for the models presented in Paper A and Paper B.

Further, if there are multiple objects, each of them will induce its own magnetic dipole field.

$$\mathbf{B}_i(\mathbf{r}) = \mathbf{C}(\mathbf{r} - \mathbf{r}_i)\mathbf{m}_i. \quad (2.7)$$

where \mathbf{r}_i is the position of the object and \mathbf{m}_i its dipole moment. Due to the linearity of the magnetostatic equations (2.4) all magnetic dipole fields will superimpose

$$\mathbf{B}(\mathbf{r}) = \sum_i \mathbf{B}_i(\mathbf{r}) = \sum_i \mathbf{C}(\mathbf{r} - \mathbf{r}_i)\mathbf{m}_i. \quad (2.8)$$

Multiple dipoles can also be used to represent larger objects by dividing them into smaller regions and represent each region with a magnetic dipole. This model has been proposed in Paper A to represent larger vehicles. The idea can also be taken one step further. By dividing the object into even smaller regions, we will in the limit define the *magnetization*. This concept will be explained in the next section.

2.4 Magnetization

All materials consist of atoms with orbiting electrons. The electrons give rise to circular currents where each of them can be represented with a magnetic dipole moment \mathbf{m}_i . All these dipole moments will describe the magnetization of the material. However, due to the very large number of atoms in a material, this description is not convenient. Therefore, we use its average over a larger volume and describe magnetization as the quantity of magnetic moment per unit volume. If there are n atoms per unit volume, we define the *magnetization* as

$$\mathbf{M}(\mathbf{r}) \triangleq \lim_{\Delta V \rightarrow 0} \frac{\sum_{i=1}^{n\Delta V} \mathbf{m}_i}{\Delta V} \quad [\text{A m}^{-1}], \quad (2.9)$$

where $\sum_{i=1}^{n\Delta V} \mathbf{m}_i$ denotes the sum of all magnetic dipole moments within the volume element ΔV centered at \mathbf{r} . The magnetization can be seen as a density of magnetic dipole moments. This description is convenient since we can describe mag-

netized regions which otherwise would require infinitely many magnetic dipole moments.

By generalizing (2.8) we can also find a relation between the magnetization and the magnetic field.

$$\mathbf{B}(\mathbf{r}) = \int C(\mathbf{r} - \mathbf{r}')\mathbf{M}(\mathbf{r}')d^3r' \quad (2.10)$$

Using this relation, the magnetic dipole can be seen as a Dirac-distribution, illustrated in the example below.

2.2 Example

Consider a magnetization localized at position \mathbf{r}_i and zero elsewhere $\mathbf{M} = \mathbf{m}\delta(\mathbf{r} - \mathbf{r}_i)$. By using this field in (2.10) we get

$$\mathbf{B}(\mathbf{r}) = \int C(\mathbf{r} - \mathbf{r}')\mathbf{m}\delta(\mathbf{r}' - \mathbf{r}_i)d^3r' = C(\mathbf{r} - \mathbf{r}_i)\mathbf{m}, \quad (2.11)$$

which is the magnetic dipole field of a magnetic dipole at \mathbf{r}_i with magnetic dipole moment \mathbf{m} .

However, the description (2.10) is complicated and highly non-linear. By introducing the *magnetizing field* we can instead describe this relation with a set of linear differential equations similar to (2.4). This is explained below.

2.5 Magnetizing Field

The current density \mathbf{J} can be divided into *magnetization current* \mathbf{J}_m and *free current* \mathbf{J}_f as

$$\mathbf{J} = \mathbf{J}_f + \mathbf{J}_m. \quad (2.12)$$

The magnetization current is bounded to the material and can be seen as the current density due the electrons orbiting around the electrons in the material. It is defined as being the curl of the magnetization

$$\mathbf{J}_m \triangleq \nabla \times \mathbf{M} \quad [\text{A m}^{-2}]. \quad (2.13)$$

The free current density \mathbf{J}_f is not bounded to any material and its charges can move freely, for example currents in electric cables etc.

By introducing the division 2.12 in the magnetostatic equations (2.4a), this results in

$$\frac{1}{\mu_0}\nabla \times \mathbf{B} = \mathbf{J}_f + \mathbf{J}_m = \mathbf{J}_f + \nabla \times \mathbf{M}, \quad (2.14)$$

or

$$\nabla \times \left(\frac{\mathbf{B}}{\mu_0} - \mathbf{M} \right) = \mathbf{J}_f. \quad (2.15)$$

Now, a new field \mathbf{H} can be defined called the *magnetizing field*

$$\mathbf{H} \triangleq \frac{\mathbf{B}}{\mu_0} - \mathbf{M} \quad [\text{A m}^{-1}]. \quad (2.16)$$

With this quantity, an alternative version of the magnetostatic equation only including the free current can be given as

$$\nabla \times \mathbf{H} = \mathbf{J}_f, \quad (2.17a)$$

$$\nabla \cdot \mathbf{B} = 0. \quad (2.17b)$$

By this we have reformulated the magnetostatic equations (2.4) into (2.17) which only depend on the free current \mathbf{J}_f and not the magnetization current \mathbf{J}_m . The effect of the magnetization current is described with the magnetization \mathbf{M} , which couples the two magnetic fields \mathbf{B} and \mathbf{H} via (2.16). The equations (2.16) and (2.17) have been used in Paper C for modeling complex magnetic structures in indoor environments using Bayesian nonparametric methods. In that contribution, we assume $\mathbf{J}_f = \mathbf{0}$ which enables an exploitation of the curl- and divergence-free properties of the \mathbf{H} - and \mathbf{B} -fields, respectively.

2.6 Magnetic Materials

As we explained earlier, all materials consist of atoms where each of them can be described with a magnetic dipole. In most materials, these dipoles are not structured in any certain manner and the total magnetization will therefore be zero. However, in some materials these dipoles will be affected by the presence of an external field, which will give raise to a non-zero magnetization. In these materials we distinguish between properties referred to as soft and hard iron.

2.6.1 Soft Iron

In soft iron the magnetization will be aligned with an applied external field, see Figure 2.2. If the material is linear and isotropic this magnetization is directly proportional to the magnetizing field

$$\mathbf{M} = \chi_m \mathbf{H}, \quad (2.18)$$

where χ_m is the *magnetic susceptibility*, which is a dimensionless constant characteristic for the magnetic material. Using the relation (2.16), this will also result in a relation between the magnetic field and the magnetization

$$\mathbf{M} = \frac{1}{\mu_0} \frac{\chi_m}{1 - \chi_m} \mathbf{B}. \quad (2.19)$$

Thus, the magnetization will always be aligned with the external field regardless of the orientation of the object. Furthermore, if the applied magnetic field is removed, the magnetization will disappear.

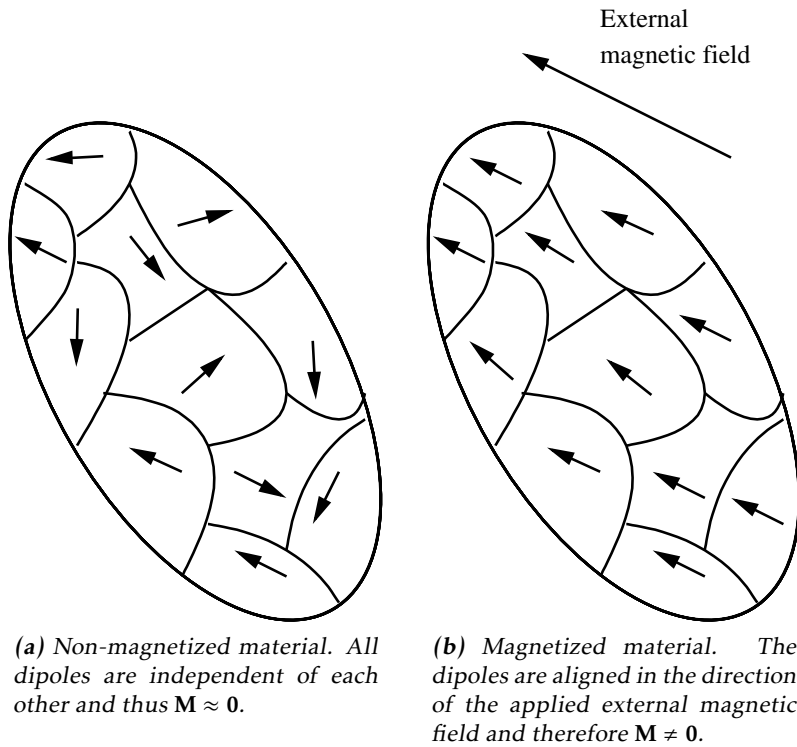


Figure 2.2: A material with $\chi_m > 0$ will be magnetized when an external field is applied.

2.6.2 Hard Iron

For weak applied magnetic fields, the \mathbf{H} - and \mathbf{M} -field will reduce to zero when the applied field is removed. However, for strong applied magnetic field the process will for some materials not be reversible forming permanent magnets. Materials having this property are called ferromagnetic. Magnetized ferromagnetic substance will also contribute to the total magnetization. Such permanent magnetization is referred to as hard iron. The hard iron magnetization will (in contrast to soft iron) be aligned with the reference frame of the object and will thus rotate as when the object rotates.

2.7 Summary and Connections

In this chapter a short overview of the electromagnetic theory relevant for this thesis has been presented. Concepts such as magnetic dipole moment, magnetization, soft iron and hard iron have been introduced and will later be used in Paper A, B and C in the second part of this thesis.

The magnetic dipole model (2.6) has been introduced and proven to have properties suitable for modeling magnetic objects with small geometrical extent. However, in the real world scenarios presented in each of these three papers, the extent of the magnetic objects is not negligible and has to be taken into consideration. This issue will be treated differently in each of the three papers.

- In Paper A the dipole model will be extended by using a grid of dipoles similar to (2.8). Each dipole can be considered to correspond to a region, where each region is smaller than the whole object, compare with Figure 2.2. The model has a parameter vector which includes the magnetic dipole moments as well as the position of the objects and a parameter related to its geometrical extent.
- The dipole model will also be used in Paper B. However, the model will not be used explicitly, only one property of it. This property is invariant to the geometrical extent of the target.
- In Paper C the magnetization \mathbf{M} (2.9) will be used to model the magnetic objects. The magnetization can be seen as a continuum with infinitely many magnetic dipole moments. To handle such infinitely dimensional objects a Bayesian nonparametric modeling technique will be investigated.

Furthermore, the separation of the soft iron and hard iron contribution to the magnetization as presented in Section 2.6 will be exploited in Paper A.

3

Astronomy

The phenomena in the sky have for a long time been a source for peoples' interest and fascination. During the development of seafaring in the 17th and 18th centuries, the astronomy started be used a for navigation, see Cotter (1968). To be able to use astronomy for navigational purposes, we need to know the laws governing the motion of celestial objects in the sky. These equations are presented in this chapter. Kepler's laws will be the starting point.

3.1 Kepler's Laws

In 1609 Johannes Kepler developed two laws¹ describing planetary motions:

1. The orbit of a planet is an ellipse, one focus of which is in the sun.
2. The radius vector of a planet sweeps equal areas in equal amounts of time.

These two laws are illustrated in Figure 3.1 and from them it is possible to derive the equation of motion for the planet in its orbit around the sun. Due to the elliptic form of the orbit the distance between planet and the sun will change over time. The point where the planet is as closest to the sun is called the *perihelion*. The position of the planet can now be described with an angle, the *true anomaly* f , measured from the perihelion. As a consequence of Kepler's second law, the true anomaly will not increase at a constant rate. For example, the planet moves faster closer to the perihelion than at other places.

By following any standard textbook on astronomy, for example Karttunen (2003), an analytical expression of the true anomaly based on Kepler's laws can be de-

¹There is also a third law of Kepler describing orbital periods, which Kepler published many years later in 1628. However, this law is not needed for describing the orbital motion of planets.

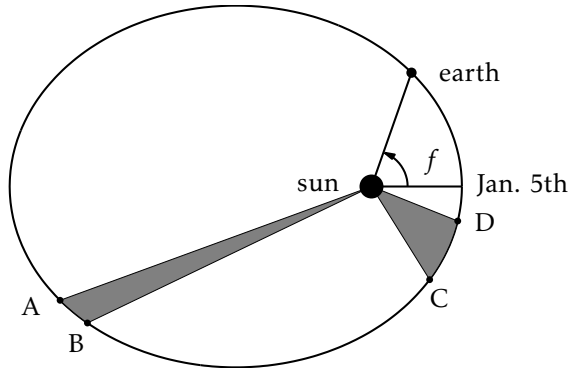


Figure 3.1: An illustration of Kepler's first and second law. The areas of the sectors are equal. According to Kepler's second law it takes equal time to travel the distances AB and CD .

rived,

$$\cos(f) = \frac{\cos(E) - e}{1 - e \cos(E)}. \quad (3.1a)$$

The *eccentric anomaly* E and the *mean anomaly* M are given by Kepler's equation

$$E - e \sin(E) = M, \quad (3.1b)$$

$$M = \frac{2\pi}{P}(t - \tau), \quad (3.1c)$$

where P is the orbital period, $t - \tau$ is the time elapsed since perihelion and e is the so-called *orbital eccentricity*. The orbital eccentricity describes the amount by which the orbit deviates from the circle, where $e = 0$ is a perfect circle and for $0 < e < 1$ the orbit is elliptic. The earth's orbit is only slightly elliptic with $e = 0.0167$.

Note that for the special case of a circular orbit $e = 0$, this gives $f = E = M$ and the mean anomaly f will increase at a constant rate as expected. For the earth the perihelion occurs 14 days after the winter solstice at about the 5th of January.

3.2 Spherical Astronomy

In order to describe the apparent motion of celestial objects, different coordinate systems have to be introduced. The transformations between these coordinate systems are used to derive analytical expressions of the position for celestial objects on the sky. Before introducing these coordinate systems, some mathematical tools related to spherical trigonometry are needed.

3.2.1 Spherical Geometry

Spherical geometry is the geometry on the surface of a sphere. In Euclidean geometry the basic component is the straight line, being the shortest path between two points. In spherical geometry, the shortest path is an arc of a *great circle*².

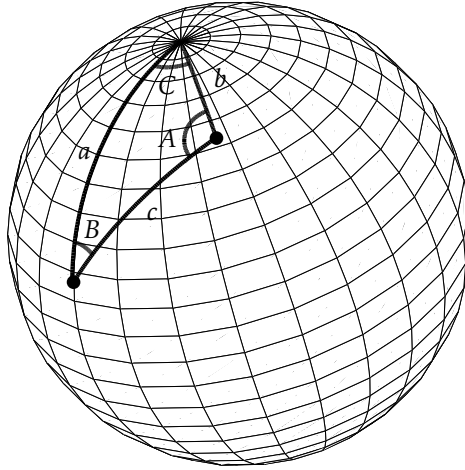


Figure 3.2: A spherical triangle.

A *spherical triangle* is a triangle lying on the sphere where its sides are arcs of great circles, see Figure 3.2. In contrast to euclidean triangles, the sum of the angles is always greater than 180° . Also, the trigonometric laws related to the triangle are slightly different. The *spherical law of cosines* reads

$$\cos(c) = \cos(a) \cos(b) + \sin(a) \sin(b) \cos(C). \quad (3.2)$$

In the limit when the sides a , b and c shrink to zero, the spherical triangle becomes an euclidean triangle. Using the following approximation valid for small angles v

$$\sin(v) \approx v, \quad \cos(v) \approx 1 - \frac{1}{2}v^2, \quad (3.3)$$

one gets the euclidean law of cosine

$$c^2 = a^2 + b^2 - 2ab \cos(C), \quad (3.4)$$

where also higher order terms have been ignored.

Also the *law of sines* has its counterpart in spherical geometry

$$\frac{\sin(a)}{\sin(A)} = \frac{\sin(b)}{\sin(B)} = \frac{\sin(c)}{\sin(C)}. \quad (3.5)$$

²A great circle is the intersection of a sphere and a plane, which passes through the center of the sphere. If the plane does not pass the center, the intersection is called a small circle.

Using the same approximation as before, we get the corresponding formula for Euclidian geometry

$$\frac{a}{\sin(A)} = \frac{b}{\sin(B)} = \frac{c}{\sin(C)}. \quad (3.6)$$

The proof of these formulas can be found in textbooks on geometry (Fenn, 1993) or astronomy (Karttunen, 2003).

Furthermore, following (Karttunen, 2003) we also have a third identity

$$\cos(A) \sin(c) = -\cos(C) \sin(a) \cos(b) + \cos(a) \sin(b) \quad (3.7)$$

which has a more trivial counterpart in Euclidean geometry

$$b = \cos(A)c + \cos(C)a \quad (3.8)$$

By using the two identities (3.5) and (3.7) we will also be able to end up in the following relation

$$\tan(A) = \frac{\sin(C)}{-\cos(C) \cos(b) + \frac{\sin(b)}{\tan(a)}}. \quad (3.9)$$

The two formulas (3.2) and (3.9) will be used to define the transformation between the coordinate systems introduced below.

3.2.2 Coordinate Systems

The position of a celestial object on the sky depends on both the position of the observer and on the time. To derive the equations describing these dependences, different coordinate systems have to be introduced. Here, all of them will be defined in spherical coordinates. Since we are only interested in points on the sphere, each coordinate system has two coordinates referred to as *latitude* and *longitude*, see Figure 3.3.

For each coordinate system we need a reference plane dividing the sphere into two equally big halves. The latitude is the angle from this plane to the point of interest and has the range $[-90^\circ, 90^\circ]$ and the intersections between the normal to the reference plane and the sphere are called the North Pole and the South Pole. To define the longitude we also need a reference meridian which is a half arc of a great circle connecting the North Pole and the South Pole. Further, the longitude is the angle from this meridian to the point of interest and has the range $[0^\circ, 360^\circ]$. The usual convention is to use a right-handed coordinate system, where the longitude is defined in clockwise direction from the reference meridian. For some angles it is more intuitive to use hours instead of degrees where 360 degrees equals 24 hours. Like other text books on astronomy, both units will be used. For example, when adding a quantity measured in hours with a quantity measured degrees, the relation $360^\circ = 24 \text{ h}$ applies.

In addition to the reference plane and reference meridian we also need a sphere. Two different spheres will be used for this task: the terrestrial sphere and the

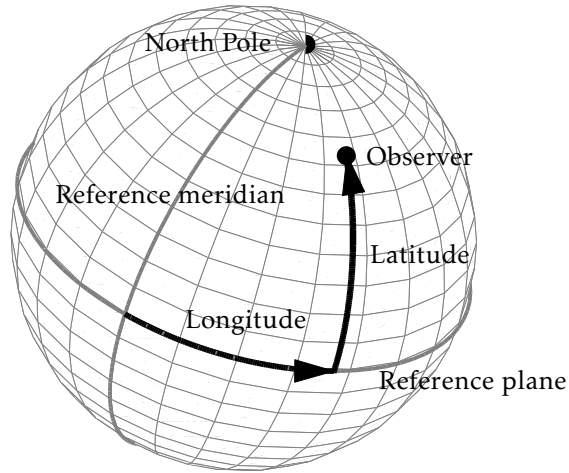


Figure 3.3: A point on the sphere can be defined with its latitude (relative to the reference plane) and its longitude (relative to the reference meridian).

celestial sphere. The terrestrial sphere represents the earth³. From the earth, the sky looks like another sphere. All celestial objects seem to be on the surface of this sphere with the earth in its center. Of course, all celestial objects are all at different distances, but this abstract construction will be helpful when defining the celestial coordinate systems. In Table 3.1 and Table 3.2 an overview of the different coordinate systems are given. More specific details are given in the sections below.

Table 3.1: Spherical coordinates of the different coordinate systems.

Coordinate system	Latitude	Longitude
Geographic	Geographic latitude γ	Geographic longitude χ
Horizontal	Altitude h	Azimuth A
Equatorial	Declination d	Right ascension α
Ecliptic	Ecliptic latitude β	Ecliptic longitude λ

Table 3.2: References for the different coordinate systems.

Coordinate system	Sphere	Reference meridian	Reference plane
Geographic	Terrestrial	Greenwich meridian	Equatorial plane
Horizontal	Celestial	South	Horizontal plane
Equatorial	Celestial	Vernal equinox	Equatorial plane
Ecliptic	Celestial	Vernal equinox	Ecliptic plane

³The earth is not exactly a sphere. Due to the rotation of the earth, its shape is slightly flattened on the poles. This results in a slightly different definition of longitude and latitude. See e.g. Karttunen (2003) for more discussion on this.

Geographic Coordinate Systems

The *geographic coordinate system* is used to define a position on the earth, where the equator defines the reference plane. The coordinates are *geographic latitude* and *geographic longitude*, usually referred to as just latitude and longitude. The longitude is the angular distance measured from the meridian passing through Greenwich Observatory in England. We will use positive values of the longitude for positions east of Greenwich, which is the standard convention in navigation. However, the sign convention varies. Astronomers usually define the longitude to have positive values in west-direction, see Meeus (1991) for a discussion on this.

Horizontal Coordinate System

The *horizontal coordinate system* uses the observer's local horizon as the reference plane, which is defined as the tangent plane of the earth passing through the observer. It measures the position of the sun using its altitude h and azimuth A , see Figure 3.4. The poles in this coordinate system are called *zenith* (above the observer) and *nadir* (below the observer).

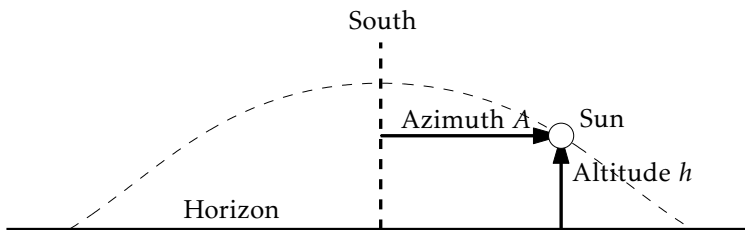


Figure 3.4: The horizontal coordinate system. The position of the sun is defined with its altitude h and azimuth A .

The altitude is the angular distance from the horizon to the celestial object and is measured in degrees. For navigational purposes this angle can be measured with a sextant, which is an instrument for determining the angle between two visible objects. In Paper D, information about the sun's altitude is instead provided with measurement from a light sensor, which has a high resolution during sunrise and sunset.

The azimuth is the angular distance to the celestial object from a fixed reference point. Here, we use the south direction as the reference meridian, but different conventions exist here as well. The azimuth of the sun will not affect the light intensity and this quantity will therefore not be used in the framework presented in Paper D.

Equatorial Coordinate System

The *equatorial coordinate system* defines the position of a celestial body on the celestial sphere with its *declination* d and *right ascension* α . It resembles the geographical coordinate system in the sense that they both have the equatorial plane

as reference plane. However, the reference meridian of the equatorial coordinate system is fixed on the celestial sphere rather than on the earth. Thus, it is unaffected by the rotation of the earth. This reference point is called *vernal equinox*⁴ and is denoted Υ .

To be able to find the transformation between the horizontal and the equatorial coordinate system, it is convenient to define a longitude to the celestial object using a reference point which is fixed on the earth. For this we use the *local hour angle*, which has the observer's local meridian as this reference point and is positive west of this meridian. Due to the earth's rotation, the hour angle to a celestial object grows with time. The hour angle of the vernal equinox is called the *sidereal time* Θ , which relate the local hour angle with right ascension as (see also Figure 3.5),

$$\Theta = H + \alpha. \quad (3.10)$$

The sidereal time depends on the longitude of the observer. To make it independent of the observer's location we use the *Greenwich sidereal time* Θ_G , which is the sidereal time at the Greenwich meridian. This gives the relation between the local hour angle and the longitude of the observer.

$$H = \Theta_G - \alpha + x. \quad (3.11)$$

All these quantities might either be given in hours or degrees, where 24 degrees equals 360 degrees.

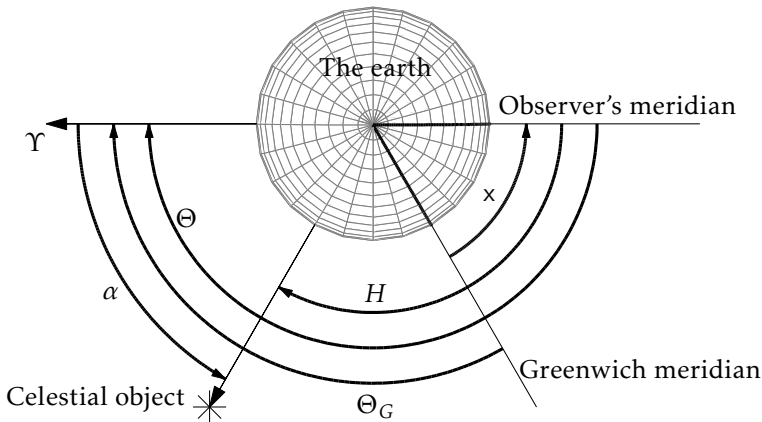


Figure 3.5: The figure displays the relation between the observer's longitude x , the local hour angle H , the sidereal time Θ , the Greenwich sidereal time Θ_G and the right ascension α .

Transformation between the horizontal and the equatorial coordinate system can now be derived using spherical trigonometry. We analyze a spherical triangle

⁴The point is in some books also-called *First point of Aries*, since it is used to be in the constellation of Aries.

combining the observer's zenith, the position of the celestial object and the North pole, see Figure 3.6. This triangle is usually called the *astronomical triangle*, see e.g. Barton (1943).

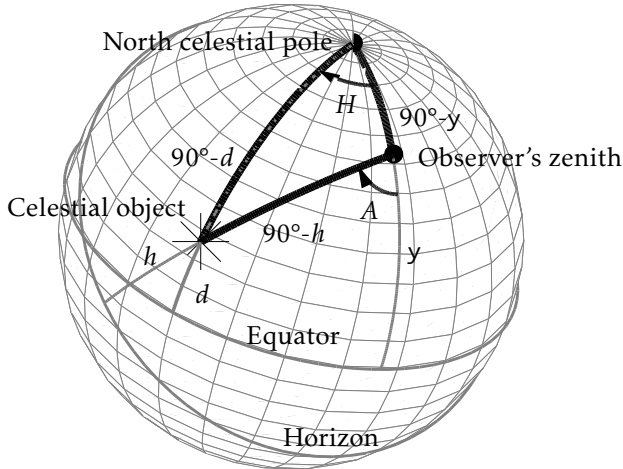


Figure 3.6: Triangle on the celestial sphere for deriving the transformation between the horizontal and the equatorial coordinate system.

With the spherical law of cosines (3.2) we also get

$$\begin{aligned} \cos(90^\circ - h) &= \cos(90^\circ - d)\cos(90^\circ - y) + \sin(90^\circ - d)\sin(90^\circ - y)\cos(H) \Rightarrow \\ \sin h &= \sin y \sin d + \cos y \cos d \cos H. \end{aligned} \quad (3.12a)$$

This is the key equation relating the altitude of the celestial object with the latitude and longitude of the observer enabling celestial navigation.

From the same triangle we can also derive the expression for the azimuth using (3.9)

$$\begin{aligned} \tan(180^\circ - A) &= \frac{\sin(H)}{-\cos(H)\cos(90^\circ - y) + \frac{\sin(90^\circ - y)}{\tan(90^\circ - d)}} \\ &= \frac{\sin(H)}{\cos(H)\sin(y) - \cos(y)\tan(d)}. \end{aligned} \quad (3.13)$$

Ecliptic Coordinate System

The *ecliptic coordinate system* has the orbital plane of the earth, called the *ecliptic*, as reference plane. The *ecliptic latitude* β is the angular distance from the ecliptic to the celestial object. Similar to the equatorial coordinate system, it has the vernal equinox as reference meridian and the *ecliptic longitude* λ measures the angular distance with respect to this meridian. The equatorial plane and the ecliptic plane are tilted relative to each other, referred to as the *obliquity of the ecliptic* and has a value of $\varepsilon = 23.4^\circ$.

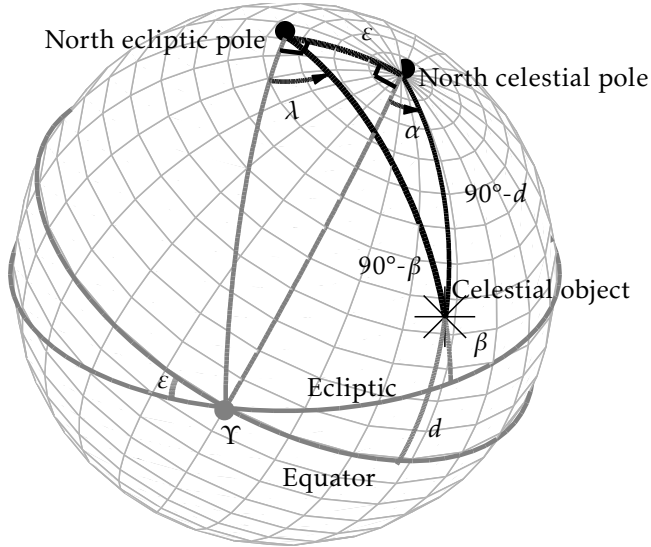


Figure 3.7: Triangle on the celestial sphere for deriving the transformation between the equatorial and the ecliptic coordinate system.

The transformation between the equatorial and the ecliptic coordinate system can be derived from another spherical triangle, see Figure 3.7. This spherical triangle combines the North celestial pole, the position of the celestial object and the North ecliptic pole. By using the law of cosines on this triangle we get an expression for the declination as a function of the ecliptic coordinates

$$\begin{aligned}\cos(90^\circ - d) &= \cos(90^\circ - \beta) \cos(\varepsilon) + \sin(90^\circ - \beta) \sin(\varepsilon) \cos(90^\circ - \lambda) \Rightarrow \\ \sin d &= \sin \beta \cos \varepsilon + \cos \beta \sin \varepsilon \sin \lambda.\end{aligned}\quad (3.14a)$$

By using (3.9) we can also find the right ascension

$$\begin{aligned}\tan(\alpha + 90^\circ) &= \frac{\sin(90^\circ - \lambda)}{-\cos(90^\circ - \lambda) \cos(\varepsilon) + \frac{\sin(\varepsilon)}{\tan(90^\circ - \beta)}} \Rightarrow \\ \tan(\alpha) &= \frac{\sin(\lambda) \cos(\varepsilon) - \sin(\varepsilon) \tan(\beta)}{\cos(\lambda)}.\end{aligned}\quad (3.14b)$$

Since the sun itself is in the ecliptic plane, its ecliptic longitude is zero⁵ $\beta = 0$. The transformation (3.14a) is therefore reduced to

$$\sin d = \sin \varepsilon \sin \lambda, \quad (3.15a)$$

$$\tan \alpha = \tan \lambda \cos(\varepsilon). \quad (3.15b)$$

⁵Due to perturbations caused by the moon, the ecliptic longitude of the sun is not identical to zero, but does not exceed 0.00033° (Meeus, 1991)

3.3 Time

Measuring time is an important task in astronomy. The time reckoning is based on two motions. The first is the rotation of the earth around its axis with a period time of 23 h 56 min 4 s, which is a *sidereal day*. The second is the orbit of the earth around the sun with a period time of 365.256 d, which we call *year*. During one sidereal day the apparent position of stars on the celestial sphere will return to their local meridian.

From the perspective of the earth, it is more natural to base our timekeeping on the apparent motion of the sun rather than that of the stars. Similarly to the sidereal day, the *solar day* is the time it takes for the sun to return to the same local meridian. Since the earth is rotating in the same direction as its orbital motion, there will be one more solar day than sidereal day during a year. That is since the orbit around the sun will contribute with one solar day during one year. On average, the length of the solar day will be 24 h.

Similarly, we use the *solar time*, which follows the apparent motion of the sun ⁶ and we define it as the hour angle of the sun plus 12 hours (such that a new day starts at midnight)

$$T = H + 12 \text{ h.} \quad (3.16)$$

However, the solar time does not flow at a constant rate. This effect has two reasons. First, the orbit of the earth around the sun is elliptic rather than circular, which makes the velocity of the earth along its orbit time varying. Second, the tilt of the earth's equator relative to the ecliptic makes the right ascension grow at an uneven rate, see (3.15b). Furthermore, it is inconvenient to have a time which does not increase at a constant rate. Therefore we also define the *mean solar time*, which does flow at a constant rate and where all days are 24 h. The difference between the solar time and the mean solar time is called the *equation of time* and it differs as much as 16 min.

3.4 Simplified Model

A rough, but workable model for the position of the sun can be derived by not including the effect provided by the equation of time explained above, but rather assume that the hour angle always increases at constant rate of 360° per 24 h. This approximation can also be found by using the following approximation, valid for small angles, in the transformation from the ecliptic to the equatorial coordinate system

$$\cos(\varepsilon) \approx 1 \quad \sin(\varepsilon) \approx \varepsilon, \quad (3.17a)$$

$$\cos(d) \approx 1 \quad \sin(d) \approx d. \quad (3.17b)$$

⁶This time is what a sundial would measure.

By using these approximations together with $\beta = 0$ in (3.14b) we get

$$\alpha \approx \lambda, \quad (3.18a)$$

$$d \approx \varepsilon \sin \lambda. \quad (3.18b)$$

By assuming a circular orbit of the earth around the sun, i.e. by assuming $e \approx 0$, the mean anomaly f and consequently also the ecliptic longitude λ will increase at a constant rate

$$\lambda \approx 360^\circ \frac{t}{P}, \quad (3.19a)$$

where t is the time since the vernal equinox and P is the orbital period of the earth around the sun. With these assumptions also the right ascension α as well as the hour angle will increase at constant rate according to (3.11)

$$t \approx \Theta_G - \alpha, \quad (3.20a)$$

$$H \approx t + 12 \text{ h} + x. \quad (3.20b)$$

Together with the angle (3.12a), the equations relating the longitude, latitude and time to the altitude of the sun can be summarized as

$$\sin h = \sin y \sin d + \cos y \cos d \cos H, \quad (3.21a)$$

$$H \approx \bar{t} + 12 \text{ h} + x, \quad (3.21b)$$

$$d \approx -\varepsilon \cos \frac{\bar{t}}{P}, \quad (3.21c)$$

where \bar{t} is the time since the last winter solstice. The times P , t and \bar{t} are given in hours.

3.5 Summary and Connections

In this chapter the fundamental principle for how to derive the apparent motion of celestial objects has been presented. This motion is a consequence of two dynamics: (1) the earth's rotation around its axis and (2) the earth's orbit around the sun, where the equations for the second one can be derived from Kepler's laws. Further, to describe this motion from the perspective of the observer, several coordinate transformations are needed, where the transformations are based on spherical geometry. Finally, a simplified model has been proposed, which assumes that the solar time flows at a constant rate. This model has been used in Paper D to derive equations for sunrise and sunset suitable for localizing migrating birds.

4

Concluding Remarks

In the first part of this thesis an introduction to the research field and its applications was given. In the first part the relevant theory for accomplishing the modeling work was also presented. In the second part the results were presented and the conclusions are summarized in Section 4.1. Ideas for future directions of the research are provided in Section 4.2.

4.1 Conclusions

In the first three papers the problem of localizing magnetic objects based on measurements of their induced magnetic field has been investigated. The models introduced in these papers were all based on the electromagnetic theory presented in Chapter 2. However, to come up with a model which works with real data is not straightforward. Especially, taking the target extent into consideration is challenging. This has been solved differently in each of the three papers.

In Paper A, a sensor model based on the magnetic dipole model was introduced. The target extent has been modeled with a row of dipoles where the length of the row is related to the length of the target. The paper also proposes a model separating the contribution of hard iron and soft iron to the induced magnetic field, which enables a heading direction dependent model. The paper also presents an observability analysis of the dipole model. The proposed model has been validated with a selection of dedicated field experiments showing good performance for small vehicles. For larger vehicles challenging modeling work still remains.

In Paper B, only the problem of classifying driving direction of a vehicle has been analyzed. Similar to Paper A, the theoretical starting point was the magnetic dipole model. However, instead of using the full dipole model for estimating po-

sition and velocity as in Paper A, a nonlinear transformation of the measurement has been derived. Based on the dipole model, this transformed data has theoretically and experimentally been proven to be sensitive to the driving direction of the vehicle, but insensitive to other scenario dependent parameters, such as velocity, magnetic signature and target extent. Note that in contrast to the model in Paper A, this model works excellent on large vehicles. The model has been validated on a total number of 511 vehicles and outperforms a standard likelihood test.

The model presented in Paper C is not restricted to the parametric dipole model. It uses a non-parametric modeling technique to model extended magnetic objects and their induced magnetic field. In contrast to the first two papers, this model is more suitable for stationary magnetic objects. The model has been validated on both simulated and experimental data showing ability to localize and determine the geometrical shape of magnetic structures.

In Paper D, a framework for localizing migrating birds using light logger data has been proposed. The sensor model is based on a simplified version of the astronomical formulas governing the position of the sun. In contrast to the first three papers, a stochastic motion model has been used. The corresponding estimation problem has been solved with a Rao-Blackwellized particle filter. The method has been applied to real data and compared with the existing method with promising results.

4.2 Future Work

Different directions are possible for future research related to the material presented in this thesis. These directions are divided into the three different application areas, that have been analyzed in this thesis.

Traffic surveillance

Future work should focus on finding solutions for the cases that are hard to resolve, such as multiple vehicles and, possibly by fusing information from other sensor types. Further, so far the detection problem has not been analyzed. Here, standard methods from the literature can be used, for example an adaptive thresholding technique presented by Cheung and Varaiya (2007). In future work the detection problem should be included, resulting in a full system for localizing vehicles in a wireless sensor network. Finally, implementation in real sensor nodes should be targeted and the performance in a real time system analyzed.

Magnetic localization mapping in indoor environments

The Bayesian nonparametric model used for describing magnetic structures is flexible in the sense that objects with different shapes can be estimated. However, the model is not flexible enough to model data having a big diversity of different characteristic length scales and amplitudes. Therefore, in future work, the Bayesian nonparametric model will be extended to handle more complex environments. One promising idea is to extend the model by using a so called hierar-

chical Dirichlet process (Teh et al., 2006). Others ideas are to use a new concept of multiresolution Gaussian Processes (Fox and Dunson, 2012) or a infinite mixture of Gaussian process experts (Rasmussen and Ghahramani, 2002).

Geolocation using light levels

In this work, the light intensity data has in a first step been preprocessed by extracting time of sunrise and sunset. In this preprocessing, important information gets lost about the length of dawn and dusk, which also partly reveals the location. Furthermore, this preprocessing step includes manual work by removing outliers due to shading behind bushes and other vegetation.

Future work should address these problems using the light intensity data as measurement and do a measurement update at each light intensity sample during dawn and dusk. Also the outliers should be modeled and detected in an automated manner. The light intensity measurement is also weather dependent. It should therefore also be analyzed if any performance can be gained by fusing with information from weather databases. The filtering solution shall be extended to a Rao-Blackwellized particle smoother (RBPS) to increase the estimation performance. We will investigate the use of a new RBPS (Lindsten et al., 2013), which is able to handle the singular process noise present in the model. Finally, the sensor model should be extended by including the effects from astronomy that have so far been neglected, see Section 3.5.

A

Dipole Derivation

Consider a region V with localized current density. That means, charged particles can move within the region, but neither leave it nor be added to it. According to (2.4), this current density gives rise to an induced magnetic field outside the region (see Figure 2.1).

Since $\nabla \cdot \mathbf{B} = 0$ everywhere, \mathbf{B} must be the curl of some vector field $\mathbf{A}(\mathbf{r})$, called the *vector potential*

$$\mathbf{B}(\mathbf{r}) = \nabla \times \mathbf{A}(\mathbf{r}). \quad (\text{A.1})$$

Substituting (A.1) into (2.4a) gives

$$\nabla \times (\nabla \times \mathbf{A}(\mathbf{r})) = \mu_0 \mathbf{J} \quad \Rightarrow \quad (\text{A.2a})$$

$$\nabla(\nabla \cdot \mathbf{A}(\mathbf{r})) - \nabla^2 \mathbf{A}(\mathbf{r}) = \mu_0 \mathbf{J}. \quad (\text{A.2b})$$

Since (A.1) only specifies the curl of \mathbf{A} , the freedom of the so-called gauge transformation allows one to make $\nabla \cdot \mathbf{A}$ have any convenient functional form. With the choice $\nabla \cdot \mathbf{A} = 0$, we get the following Poisson's equation

$$\nabla^2 \mathbf{A} = -\mu_0 \mathbf{J}, \quad (\text{A.3})$$

which has the solution

$$\mathbf{A}(\mathbf{r}) = \frac{\mu_0}{4\pi} \int \frac{\mathbf{J}(\mathbf{r}')}{\|\mathbf{r} - \mathbf{r}'\|} d^3 r'. \quad (\text{A.4})$$

Since $\mathbf{J}(\mathbf{r}') \neq \mathbf{0}$ only in the region of the localized current density V , we have

$$\mathbf{A}(\mathbf{r}) = \frac{\mu_0}{4\pi} \int_V \frac{\mathbf{J}(\mathbf{r}')}{\|\mathbf{r} - \mathbf{r}'\|} d^3 r'. \quad (\text{A.5})$$

Furthermore, the denominator in (A.5) can be expanded in powers of \mathbf{r}' . With $\|\mathbf{r}\| > \|\mathbf{r}'\|$ this will be

$$\frac{1}{\|\mathbf{r} - \mathbf{r}'\|} = \frac{1}{\|\mathbf{r}\|} + \nabla \left(\frac{1}{\|\mathbf{r}\|} \right) \cdot (-\mathbf{r}') + \dots = \frac{1}{\|\mathbf{r}\|} + \frac{\mathbf{r} \cdot \mathbf{r}'}{\|\mathbf{r}\|^3} + \dots \quad (\text{A.6})$$

where $r = \|\mathbf{r}\|$. Using this Taylor expansion in (A.4) results in

$$A_i(\mathbf{r}) = \frac{\mu_0}{4\pi} \left(\frac{1}{\|\mathbf{r}\|} \int_V J_i(\mathbf{r}') d^3 r' + \frac{\mathbf{r}}{\|\mathbf{r}\|^3} \cdot \int_V J_i(\mathbf{r}') \mathbf{r}' d^3 r' + \dots \right). \quad (\text{A.7})$$

Due to the fact that the current density $\mathbf{J}(\mathbf{r})$ is localized and obeys the static continuity condition $\nabla \cdot \mathbf{J} = 0$, Gauss' theorem makes the first term in (A.7) zero. Furthermore, it can be shown that

$$\mathbf{r} \cdot \int_V \mathbf{r}' J_i(\mathbf{r}') d^3 r' = (\mathbf{m} \times \mathbf{r})_i, \quad (\text{A.8})$$

where \mathbf{m} is the *magnetic dipole moment*

$$\mathbf{m} = \frac{1}{2} \int_V \mathbf{r}' \times \mathbf{J}(\mathbf{r}') d^3 r'. \quad (\text{A.9})$$

The details of these steps are clearly outlined in Jackson (1998). By truncating (A.7) and using (A.9) in (A.7), we get

$$\mathbf{A}(\mathbf{r}) = \frac{\mu_0}{4\pi} \frac{\mathbf{m} \times \mathbf{r}}{\|\mathbf{r}\|^3}. \quad (\text{A.10})$$

The induced magnetic field can be calculated directly by evaluating the curl of (A.10),

$$\mathbf{B}(\mathbf{r}) = \frac{\mu_0}{4\pi} \frac{3(\mathbf{r} \cdot \mathbf{m})\mathbf{r} - \|\mathbf{r}\|^2 \mathbf{m}}{\|\mathbf{r}\|^5} \quad (\text{A.11})$$

When $\|\mathbf{r}\| \gg \|\mathbf{r}'\|$ the truncation of the Taylor expansion in (A.6) makes a good approximation, i.e. if the characteristic length of region V is small in comparison to the distance from the region to the observer at point P , see Figure 2.1.

Bibliography

- S. Åkesson, R. Klaassen, J. Holmgren, J. W. Fox, and A. Hedenström. Migration Route and Strategies in a Highly Aerial Migrant, the Common Swift *Apus apus*, Revealed by Light-Level Geolocators. *Plos One*, 7(7), 2012.
- E. Almqvist, D. Eriksson, A. Lundberg, E. Nilsson, N. Wahlström, E. Frisk, and M. Krysander. Solving the ADAPT benchmark problem - A student project study. In *21st International Workshop on Principles of Diagnosis (DX-10)*, Portland, Oregon, USA, October 2010.
- W.H. Barton. *An introduction to celestial navigation*. Addison-Wesley press, inc., 1943.
- F. Caron, E. Duflos, D. Pomorski, and P. Vanheeghe. Gps/imu data fusion using multisensor kalman filtering: introduction of contextual aspects. *Information Fusion*, 7(2):221–230, 2006.
- D.K. Cheng. *Field and wave electromagnetics*. Reading, Massachusetts : Addison Wesley, 2 edition, 1989.
- S.-Y. Cheung and P. Varaiya. Traffic surveillance by wireless sensor networks: Final report. Technical report, California Path Program, Institute of Transportation Studies, University of California, Berkeley, 2007.
- L. Correia and D. Jonsson. A Real-time Watercolor Simulation for a Novel Tracking Device. Master's thesis, Linköping University, Department of Science and Technology, 2012.
- C.H. Cotter. *A history of nautical astronomy*, volume 1. Hollis & Carter, 1968.
- G. Deak, K. Curran, and J. Condell. A survey of active and passive indoor localisation systems. *Computer Communications*, 2012.
- B. Di Bartolo. *Classical theory of electromagnetism*. World Scientific Publishing Company Incorporated, 2004.
- P.A. Ekstrom. An advance in geolocation by light. *Memoirs of the National Institute of Polar Research*, 58:210–226, 2004.

- R. Fenn. *Geometry*. Springer Verlag, 1993.
- E. Fox and D.B. Dunson. Multiresolution gaussian processes. In *Advances in Neural Information Processing Systems 25*, pages 746–754. 2012.
- Y. Gu, A. Lo, and I. Niemegeers. A survey of indoor positioning systems for wireless personal networks. *IEEE Communications Surveys and Tutorials*, 11(1):13–32, 2009. cited By (since 1996) 124.
- F. Gustafsson and N. Wahlström. Method and device for pose tracking using vector magnetometers, 2012. Patent. Under revision.
- R.D. Hill. Theory of geolocation by light levels. In *Elephant seals: population ecology, behavior, and physiology*. University of California Press, Berkeley, pages 227–236. University of California Press, 1994.
- J.D. Hol, T.B. Schön, and F. Gustafsson. Modeling and calibration of inertial and vision sensors. *The International Journal of Robotics Research*, 29(2-3):231–244, 2010.
- R. Hostettler, M. Lundberg, and W. Birk. A system identification approach to modeling of wave propagation in pavements. In *16th IFAC Symposium on System Identification*, Brussels, July 2012.
- J.D. Jackson. *Classical Electrodynamics*. John Wiley and Sons, Inc., 3 edition, 1998.
- R. Karlsson and F. Gustafsson. Bayesian surface and underwater navigation. *Signal Processing, IEEE Transactions on*, 54(11):4204–4213, 2006.
- H. Karttunen. *Fundamental astronomy*. Springer Verlag, 2003.
- M. Kok, N. Wahlström, T.B. Schön, and F. Gustafsson. MEMS-based inertial navigation based on a magnetic field map. In *Proceedings of the 38th International Conference on Acoustics, Speech, and Signal Processing (ICASSP)*, Vancouver, Canada, May 2013. Submitted.
- E. Le Grand and S. Thrun. 3-axis magnetic field mapping and fusion for indoor localization. In *Proceedings of IEEE International Conference on Multisensor Fusion and Integration for Intelligent Systems (MFI)*, pages 358–364. IEEE, 2012.
- J. Lenz and S. Edelstein. Magnetic sensors and their applications. *Sensors Journal, IEEE*, 6:631–649, Jun 2006.
- L. Lindsten, P. Bunch, S.J. Godsill, and T.B. Schön. Rao-Blackwellized particle smoothers for mixed linear/nonlinear state-space models. In *Proceedings of the 38th International Conference on Acoustics, Speech, and Signal Processing (ICASSP)*, Vancouver, Canada, May 2013. Submitted.
- J. C. Maxwell. A dynamical theory of the electromagnetic field. *Philosophical Transactions of the Royal Society of London*, 155:459–513, 1865.

- J.H. Meeus. *Astronomical algorithms*. Willmann-Bell, Incorporated, 1991.
- C.E. Rasmussen and Z. Ghahramani. Infinite mixtures of gaussian process experts. *Advances in neural information processing systems*, 2:881–888, 2002.
- B.J.M. Stutchbury, S.A. Tarof, T. Done, E. Gow, P.M. Kramer, J. Tautin, J.W. Fox, and V. Afanasyev. Tracking long-distance songbird migration by using geolocators. *Science*, 323(5916):896, 2009.
- Y.W. Teh, M.I. Jordan, M.J. Beal, and D.M. Blei. Hierarchical Dirichlet processes. *Journal of the American Statistical Association*, 101(476):1566–1581, 2006.
- J. Torres-Solis, T.H. Falk, and T. Chau. A review of indoor localization technologies: towards navigational assistance for topographical disorientation. *Ambient Intelligence*, pages 51–84, 2010.
- I. Vallivaara, J. Haverinen, A. Kemppainen, and J. Roning. Magnetic field-based SLAM method for solving the localization problem in mobile robot floor-cleaning task. In *Proceedings of the 15th International Conference on Advanced Robotics (ICAR)*, pages 198–203, Tallin, Estonia, June 2011.
- D. Vissière, A.P. Martin, and N. Petit. Using magnetic disturbances to improve IMU-based position estimation. In *Proceedings of the European Control Conference*, pages 2853–2858, Kos, Greece, July 2007.
- N. Wahlström. Target Tracking using Maxwell’s Equations. Master’s thesis, Linköping University, Automatic Control, 2010.
- N. Wahlström and F. Gustafsson. Magnetometer modeling and validation for tracking metallic targets. *IEEE Transactions on Signal Processing*, 2012. Under revision.
- N. Wahlström, J. Callmer, and F. Gustafsson. Magnetometers for tracking metallic targets. In *Proceedings of 13th International Conference on Information Fusion (FUSION)*, Edinburgh, Scotland, July 2010.
- N. Wahlström, J. Callmer, and F. Gustafsson. Single target tracking using vector magnetometers. In *Proceedings of the International Conference on Acoustics, Speech and Signal Processing (ICASSP)*, pages 4332–4335, Prague, Czech Republic, May 2011.
- N. Wahlström, F. Gustafsson, and S. Åkesson. A Voyage to Africa by Mr Swift. In *Proceedings of the 15th International Conference on Information Fusion (FUSION)*, pages 808–815, Singapore, July 2012a.
- N. Wahlström, R. Hostettler, F. Gustafsson, and W. Birk. Rapid classification of vehicle heading direction with two-axis magnetometer. In *Proceedings of the International Conference on Acoustics, Speech and Signal Processing (ICASSP)*, pages 3385–3388, Kyoto, Japan, March 2012b.
- N. Wahlström, R. Hostettler, F. Gustafsson, and W. Birk. Classification of driving

- direction in traffic surveillance using magnetometers. *IEEE Transactions on Intelligent Transportation Systems*, 2012c. Submitted.
- N. Wahlström, M. Kok, T.B. Schön, and F. Gustafsson. Modeling magnetic fields using Gaussian processes. In *Proceedings of the the 38th International Conference on Acoustics, Speech, and Signal Processing (ICASSP)*, Vancouver, Canada, May 2013. Submitted.
- O.J. Woodman. An introduction to inertial navigation. *University of Cambridge, Computer Laboratory, Tech. Rep. UCAMCL-TR-696*, 2007.
- H. Zhang and F. Martin. Robotic mapping assisted by local magnetic field anomalies. In *Proceedings of the IEEE Conference on Technologies for Practical Robot Applications (TePRA)*, pages 25–30, Woburn, USA, April 2011.

Part II

Publications

Paper A

Magnetometer Modeling and Validation for Tracking Metallic Targets

Authors: Niklas Wahlström, and Fredrik Gustafsson

Edited version of the paper:

N. Wahlström and F. Gustafsson. Magnetometer modeling and validation for tracking metallic targets. *IEEE Transactions on Signal Processing*, 2012. Under revision.

Early versions of this work were presented in:

N. Wahlström, J. Callmer, and F. Gustafsson. Magnetometers for tracking metallic targets. In *Proceedings of 13th International Conference on Information Fusion (FUSION)*, Edinburgh, Scotland, July 2010.

N. Wahlström, J. Callmer, and F. Gustafsson. Single target tracking using vector magnetometers. In *Proceedings of the International Conference on Acoustics, Speech and Signal Processing (ICASSP)*, pages 4332–4335, Prague, Czech Republic, May 2011.

Magnetometer Modeling and Validation for Tracking Metallic Targets

Niklas Wahlström, and Fredrik Gustafsson

Dept. of Electrical Engineering,
Linköping University,
SE-581 83 Linköping, Sweden
{nikwa, fredrik}@isy.liu.se

Abstract

With the electromagnetic theory as basis, we present a sensor model for three-axis magnetometers suitable for localization and tracking as required in intelligent transportation systems and security applications. The model depends on a physical magnetic dipole model of the target and its relative position to the sensor. Both point target and extended target models are provided as well as a target orientation dependent model. The suitability of magnetometers for tracking is analyzed in terms of local observability and the Cramér Rao lower bound as a function of the sensor positions in a two sensor scenario. The models are validated with real field test data taken from various road vehicles which indicate excellent localization as well as identification of the magnetic target model suitable for target classification. These sensor models can be combined with a standard motion model and a standard nonlinear filter to track metallic objects in a magnetometer network.

1 Introduction

Tracking and classification of targets are primary concerns in automated surveillance and security systems. The tracking and classification information can be used for statistical purposes, i.e. counting number of targets of a specific type and registration of their velocities and directions of arrival. In this work we will focus on metallic targets.

One way of sensing metallic objects is by making use of their magnetic properties. We know that metallic objects induce a magnetic field partly due to its permanently magnetized ferromagnetic content and partly due to the deflection of the earth magnetic field (Jackson, 1998). This induced magnetic field can be measured with distributed passive magnetometers (Lenz, 1990; Lenz and Edelstein, 2006).

For moving metallic vehicles, the magnetometer measurements will vary in time, which results in a time dependent signal. Like in other common tracking application based on radar, time difference of arrival and received signal strength, this signal depends on the position, speed, orientation and target specific parameters. The difference between the applications is summarized in the sensor model that relates the quantities to the observations. The same motion models and filters can be used in all these application. However, we do not focus on suggesting particular motion models and filters since these choices are standard in literature. Instead, we focus on the application specific fundamental questions of observability and geometry for the sensor model.

The simplest far-field model for the metallic vehicle is to approximate it as a moving magnetic dipole, which is parametrized with the magnetic dipole moment \mathbf{m} that can be interpreted as the magnetic signature of the vehicle. This dipole model has previously been used for classification and target tracking of ground targets by Wynn (1999); Casalegno (2002); Kozick and Sadler (2007a,b, 2008); Christou and Jacyna (2010); Wahlström et al. (2010, 2011); Rakijas (2001); Merlat and Naz (2003); Edelstein (2004); Birsan (2004, 2005). In a near-field scenario the signal structure is much more complex where nonparametric methods have been shown to be successful. Cheung and Varaiya (2007); Cheung et al. (2005) have done an extensive investigation is presented, where the measured signal itself has been interpreted as the magnetic signature, which can be used for classification and re-identification of the vehicle at a different location.

Furthermore, several studies have been done exploring the use of underwater magnetometers for tracking of vessels (Daya et al., 2005; Birsan, 2006; Callmer et al., 2009), where Callmer et al. (2009) have used the dipole model not only for localizing the vessel, but also for estimating the positions of the sensors. Birsan (2006) has used a Bayesian match-field approach, which takes the attenuation of the seawater into consideration.

As in the work by Wynn (1999); Casalegno (2002); Kozick and Sadler (2007a,b, 2008); Christou and Jacyna (2010); Wahlström et al. (2010, 2011); Rakijas (2001); Merlat and Naz (2003); Edelstein (2004); Birsan (2004, 2005); Callmer et al. (2009), this work will be based on the dipole model. However, we will generalize many of the assumptions that previously have been made:

- Prior work by Casalegno (2002); Kozick and Sadler (2007a,b, 2008); Christou and Jacyna (2010); Wahlström et al. (2010, 2011); Rakijas (2001); Merlat and Naz (2003); Edelstein (2004); Birsan (2004, 2005) is constrained to a single dipole point target model, which does not included the the geometrical extend of the target. We suggest a model with multiple dipoles. This model was proposed by Wynn (1999) without being illustrated on simulated or real data, which will be provided in this work.
- Work by Wynn (1999); Casalegno (2002); Kozick and Sadler (2007a,b, 2008); Christou and Jacyna (2010); Wahlström et al. (2010) is based on a linear motion assumptions, which simplifies the modeling of the dipole moment \mathbf{m} .

However, for other motions where the target orientation changes over time, the dependency on \mathbf{m} will more complicated. One way of solving this is to marginalize the dipole moment as done by Rakijas (2001); Merlat and Naz (2003); Edelstein (2004). However, this work will explicitly describe the \mathbf{m} as a function of the target orientation.

- In many papers (Birsan, 2004, 2005; Merlat and Naz, 2003; Edelstein, 2004; Kozick and Sadler, 2008; Callmer et al., 2009) the theory is illustrated on simulated data, whereas this work will compare the theory with experimental data.

We will derive a general sensor model for extended magnetic targets with target orientation dependent dipole moments observed in an arbitrary magnetometer network, where we validate the models using statistical tools for a variety of vehicles.

Furthermore, Birsan (2005) has adressed the problem with lack of observability for a one-sensor scenario. Our work will more precisely describe this unobservable manifold. Also, a measure of the optimal sensor deployment is discussed in terms of the *Cramér Rao Lower Bound* (CRLB) as a function of the sensor positions in a two-sensor scenario.

The paper outline is as follows: Section 2 describes the sensor model and its extensions. In Section 3 a constant velocity tracking model is presented and compared with other models from the literature based on the same assumption. In Section 4 observability and sensor deployment is discussed and in Section 5 the estimation methods are summarized. A validation of the sensor model based on experimental data is provided in Section 6. The paper closes with conclusions and proposals for future work.

2 Theoretical Sensor Model

In the statistical signal processing framework, a sensor model of a time-invariant system is given by

$$\mathbf{y}_k = \mathbf{h}(\mathbf{x}_k) + \mathbf{e}_k, \quad (1)$$

where \mathbf{y}_k is the measurement, \mathbf{x}_k is the state of the system and \mathbf{e}_k is measurement noise, all at time instant kT , T being the sample period. This section will present and discuss different sensor models suitable for target tracking of magnetic objects.

2.1 Single Sensor Point Target Model

Any magnetic target will induce a magnetic field, which can be measured by a magnetometer. By approximating the target as a magnetic dipole (Jackson, 1998), this field can be modeled as a magnetic dipole field. An expression of this field can be derived from Maxwell's equations (Maxwell, 1865) (for a derivation see

for example Jackson (1998)) and gives the following nonlinear model

$$\mathbf{h}(\mathbf{x}_k) = \mathbf{B}_0 + \frac{\mu_0}{4\pi} \frac{3(\mathbf{r}_k \cdot \mathbf{m}_k)\mathbf{r}_k - \|\mathbf{r}_k\|^2 \mathbf{m}_k}{\|\mathbf{r}_k\|^5} \quad (2a)$$

$$= \mathbf{B}_0 + \mathbf{J}^{\mathbf{m}}(\mathbf{r}_k)\mathbf{m}_k, \quad (2b)$$

with

$$\mathbf{J}^{\mathbf{m}}(\mathbf{r}_k) = \frac{\mu_0}{4\pi\|\mathbf{r}_k\|^5} (3\mathbf{r}_k\mathbf{r}_k^{\top} - \|\mathbf{r}_k\|^2 \mathbf{I}_3), \quad (2c)$$

where \mathbf{B}_0 is a bias, \mathbf{r}_k is the position of the target relative to the sensor, \mathbf{m}_k is the magnetic dipole moment of the target and $\mathbf{e}_k \sim \mathcal{N}(\mathbf{0}, \mathbf{R})$ white Gaussian noise. The total sensor model is then given by

$$\mathbf{y}_k = \mathbf{h}(\mathbf{x}_k) + \mathbf{e}_k \quad (2d)$$

$$\text{with } \mathbf{x}_k = [\mathbf{B}_0^{\top} \quad \mathbf{r}_k^{\top} \quad \mathbf{m}_k^{\top}]^{\top}, \quad (2e)$$

The dipole model is an approximation of the induced magnetic field by considering the target to be a point source. This approximation is valid if the target is far from the sensor compared to its size, for further discussion see Section 2.3.

The bias \mathbf{B}_0 will in theory be constant and equal to the earth magnetic field. However, in practice it also includes the magnetic distortion induced by other metallic objects in the environment, which we assume to be constant. Furthermore, the bias \mathbf{B}_0 also includes a magnetic sensor bias, which slightly depends on temperature. This temperature may vary over time due to changing weather condition and amount of daylight exposed to the sensor (Cheung and Varaiya, 2007). However, this drift is slowly varying and is assumed to be constant during the time it takes for a vehicle to pass the sensor.

2.2 Multiple Sensor Model

The sensor model (2) can easily be extended to handle multiple sensors by introducing

$$\mathbf{h}_j(\mathbf{x}_k) = \mathbf{B}_{0,j} + \mathbf{J}^{\mathbf{m}}(\mathbf{r}_k - \boldsymbol{\theta}_j)\mathbf{m}_k \quad (3a)$$

where $\boldsymbol{\theta}_j$ and $\mathbf{B}_{0,j}$ are the position and the bias of the j th sensor, respectively.

The total sensor model is then given by

$$\mathbf{y}_{j,k} = \mathbf{h}_j(\mathbf{x}_k) + \mathbf{e}_{j,k} \quad (3b)$$

$$\text{with } \mathbf{x}_k = [\mathbf{B}_{0,1:J}^{\top} \quad \mathbf{r}_k^{\top} \quad \mathbf{m}_k^{\top}]^{\top}, \quad (3c)$$

where $\mathbf{e}_{j,k}$ is the measurement noise of the j th sensor.

2.3 Extended Target Model

The dipole model (2b) approximates the target with a single magnetic dipole and can as such be seen as a point target model. However, this is a fairly rough approximation since vehicles do have a geometrical extension. By parameterizing

the extended target with multiple dipoles, a more accurate model can be obtained. By that we get an extended target model. Consider each dipole to be placed at $\Delta \mathbf{r}_k^i$, relative to the center of the target \mathbf{r}_k and having the dipole vector \mathbf{m}_k^i . Then the point target model (2b) can be extended as

$$\mathbf{h}(\mathbf{x}_k) = \mathbf{B}_0 + \sum_{i=1}^d \mathbf{J}^{\mathbf{m}}(\mathbf{r}_k + \Delta \mathbf{r}_k^i) \mathbf{m}_k^i \quad (4)$$

where d is the number of dipoles. The extended target model in (4) reduces to a single target model (2b) if the relative positions $\Delta \mathbf{r}_k^i$ are much smaller than \mathbf{r}_k . The influence of the target extension can be analyzed by applying a Taylor series expansion of $\mathbf{J}^{\mathbf{m}}(\mathbf{r}_k)$ in (2c) around \mathbf{r}_k . By truncating the Taylor series after the second term, we reach the approximation

$$\begin{aligned} \mathbf{h}(\mathbf{x}_k) &\approx \mathbf{B}_0 + \sum_{i=1}^d \left(\mathbf{J}^{\mathbf{m}}(\mathbf{r}_k) + \underbrace{\mathbf{V}_{\mathbf{r}}(\mathbf{J}^{\mathbf{m}}(\mathbf{r}_k)) \Delta \mathbf{r}_k^i}_{\triangleq \mathbf{J}^{\mathbf{r}}(\mathbf{r}_k, \Delta \mathbf{r}_k^i)} \right) \mathbf{m}_k^i \\ &= \mathbf{B}_0 + \mathbf{J}^{\mathbf{m}}(\mathbf{r}_k) \sum_{i=1}^d \left(\mathbf{I}_3 + (\mathbf{J}^{\mathbf{m}}(\mathbf{r}_k))^{-1} \mathbf{J}^{\mathbf{r}}(\mathbf{r}_k, \Delta \mathbf{r}_k^i) \right) \mathbf{m}_k^i, \end{aligned} \quad (5)$$

where we have defined

$$\{\mathbf{V}_{\mathbf{x}} \mathbf{f}(\mathbf{x})\}_{i_1, \dots, i_{n+1}} = \frac{\partial}{\partial x_{i_{n+1}}} f_{i_1, \dots, i_n}(\mathbf{x}) \quad (6)$$

and $\mathbf{J}^{\mathbf{r}}(\cdot, \cdot)$ is given by (30b). Further, it can be shown that

$$\|(\mathbf{J}^{\mathbf{m}}(\mathbf{r}_k))^{-1} \mathbf{J}^{\mathbf{r}}(\mathbf{r}_k, \Delta \mathbf{r}_k^i)\|_2 \leq \frac{8 \|\Delta \mathbf{r}_k^i\|_2}{7 \|\mathbf{r}_k\|_2} \quad (7)$$

and with $\|\Delta \mathbf{r}_k^i\|_2 \ll \|\mathbf{r}_k\|_2$ we arrive at the point target model

$$\mathbf{h}(\mathbf{x}_k) \approx \mathbf{J}^{\mathbf{m}}(\mathbf{r}_k) \sum_{i=1}^d \mathbf{m}_k^i = \mathbf{J}^{\mathbf{m}}(\mathbf{r}_k) \mathbf{m}_k, \quad (8)$$

where the dipole moment \mathbf{m}_k in point target model is related to the dipole moments \mathbf{m}_k^i in the extended target models as

$$\mathbf{m}_k = \sum_{i=1}^d \mathbf{m}_k^i. \quad (9)$$

Thus, the point target model is valid if the distance between the target and the sensor is much larger than the characteristic length of the target, which has also been stated by Jackson (1998). However, if this is not the case, an extended target model might be considered.

2.4 Uniformly Linear Array of Dipoles

In this work, a row of dipoles will be used to describe the target extent. Since a vehicle normally has its largest geometrical extension in the same direction as its course, a row of equidistantly distributed dipoles along the velocity vector \mathbf{v}_k will be considered (see Figure 1). The velocity vector \mathbf{v}_k will later be included in the dynamic description in Section 3. Furthermore, the size of the object is unknown,

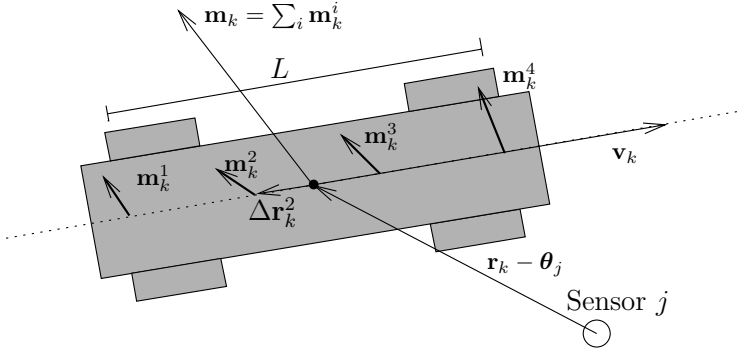


Figure 1: The vehicle parametrized with $d = 4$ dipoles aligned in a row in the direction of the vehicle course \mathbf{v}_k . All dipoles are equidistantly distributed with the interval $L/(d - 1)$, i.e. a total length of L .

thus the distance between the first and the last dipole L has to be regarded as a parameter. By combining this with the multiple sensor model (3) we get

$$\mathbf{h}_j^d(\mathbf{x}_k) = \mathbf{B}_{0,j} + \sum_{i=1}^d \mathbf{J}^m(\mathbf{r}_k - \boldsymbol{\theta}_j + \Delta \mathbf{r}_k^i) \mathbf{m}_k^i \quad (10a)$$

with

$$\Delta \mathbf{r}_k^i = \left(i - \frac{d+1}{2} \right) \frac{L}{d-1} \frac{\mathbf{v}_k}{\|\mathbf{v}_k\|}. \quad (10b)$$

The total sensor model is given by

$$\mathbf{y}_{j,k} = \mathbf{h}_j^d(\mathbf{x}_k) + \mathbf{e}_{j,k} \quad (10c)$$

$$\text{with } \mathbf{x}_k = \left[(\mathbf{B}_{0,1:j})^\top \quad \mathbf{r}_k^\top \quad \mathbf{v}_k^\top \quad (\mathbf{m}_k^{1:d})^\top \quad L \right]^\top. \quad (10d)$$

Note that if either the length is $L = 0$ or the number of dipoles is $d = 1$, the model (10) will be equivalent with the point target model presented in (2).

2.5 Target Orientation Dependent Model

The magnetic dipole moment \mathbf{m}_k will also depend on the orientation of the vehicle. To describe this dependency, the source of the magnetization has to be

decomposed into one hard iron contribution and one soft iron contribution as done by Casalegno (2002); Merlat and Naz (2003).

We know that metallic objects induce a magnetic field partly due to the ferromagnetic content (hard iron) and partly due to the deflection of the earth magnetic field (soft iron). The magnetization due to the hard iron can be represented with a magnetic dipole moment \mathbf{m}_0 , which is independent of the external magnetic field and will thus always be constant in the reference frame of the vehicle. Since the sensors have the same reference frame as the world, which is not the same as the one of the vehicle, a transformation between these two reference frames has to be found. Generally, the heading Ψ , banking ϕ and inclination θ angles are used to define the relative orientation of a vehicle with respect to world coordinates. Here, the world coordinates are aligned with the magnetic north, see Figure 2. In this work, no banking and inclination are considered since we assume that the road is flat, i.e. it does neither bank nor incline. Furthermore, any slip is neglected. Consequently, the heading Ψ_k uniquely determines the orientation of the vehicle with respect to the sensors and is defined as

$$\Psi_k = \arctan2(v_k^y, v_k^x), \quad (11)$$

with $\arctan2$ being the four quadrant arc-tangent and where v_k^x and v_k^y are the x and y components of the velocity vector \mathbf{v}_k , respectively. Now, with the rotation matrix

$$Q(\Psi_k) = \begin{bmatrix} \cos \Psi_k & -\sin \Psi_k & 0 \\ \sin \Psi_k & \cos \Psi_k & 0 \\ 0 & 0 & 1 \end{bmatrix}, \quad (12)$$

the hard iron contribution of magnetic dipole moment can be described as

$$\mathbf{m}_k^{\text{hard}} = Q(\Psi_k)\mathbf{m}_0. \quad (13)$$

On the other hand, the magnetization due to the soft iron is more complicated. For an isotropic medium (a spherical shell for example), the induced magnetic dipole moment \mathbf{m}_{soft} is parallel to the earth magnetic field \mathbf{B}_0

$$\mathbf{m}_k^{\text{soft}} = \frac{D}{\mu_0} \mathbf{B}_0, \quad (14)$$

with D being a target characteristic scalar constant.

However, in general the moment induction is a non-isotropic process and its description requires a symmetric 3×3 -matrix P , which is known as the polarizability tensor (Jackson, 1998). In world coordinates this tensor reads $Q(\Psi_k)PQ^T(\Psi_k)$ and we have

$$\mathbf{m}_k^{\text{soft}} = \frac{1}{\mu_0} Q(\Psi_k)PQ^T(\Psi_k)\mathbf{B}_0.$$

Since a symmetric 3×3 -matrix has 6 unknowns, this would heavily enlarge our state space dimension (and presumably lead to unobservability). Therefore, in this work we assume that magnetic dipole moment is parallel to the earth magnetic field. Thus, we assume that the vehicles are isotropic, which might be a

rough but workable assumption.

Since magnetization is additive, the total magnetic dipole moment can be modeled as

$$\mathbf{m}_k = Q(\Psi_k)\mathbf{m}_0 + \frac{D}{\mu_0}\mathbf{B}_0. \quad (15)$$

In Figure 2 a graphical representation of the model is presented.

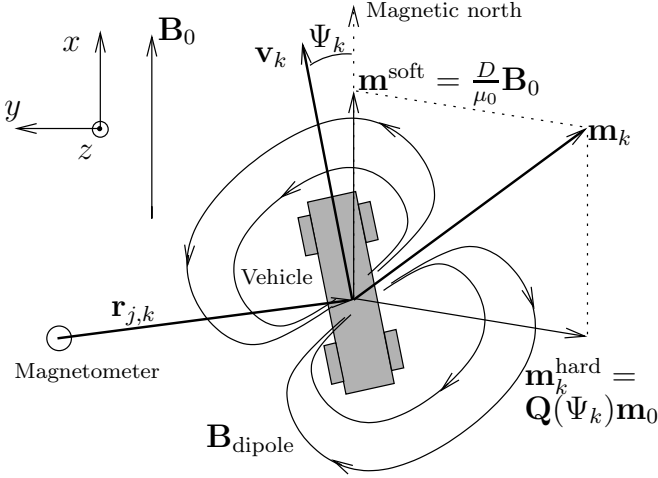


Figure 2: A stationary magnetometer measures the earth magnetic field \mathbf{B}_0 together with a magnetic dipole field $\mathbf{B}_{\text{dipole}}$. The magnetic dipole field is induced by a moving vehicle at position $\mathbf{r}_{j,k}$ with velocity \mathbf{v}_k and magnetic dipole moment $\mathbf{m}_k = Q(\Psi_k)\mathbf{m}_0 + \frac{D}{\mu_0}\mathbf{B}_0$. The heading angle Ψ_k is defined by the velocity direction.

We have now decomposed the magnetic dipole moment into two components, one representing the hard iron and one representing the soft iron. The corresponding model parameters D and \mathbf{m}_0 will represent the real magnetic signature of the target and will thus be constant even in a target maneuvering scenario.

2.6 General Sensor Model

The orientation dependent model can now be combined with the extended target model (10) which gives

$$\mathbf{h}_j^d(\mathbf{x}_k) = \mathbf{B}_{0,j} + \sum_{i=1}^d \mathbf{J}^{\mathbf{m}}(\mathbf{r}_k + \Delta\mathbf{r}_k^i - \boldsymbol{\theta}_j)\mathbf{m}_k^i \quad (16a)$$

with

$$\mathbf{m}_k^i = Q(\Psi_k)\mathbf{m}_0^i + \frac{D^i}{\mu_0}\mathbf{B}_0, \quad (16b)$$

$$\mathbf{B}_0 = \frac{1}{J} \sum_{j=1}^J \mathbf{B}_{0,j}, \quad (16c)$$

$$\Psi_k = \arctan2(v_k^y, v_k^x), \quad (16d)$$

$$\Delta \mathbf{r}_k^i = \left(i - \frac{d+1}{2} \right) \frac{L}{d-1} \frac{\mathbf{v}_k}{\|\mathbf{v}_k\|}. \quad (16e)$$

Here, the mean of all sensor biases $\mathbf{B}_{0,j}$ is used as an expression for the earth magnetic field, which is needed for describing the orientation of the soft iron contribution (14). The total sensor model is then given by

$$\mathbf{y}_{j,k} = \mathbf{h}_j^d(\mathbf{x}_k) + \mathbf{e}_{j,k} \quad (16f)$$

$$\text{with } \mathbf{x}_k = \left[(\mathbf{B}_{0,1:J})^\top \quad \mathbf{r}_k^\top \quad \mathbf{v}_k^\top \quad (\mathbf{m}_0^{1:d})^\top \quad (D^{1:d})^\top \quad L \right]^\top$$

Note that if the heading Ψ_k is constant, the magnetic dipole moment \mathbf{m}_k^i will also be constant. In such a scenario, the parameters for the hard iron \mathbf{m}_0^i and the soft iron D^i are not identifiable. Therefore, in such a scenario a parametrization of the dipole moment directly is a more attractive solution, which will be used in the next section.

3 Constant Velocity Tracking Model

The models presented in the previous section are not constrained to any type of motion. However, in this work special interest will be given to the scenario when vehicles pass the sensor with constant velocity. This prior knowledge enables us to formulate a static sensor model.

3.1 Sensor Model for Constant Velocity

By assuming constant velocity \mathbf{v}_k

$$\begin{aligned} \mathbf{r}_{k+1} &= \mathbf{r}_k + T\mathbf{v}_k \\ \mathbf{v}_{k+1} &= \mathbf{v}_k, \end{aligned} \quad (17)$$

the heading Ψ_k will also be constant as well as the magnetic dipole moment \mathbf{m}_k according to (15). We could also consider another parametrization of the target motion. However, if that motion model implies a time-varying heading Ψ_k , the magnetic dipole moment will no longer be constant and the target orientation dependent dipole model (15) has to be considered.

We can now define a static sensor model

$$\begin{aligned} \mathbf{y}_k &= \mathbf{h}_k(\mathbf{x}) + \mathbf{e}_k \\ &= \mathbf{B}_0 + \frac{\mu_0}{4\pi} \frac{3(\mathbf{r}_k \cdot \mathbf{m})\mathbf{r}_k - \|\mathbf{r}_k\|^2 \mathbf{m}}{\|\mathbf{r}_k\|^5} + \mathbf{e}_k \end{aligned} \quad (18)$$

$$\text{where } \mathbf{r}_k = \mathbf{r}_0 + kT\mathbf{v}_0.$$

Here, the substitution

$$\begin{aligned} \mathbf{r}_k &= \mathbf{r}_0 + kT\mathbf{v}_0 \\ \mathbf{m}_k &= \mathbf{m} \end{aligned} \quad (19)$$

has been used in (2). Thus, now we have the parameter vector

$$\mathbf{x} = \left[\mathbf{B}_0^\top \quad \mathbf{r}_0^\top \quad \mathbf{v}_0^\top \quad \mathbf{m}^\top \right]^\top, \quad (20)$$

where \mathbf{r}_0 is the initial position of the target, \mathbf{v}_0 its constant velocity and \mathbf{m} its constant magnetic dipole moment. Thus, the model (18) has 12 parameters where 6 of them enter linearly in (18) (\mathbf{B}_0 and \mathbf{m}) whereas the other 6 (\mathbf{r}_0 and \mathbf{v}_0) enter non-linearly.

In a similar manner also the extended target model presented in (10) can be reformulated under the constant velocity assumption. Here, all magnetic dipole moments $\mathbf{m}^{1:d}$ will be constant. We have

$$\mathbf{h}_{j,k}^d(\mathbf{x}) = \mathbf{B}_{0,j} + \sum_{i=1}^d \mathbf{J}^{\mathbf{m}}(\mathbf{r}_k + \Delta \mathbf{r}_k^i - \boldsymbol{\theta}_j) \mathbf{m}^i \quad (21a)$$

with

$$\Delta \mathbf{r}_k^i = \left(i - \frac{d+1}{2} \right) \frac{L}{d-1} \frac{\mathbf{v}_0}{\|\mathbf{v}_0\|} \quad \text{and} \quad \mathbf{r}_k = \mathbf{r}_0 + kT\mathbf{v}_0 \quad (21b)$$

The total sensor model is then given by

$$\mathbf{y}_{j,k} = \mathbf{h}_{j,k}^d(\mathbf{x}) + \mathbf{e}_{j,k} \quad (21c)$$

$$\text{with } \mathbf{x} = \left[(\mathbf{B}_{0,1:j})^\top \quad \mathbf{r}_0^\top \quad \mathbf{v}_0^\top \quad (\mathbf{m}^{1:d})^\top \quad L \right]^\top. \quad (21d)$$

3.2 Anderson function expansion for constant velocity

The presented sensor model (18) describes the observed magnetometer signal if the target is moving with constant velocity. An equivalent model (Wynn, 1999; Kozick and Sadler, 2007a,b, 2008) for the same problem setup can be formulated by modeling the signal itself. Direct calculations (Wynn, 1999) starting from (18) reveals that each of the three dimensions in the sensor response \mathbf{y}_k can be expressed as a linear combination of three elementary functions. These functions are known as the Anderson functions (Wynn, 1999). By choosing the time origin at the *closest point of approach* (CPA) time t_{CPA} and normalizing it with the CPA range r_{CPA} and the speed $v_0 = \|\mathbf{v}_0\|$, the resulting model is

$$\mathbf{y}_k = \mathbf{B}_0 + \mathbf{C} \cdot \mathbf{f} \left(\frac{v_0}{r_{CPA}} (kT - t_{CPA}) \right) + \mathbf{e}_k, \quad (22)$$

where the time dependency enters in the orthogonal Anderson functions (Wynn, 1999)

$$\mathbf{f}(t) = [f_0(t) \quad f_1(t) \quad f_2(t)]^T \quad (23a)$$

$$f_n(t) = \frac{t^n}{(t^2 + 1)^{\frac{5}{2}}}, \quad n = 0, 1, 2 \quad (23b)$$

and where \mathbf{C} is a 3×3 -matrix of coefficients. Consequently, (22) is linear in \mathbf{B}_0 and \mathbf{C} , which includes $3 + 9 = 12$ parameters, and is nonlinear in the remaining 3 parameter v_0 , r_{CPA} and t_{CPA} , in total 15 parameters.

Both t_{CPA} and r_{CPA} are related to the parameters in (20) in the following way: The traveled distance between $t = 0$ and $t = t_{CPA}$ is equal to the projection of $-\mathbf{r}_0$ onto \mathbf{v}_0 , see Figure 3.

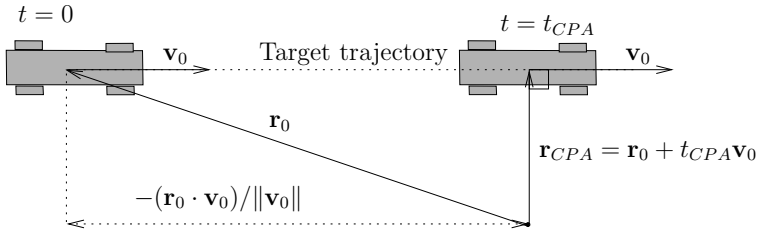


Figure 3: The CPA time t_{CPA} and CPA range r_{CPA} can be expressed by the initial position \mathbf{r}_0 and the velocity \mathbf{v}_0 .

This gives the CPA time and CPA range

$$t_{CPA} = -\frac{(\mathbf{r}_0 \cdot \mathbf{v}_0)}{\|\mathbf{v}_0\|} \frac{1}{\|\mathbf{v}_0\|} = -\frac{(\mathbf{r}_0 \cdot \mathbf{v}_0)}{(\mathbf{v}_0 \cdot \mathbf{v}_0)} \quad (24a)$$

$$r_{CPA} = \|\mathbf{r}_{CPA}\| = \|\mathbf{r}_0 + t_{CPA} \cdot \mathbf{v}_0\|. \quad (24b)$$

Furthermore, also the coefficients in \mathbf{C} are related to (20) in that

$$\mathbf{C} = \beta \begin{bmatrix} \mathbf{c}_1 & \mathbf{c}_2 & \mathbf{c}_3 \end{bmatrix} \quad (25a)$$

with

$$\mathbf{c}_1 = 3(\tilde{\mathbf{r}} \cdot \tilde{\mathbf{m}})\tilde{\mathbf{r}} - \tilde{\mathbf{m}} \quad (25b)$$

$$\mathbf{c}_2 = 3(\tilde{\mathbf{r}} \cdot \tilde{\mathbf{m}})\tilde{\mathbf{v}} - 3(\tilde{\mathbf{v}} \cdot \tilde{\mathbf{m}})\tilde{\mathbf{r}} \quad (25c)$$

$$\mathbf{c}_3 = 3(\tilde{\mathbf{m}} \cdot \tilde{\mathbf{v}})\tilde{\mathbf{v}} - \tilde{\mathbf{m}} \quad (25d)$$

where the following normalization has been used

$$\beta = \frac{\mu_0}{4\pi} \frac{m}{r_{\text{CPA}}^3}, \quad \tilde{\mathbf{r}} = \frac{\mathbf{r}_{\text{CPA}}}{r_{\text{CPA}}}, \quad \tilde{\mathbf{v}} = \frac{\mathbf{v}_0}{v_0}, \quad \tilde{\mathbf{m}} = \frac{\mathbf{m}}{m}. \quad (26)$$

3.3 Comparison

By comparing the two different models (18) and (22), the following observations can be made

- The Anderson function model (22) consists of 15 parameters, whereas the dipole model (18) consists of only 12. Consequently, (22) is overparametrized. The reason is that the superposition of the Anderson functions in (22) is non-linearly constrained and does not have all 9 degrees of freedom as given in (22). This can be seen by inspecting (25). Each of the unit vectors $\tilde{\mathbf{r}}$, $\tilde{\mathbf{v}}$ and $\tilde{\mathbf{m}}$ contribute with 2 degrees of freedom to the matrix C. By taking the coefficient β and the constraint $(\tilde{\mathbf{r}} \cdot \tilde{\mathbf{v}}) = 0$ into account, C has in total only 6 independent components, or equivalently, the 9 coefficients in C have to obey 3 (non-linear) constraints. These constraints are not present in (22). Thus, (22) is a relaxation of (18).
- The dipole model (18) has 6 parameters entering non-linearly in the model, whereas (22) has only 3. Since the relaxation reduces the non-linearity, (22) can be seen as a convexification of the more non-linear model (18).
- The parametrization of (18) is directly related to the target trajectory (\mathbf{r}_0 and \mathbf{v}_0) and the magnetic signature of the target \mathbf{m} . This will make the multi sensor extension of (18) trivial, see Section 2.2. In contrast, a multi sensor version of (22) has to rely on sub-optimal solutions where each sensor estimates its own matrix C, which then are fused at a later stage, as done by Kozick and Sadler (2008).

In addition, (18) can easily be extended to tracking by applying a motion model and a nonlinear filter, which has been done by Wahlström et al. (2011). This extension would for (22) be harder, since the shape of the Anderson functions relies on a linear motion of the target.

4 Magnetometer Potential for Localization and Tracking

In this section limitations and possibilities of the magnetometer will be discussed in terms of observability and the Cramér Rao lower bound as a function of the placement of a second sensor.

Without loss of generality the bias \mathbf{B}_0 is assumed to be known and the discussion will be based on the unbiased static sensor model in (18) with the state $\mathbf{x} = [\mathbf{r}_0^T \quad \mathbf{v}_0^T \quad \mathbf{m}^T]^T$ to make the analysis cleaner. We will therefore consider the

model

$$\mathbf{h}_k(\mathbf{x}) = \mathbf{h}(\mathbf{r}_k, \mathbf{m}) = \frac{\mu_0}{4\pi} \frac{3(\mathbf{r}_k \cdot \mathbf{m})\mathbf{r}_k - \|\mathbf{r}_k\|^2 \mathbf{m}}{\|\mathbf{r}_k\|^5} \quad (27)$$

where $\mathbf{r}_k = \mathbf{r}_0 + kT\mathbf{v}_0$.

4.1 Single Sensor Observability

To analyze observability, a local analysis can be performed. Consider the *Fischer information matrix* (FIM), which under Gaussian assumptions of the sensor noise $\mathbf{e}_k \sim \mathcal{N}(\mathbf{0}, \mathbf{R})$ reads

$$\mathcal{I}(\mathbf{x}^0) \triangleq \sum_{k=1}^N \nabla \mathbf{h}_k^\top(\mathbf{x}^0) \mathbf{R}^{-1} \nabla \mathbf{h}_k(\mathbf{x}^0), \quad (28)$$

where \mathbf{x}^0 are the true parameters. Any zero eigenvalues of this matrix makes it singular, which indicates a lack of local observability at \mathbf{x}^0 . The unobservable subspace is spanned by the eigenvectors corresponding to the zero eigenvalues, also known as the kernel of the matrix. Indeed, it can be shown that the kernel of $\mathcal{I}(\mathbf{x}^0)$ is at least of dimension one.

1 Proposition. Consider the sensor model (27) and its information matrix (28). Then

$$\mathcal{I}(\mathbf{x}^0) \cdot \begin{bmatrix} \mathbf{r}_0 \\ \mathbf{v}_0 \\ 3\mathbf{m} \end{bmatrix} = \mathbf{0} \quad \text{for all } \mathbf{x}^0 = \begin{bmatrix} \mathbf{r}_0 \\ \mathbf{v}_0 \\ \mathbf{m} \end{bmatrix} \in \mathbb{R}^9. \quad (29)$$

Proof: Define $\bar{\mathbf{x}} = \begin{bmatrix} \mathbf{r}_0^\top & \mathbf{v}_0^\top & 3\mathbf{m}^\top \end{bmatrix}^\top$ and apply $\bar{\mathbf{x}}$ to the Jacobian

$$\begin{aligned} \nabla \mathbf{h}_k(\mathbf{x}^0) \bar{\mathbf{x}} &= \begin{bmatrix} \mathbf{J}^r(\mathbf{r}_k, \mathbf{m}) & kT\mathbf{J}^r(\mathbf{r}_k, \mathbf{m}) & \mathbf{J}^m(\mathbf{r}_k) \end{bmatrix} \cdot \begin{bmatrix} \mathbf{r}_0 \\ \mathbf{v}_0 \\ 3\mathbf{m} \end{bmatrix} \\ &= \mathbf{J}^r(\mathbf{r}_k, \mathbf{m})\mathbf{r}_0 + kT\mathbf{J}^r(\mathbf{r}_k, \mathbf{m})\mathbf{v}_0 + 3\mathbf{J}^m(\mathbf{r}_k)\mathbf{m} \\ &= \mathbf{J}^r(\mathbf{r}_k, \mathbf{m})\mathbf{r}_k + 3\mathbf{J}^m(\mathbf{r}_k)\mathbf{m}. \end{aligned}$$

where $\mathbf{J}^m(\mathbf{r}_k)$ and $\mathbf{J}^r(\mathbf{r}_k, \mathbf{m})$ are the Jacobians of $\mathbf{h}_k(\mathbf{x}) = \mathbf{h}(\mathbf{r}_k, \mathbf{m})$ with respect to \mathbf{m} and \mathbf{r}_k and respectively

$$\mathbf{J}^m(\mathbf{r}_k) = \nabla_{\mathbf{m}} \mathbf{h}(\mathbf{r}_k, \mathbf{m}) = \frac{1}{\|\mathbf{r}_k\|^5} (3\mathbf{r}_k \mathbf{r}_k^\top - \|\mathbf{r}_k\|^2 \mathbf{I}_3) \quad (30a)$$

$$\mathbf{J}^r(\mathbf{r}_k, \mathbf{m}) = \nabla_{\mathbf{r}_k} \mathbf{h}(\mathbf{r}_k, \mathbf{m}) = \frac{3}{\|\mathbf{r}_k\|^5} \left((\mathbf{r}_k \cdot \mathbf{m}) \mathbf{I}_3 + \mathbf{r}_k \mathbf{m}^\top + \mathbf{m} \mathbf{r}_k^\top - 5 \frac{(\mathbf{r}_k \cdot \mathbf{m})}{(\mathbf{r}_k \cdot \mathbf{r}_k)} \mathbf{r}_k \mathbf{r}_k^\top \right). \quad (30b)$$

Further, we can show that

$$\mathbf{J}^r(\mathbf{r}_k, \mathbf{m})\mathbf{r}_k = -3\mathbf{J}^m(\mathbf{r}_k)\mathbf{m} \quad (31)$$

and from this we get

$$\nabla \mathbf{h}_k(\mathbf{x}^0) \bar{\mathbf{x}} = -3\mathbf{J}^{\mathbf{m}}(\mathbf{r}_k) \mathbf{m} + 3\mathbf{J}^{\mathbf{m}}(\mathbf{r}_k) \mathbf{m} = \mathbf{0} \quad \forall k,$$

which leads to

$$\mathcal{I}(\mathbf{x}^0) \bar{\mathbf{x}} = \sum_{k=1}^N \nabla \mathbf{h}_k^{\top}(\mathbf{x}^0) \mathbf{R}^{-1} \underbrace{\nabla \mathbf{h}_k(\mathbf{x}^0) \bar{\mathbf{x}}}_{=0} = \mathbf{0}.$$

□

Thus, the kernel is at least given by the following one-dimensional subspace:

$$\text{Ker}(\mathcal{I}(\mathbf{x}^0)) \supseteq \left(\lambda \begin{bmatrix} \mathbf{r}_0^{\top} & \mathbf{v}_0^{\top} & 3\mathbf{m}^{\top} \end{bmatrix}^{\top} \mid \lambda \in \mathbb{R} \right). \quad (32)$$

In most cases the kernel dimension is exactly equal to one, meaning that (32) is fulfilled with equality. For example, for the following parameters $\mathbf{r}_0 = [-3 \ 1 \ 0]^{\top}$, $\mathbf{v}_0 = [1 \ 0 \ 0]^{\top}$ and $\mathbf{m} = [1 \ 1 \ 1]^{\top}$, the kernel of the information matrix indeed has dimension one. However, if \mathbf{m} is orthogonal to both \mathbf{r}_0 and \mathbf{v}_0 the kernel will be larger. For example, for the parameter $\mathbf{r}_0 = [-3 \ 1 \ 0]^{\top}$, $\mathbf{v}_0 = [1 \ 0 \ 0]^{\top}$ and $\mathbf{m} = [0 \ 0 \ 1]^{\top}$ the kernel of the information matrix has dimension two.

Due to the non-linearity, the expression of the unobservable subspace (32) is only valid at the point \mathbf{x}^0 and can therefore only be regarded as the tangent of the unobservable one-dimensional manifold at this point. Denote this manifold $\bar{\mathbf{x}}(u) = [\tilde{\mathbf{r}}_0(u) \ \tilde{\mathbf{v}}_0(u) \ 3\tilde{\mathbf{m}}(u)]^{\top}$, where u is a scalar parameter. For each u there will be a $\lambda(u)$ such that

$$\frac{d}{du} \bar{\mathbf{x}}(u) = \frac{d}{du} \begin{bmatrix} \tilde{\mathbf{r}}_0(u) \\ \tilde{\mathbf{v}}_0(u) \\ 3\tilde{\mathbf{m}}(u) \end{bmatrix} = \lambda(u) \begin{bmatrix} \tilde{\mathbf{r}}_0(u) \\ \tilde{\mathbf{v}}_0(u) \\ 3\tilde{\mathbf{m}}(u) \end{bmatrix}. \quad (33)$$

By choosing the parametrization $u = \lambda(u)^{-1}$, we get the following unobservable manifold

$$\bar{\mathbf{x}}(u) = \begin{bmatrix} u\mathbf{r}_0 \\ u\mathbf{v}_0 \\ u^3\mathbf{m} \end{bmatrix}. \quad (34)$$

It is instructive to substitute $\bar{\mathbf{x}}(u)$ into (18) and conclude that $\mathbf{h}_{1:k}(\bar{\mathbf{x}}(u))$ is independent of the parameter u , which means that all points on this manifold will give the same output \mathbf{y}_k . For example, multiplying \mathbf{r}_0 and \mathbf{v}_0 with 2, and \mathbf{m} with $2^3 = 8$ will result in the same output \mathbf{y}_k .

The result is physically quite intuitive since the magnetometer does not measure any absolute distances and the system can be arbitrarily scaled without changing the measured output. Thus, a small vehicle driving slowly close to the sensor will give rise to the same signal as a large vehicle driving fast far from the sensor.

Furthermore, the cubic scaling of the magnetic dipole moment \mathbf{m} is reasonable since it is related to the volume of the vehicle.

The conducted observability analysis also gives insight to the comparison between the dipole model (18) and the Anderson function model (22):

- The sensor model (22) can easily be re-parametrized excluding the unobservable manifold (34) by introducing the scale parameter $\alpha = v_0/r_{\text{CPA}}$. This parametrization has also been used by Wynn (1999); Kozick and Sadler (2007a,b, 2008). An equivalent re-parametrization in (18) would inevitably increase the model complexity.
- By substituting (34) into (24a) it can be stated that t_{CPA} is independent of u and consequently observable. This means that t_{CPA} can be uniquely determined from only one vector magnetometer and does not necessarily need to be aided with other sensors as done by Kozick and Sadler (2007a,b, 2008) to achieve observability for that parameter. Furthermore, notice that only one axis of the vector magnetometer is sufficient to achieve observability for t_{CPA} . This can be seen by decomposing its signal into the three Anderson functions (23b), which each of them contains the information of t_{CPA} .

4.2 Single Sensor Observability with Prior Information

The lack of observability can be solved by using prior knowledge about the target trajectory. This situation has been studied by Kozick and Sadler (2007a) and Kozick and Sadler (2007b), which includes the possibility to use information about the range at CPA, for example by knowing the geometry of the road on which the vehicle is traveling. By using (24) this gives the extra scalar measurement

$$y_{\text{CPA}} = h_{\text{CPA}}(\mathbf{x}^0) = \|\mathbf{r}_{\text{CPA}}\| = \left\| \mathbf{r}_0 - \frac{(\mathbf{r}_0 \cdot \mathbf{v}_0)}{(\mathbf{v}_0 \cdot \mathbf{v}_0)} \cdot \mathbf{v}_0 \right\| \quad (35)$$

and the corresponding information matrix can be computed as

$$\mathcal{I}_{\text{CPA}}(\mathbf{x}^0) = \nabla h_{\text{CPA}}^{\text{T}}(\mathbf{x}^0) \alpha^{-1} \nabla h_{\text{CPA}}(\mathbf{x}^0), \quad (36)$$

where $\alpha \rightarrow 0$ since the information in (24b) comes with zero uncertainty. Furthermore, since this prior knowledge is independent of the sensor information, the information matrices are additive, which gives

$$\mathcal{I}_{+\text{CPA}}(\mathbf{x}^0) = \mathcal{I}(\mathbf{x}^0) + \mathcal{I}_{\text{CPA}}(\mathbf{x}^0). \quad (37)$$

If the condition in (32) is fulfilled with equality, we only need to require that $\mathcal{I}_{\text{CPA}}(\mathbf{x}^0) \cdot \begin{bmatrix} \mathbf{r}_0^{\text{T}} & \mathbf{v}_0^{\text{T}} & 3\mathbf{m}^{\text{T}} \end{bmatrix}^{\text{T}} \neq \mathbf{0}$ for $\mathcal{I}_{+\text{CPA}}(\mathbf{x}^0)$ to have full rang. This is indeed true if \mathbf{r}_0 is not parallel to \mathbf{v}_0 .

2 Proposition. Consider the sensor model (35) and its information matrix (36).

Then

$$\mathcal{I}_{CPA}(\mathbf{x}^0) \cdot \begin{bmatrix} \mathbf{r}_0 \\ \mathbf{v}_0 \\ 3\mathbf{m} \end{bmatrix} = \mathbf{0} \quad (38)$$

if and only if \mathbf{r}_0 is parallel to \mathbf{v}_0 .

Proof: Define $\bar{\mathbf{x}} = [\mathbf{r}_0^\top \quad \mathbf{v}_0^\top \quad 3\mathbf{m}^\top]^\top$ and apply $\bar{\mathbf{x}}$ to the Jacobian

$$\nabla \mathbf{h}_k(\mathbf{x}^0) \bar{\mathbf{x}} = \begin{bmatrix} \frac{\mathbf{r}_{CPA}^\top}{\|\mathbf{r}_{CPA}\|} & \frac{(\mathbf{r}_0 \cdot \mathbf{v}_0) \mathbf{r}_{CPA}^\top}{(\mathbf{v}_0 \cdot \mathbf{v}_0) \|\mathbf{r}_{CPA}\|} & \mathbf{0}_{1 \times 3} \end{bmatrix} \cdot \begin{bmatrix} \mathbf{r}_0 \\ \mathbf{v}_0 \\ 3\mathbf{m} \end{bmatrix}$$

Since $(\mathbf{r}_{CPA} \cdot \mathbf{v}_0) = 0$ we have

$$\begin{aligned} \nabla \mathbf{h}_k(\mathbf{x}^0) \bar{\mathbf{x}} &= \frac{(\mathbf{r}_{CPA} \cdot \mathbf{r}_0)}{\|\mathbf{r}_{CPA}\|} \\ &= \frac{(\mathbf{r}_0 \cdot \mathbf{r}_0)(\mathbf{v}_0 \cdot \mathbf{v}_0) - (\mathbf{r}_0 \cdot \mathbf{v}_0)(\mathbf{r}_0 \cdot \mathbf{v}_0)}{(\mathbf{v}_0 \cdot \mathbf{v}_0) \|\mathbf{r}_{CPA}\|} \geq 0 \end{aligned}$$

and is only fulfilled with equality if and only if \mathbf{r}_0 is parallel to \mathbf{v}_0 . This leads to

$$\mathcal{I}_{CPA}(\mathbf{x}^0) \bar{\mathbf{x}} = \sum_{k=1}^N \nabla \mathbf{h}_k^\top(\mathbf{x}^0) \mathbf{R}^{-1} \nabla \mathbf{h}_k(\mathbf{x}^0) \bar{\mathbf{x}} = \mathbf{0}$$

if and only if \mathbf{r}_0 is parallel to \mathbf{v}_0 . \square

Consequently, we do not achieve observability if \mathbf{r}_0 is parallel to \mathbf{v}_0 , which corresponds to $\mathbf{r}_{CPA} = \mathbf{0}$. However, this situation can be considered as unphysical, since it would correspond to a scenario where the sensor is on the target trajectory.

4.3 Multi Sensor Observability

The lack of observability can also be solved with a second sensor. To handle multiple sensors, the sensor model has to be slightly expanded. Let the j th sensor be positioned at $\boldsymbol{\theta}_j$. The target parameter relative to the j th sensor will then be $\mathbf{x}_j = [(\mathbf{r}_0 - \boldsymbol{\theta}_j)^\top \quad \mathbf{v}_0^\top \quad \mathbf{m}^\top]^\top$ and the total sensor model is given by

$$\mathbf{y}_{k,j} = \mathbf{h}_k(\mathbf{x}_j) + \mathbf{e}_{k,j} \quad \text{for all } j \in J. \quad (39)$$

Furthermore, under the assumption that the measurement noise of different sensors are independent, the information matrices for all sensors are additive, which gives

$$\mathcal{I}_J(\mathbf{x}^0, \boldsymbol{\theta}_{1:J}) = \sum_{j=1}^J \mathcal{I}(\mathbf{x}_j^0) \quad (40)$$

By again using Proposition 1 we have

$$\text{Ker}(\mathcal{I}(\mathbf{x}_j^0)) \supseteq \left(\lambda \left[(\mathbf{r}_0 - \boldsymbol{\theta}_j)^\top \mathbf{v}_0^\top \mathbf{3m}^\top \right]^\top \mid \lambda \in \mathbb{R} \right). \quad (41)$$

Assume that (41) is fulfilled with equality for two different sensors at $\boldsymbol{\theta}_1$ and $\boldsymbol{\theta}_2$. Then the intersection of their kernels will be empty if $\boldsymbol{\theta}_1 \neq \boldsymbol{\theta}_2$. Under these assumptions we will then reach observability for a system with two sensors.

4.4 Comparison

We can now compare two extensions from the single sensor setup

- Setup 1) One sensor with prior knowledge of CPA range
- Setup 2) Two sensors

Both scenarios resolve the observability issue reported for the single sensor setup except for some cases with special geometry. However, Setup 2 requires that both coordinate systems of the two sensors are aligned with each other and also that their relative position is known in order not to violate the sensor model (39). This issue is less critical in Setup 1 since any misalignment of the single sensor will not change the range to the target and will thus not violate the sensor model. Furthermore, in Setup 2 the two sensors need to be synchronized.

4.5 Cramér Rao Lower Bound

So far we have only compared the models concerning their observability properties. However, in order to find a good sensor deployment we want to quantify the best achievable estimation performance as a function of the sensor positions. This analysis is justified with the CRLB (Kay, 1993), which states that any unbiased estimate must have a covariance matrix larger than or equal to the inverse of the FIM

$$\text{Cov}(\hat{\mathbf{x}}) - \mathcal{I}(\mathbf{x}^0)^{-1} \geq 0. \quad (42)$$

The design goal in the sensor deployment is then to make the inverse of the information matrix as small as possible in order to minimize the covariance of the estimate. We do this analysis for the partitions of the state space corresponding to \mathbf{r}_0 , \mathbf{v}_0 and \mathbf{m} separately. We notice that for a positive semidefinite matrix any diagonal sub matrix is also positive semidefinite. By following Kay (1993) and using that property on (42) we get

$$[\text{Cov}(\hat{\mathbf{x}}) - \mathcal{I}(\mathbf{x}^0)^{-1}]_{ii} \geq 0 \quad (43)$$

and consequently

$$\text{Cov}(\hat{\mathbf{x}}_i) = [\text{Cov}(\hat{\mathbf{x}})]_{ii} \geq [\mathcal{I}(\mathbf{x}^0)^{-1}]_{ii} \quad (44)$$

where i corresponds to a partition of the state vector. The design goal in the sensor deployment is then to minimize any of the three criteria

$$\|[\mathcal{I}(\mathbf{x}^0)^{-1}]_{\mathbf{r}_0\mathbf{r}_0}\|_2, \quad \|[\mathcal{I}(\mathbf{x}^0)^{-1}]_{\mathbf{v}_0\mathbf{v}_0}\|_2, \quad \|[\mathcal{I}(\mathbf{x}^0)^{-1}]_{\mathbf{m}\mathbf{m}}\|_2 \quad (45)$$

depending on if we are interested in a good estimation performance for the position \mathbf{r}_0 , velocity \mathbf{v}_0 or magnetic dipole moment \mathbf{m} . In order to examine where a second magnetometer should be placed, these three criteria can be computed for different positions θ_2 of the second sensor. Wahlström et al. (2010) has analyzed similar criteria. For most values \mathbf{x}^0 the conclusion is that you should deploy a two sensor system symmetrically at both sides of the target trajectory if a good estimation performance for the position \mathbf{r}_0 and magnetic dipole moment \mathbf{m} is of interest. On the other hand, for the velocity \mathbf{v}_0 it is better to place both sensors at the same side of the target trajectory and as separate as possible, which is intuitive. In the setup for the real world data collection presented in this work, the first of these two deployments has been considered.

5 Estimation

As already mentioned, in this work special interest will be given to scenarios where vehicles pass the sensors with constant velocity. Therefore, in this section the estimation methods to be used with the constant velocity models presented in Section 3 will be given. These methods will later be used in the sensor model validation presented in Section 6.

5.1 Sensor Noise Covariance

First, the distribution of the sensor noise $\mathbf{e}_{j,k}$ will be estimated for each of the magnetometers. According to Törnqvist (2006), the noise of the magnetometer (Xse, 2005) is white Gaussian, i.e. its samples are i.i.d. and normally distributed with zero mean. Such a stochastic process is uniquely defined by its covariance matrix \mathbf{R} . This matrix can be estimated from a measurement sequence without any moving targets by using the sample covariance

$$\mathbf{R}_j = \frac{1}{N-1} \sum_{k=1}^N (\mathbf{y}_{j,k} - \bar{\mathbf{y}}_j)(\mathbf{y}_{j,k} - \bar{\mathbf{y}}_j)^\top, \quad \text{where}$$

$$\bar{\mathbf{y}}_j = \frac{1}{N} \sum_{k=1}^N \mathbf{y}_{j,k}.$$

Here \mathbf{R}_j represents the covariance of the j th sensor.

5.2 Parameter Estimation using Constant Velocity Model

The parameter \mathbf{x} introduced in the models (3) and (16) can be estimated using weighted nonlinear least squares by minimizing the cost function

$$\hat{\mathbf{x}} = \arg \min_{\mathbf{x}} V^d(\mathbf{x}) \quad (46a)$$

$$V^d(\mathbf{x}) = \sum_{k=1}^N \sum_{j=1}^J (\mathbf{y}_{j,k} - \mathbf{h}_{j,k}^d(\mathbf{x}))^\top \mathbf{R}_j^{-1} (\mathbf{y}_{j,k} - \mathbf{h}_{j,k}^d(\mathbf{x})). \quad (46b)$$

Note that under the Gaussian assumption of the measurement noise $\mathbf{e}_{j,k}$, (46) will be both a *minimum variance* and a *maximum likelihood* estimate.

In this framework, also the covariance of the optimum $\hat{\mathbf{x}}$ can be estimated. Since $\nabla V = \mathbf{0}$ at optimum, the covariance can be approximated as (Gustafsson, 2010)

$$\text{Cov}(\hat{\mathbf{x}}) \approx \left(\sum_{k=1}^N \sum_{j=1}^2 \nabla \mathbf{h}_{j,k}^d(\hat{\mathbf{x}})^\top \mathbf{R}_j^{-1} \nabla \mathbf{h}_{j,k}^d(\hat{\mathbf{x}}) \right)^{-1}. \quad (47)$$

5.3 Model Validation

The number of dipoles d can for this model class be considered as a model order parameter, which will affect the statistical properties of the cost function. Under the assumption that both the measurement equation $\mathbf{h}_{j,k}(\mathbf{x})$ and the noise $\mathbf{e}_{j,k} \sim \mathcal{N}(\mathbf{0}, \mathbf{R}_j)$ are correctly modeled, the cost function $V^d(\hat{\mathbf{x}})$ will be $\chi_{Nn_y - n_x}^2$ distributed, n_y and n_x being the dimension of each measurement and the state space respectively. For the extended target model in (16) this will be

$$n_y = \dim(\mathbf{y}_{1:J,k}) = 3J \quad (48)$$

$$\begin{aligned} n_x &= \dim\left(\left[(\mathbf{B}_{0,1:J})^\top \quad \mathbf{r}_0^\top \quad \mathbf{v}_0^\top \quad (\mathbf{m}^{1:d})^\top \quad L \right]^\top \right) \\ &= 3J + 3 + 3 + 3d + 1 = 3J + 7 + 3d. \end{aligned} \quad (49) \quad (50)$$

Since the mean of $\chi_{Nn_y - n_x}^2$ is equal to $Nn_y - n_x$, the normalized cost function

$$\bar{V}^d(\hat{\mathbf{x}}) = V^d(\hat{\mathbf{x}}) / (Nn_y - n_x) \quad (51a)$$

$$= V^d(\hat{\mathbf{x}}) / (3NJ - 3J - 7 - 3d) \quad (51b)$$

is considered and $\bar{V}^d(\hat{\mathbf{x}}) \approx 1$ would indicate a correct model. Therefore, the normalized cost function can be used for choosing an appropriate model order. However, in this work no explicit model order selection rule will be proposed.

5.4 State and Parameter Estimation

By using the maneuvering target model presented in Section 2.5, the constant velocity assumption can be relaxed. By combining that sensor model with an appropriate motion model, a non-linear filter can be applied to estimate all states included in the model. Related results have been reported by Wahlström et al. (2011) where a (nearly) constant velocity model has been applied and the estimation has been performed with an extended Kalman filter using data for vehicles passing a three-way intersection.

6 Sensor Model Validation

In order to validate the proposed sensor models, real experimental data has been collected with magnetometers (Xse, 2005). In this section, the experimental setup will be described and the results of the validation will be given using the estimation methodology presented in Section 5. In accordance with the results in Section 4.1 and 4.3, all measurements have been done with two sensors in order to reach observability.

6.1 Experimental Setup

The two magnetometers have been placed close to a straight road (see Figure 4). In accordance with the discussion in Section 4.5 they have been deployed symmetrically at each side of the road. In the experimental setup a relative distance of 9.0 m between the sensors has been used. As reference data a video camera

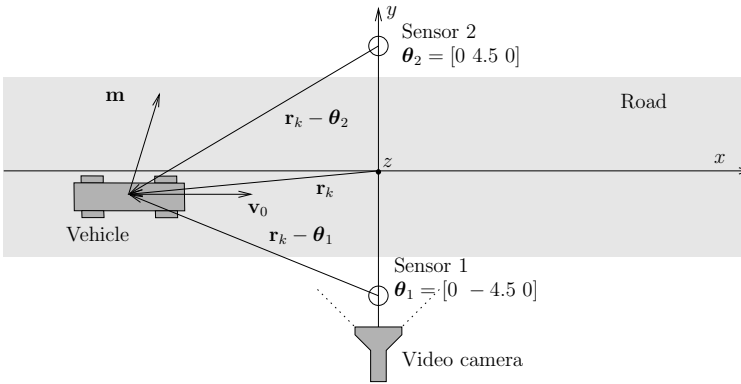


Figure 4: Sensor setup for the sensor model validation. \mathbf{r}_k is a vector from the origin to the vehicle, \mathbf{v}_0 is the velocity of the vehicle, \mathbf{m} is the magnetic moment of the vehicle and θ_1 and θ_2 are the positions of the two sensors.

has been used recording all objects within the sensor range area. Data from six vehicles (Figure 5) passing the sensors are used for the sensor model validation in Section 6.3 and 6.4.

6.2 Sensor Noise Covariance

Without any targets, each magnetometer measures a stationary magnetic field together with sensor noise. This stationary magnetic field mainly consist of the earth magnetic field but also of induced magnetic fields from other stationary ferromagnetic objects in the environment. We do not need to assume that the magnetic field in the environment is homogeneous, however we do assume it to be stationary.

By using data from a time window without any moving targets present, the sensor noise covariance can be estimated using the approach described in Section 5.1. In

this manner, the two symmetric 3×3 -matrices R_1 and R_2 for the two sensors in use are estimated to be

$$R_1 = 10^{-15} \begin{bmatrix} 0.1303 & -0.0073 & -0.0114 \\ -0.0073 & 0.1112 & 0.0117 \\ -0.0114 & 0.0117 & 0.1558 \end{bmatrix}, \quad (52a)$$

$$R_2 = 10^{-15} \begin{bmatrix} 0.1500 & 0.0205 & 0.0215 \\ 0.0205 & 0.1937 & 0.0310 \\ 0.0215 & 0.0310 & 0.1483 \end{bmatrix}, \quad (52b)$$

where the unit of the measurement is Tesla.

6.3 Point Target Model Validation

Since the road is straight, the constant velocity assumption for all vehicles applies. We start with modeling the vehicles as a single dipole. Since we have a scenario with multiple sensors, the sensor model presented in 2.2 will be considered.

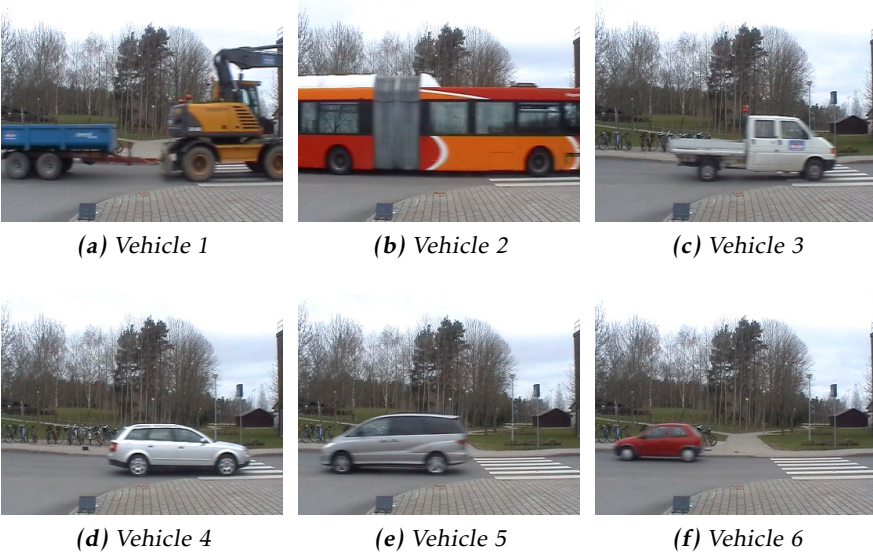


Figure 5: The vehicles used in the sensor model validation.

In Table 1 the normalized cost function for the vehicles in Figure 5 is presented. By this we can conclude that larger vehicles generally produce a worse fit with the measured data than smaller vehicles do. This is intuitively clear since the point target model assumes that the target has no geometrical extension, which is a more rough approximation for large vehicles than for small vehicles. However, for all vehicles, the normalized cost function is much larger than 1.

Table 1: The values of the normalized cost function $V(\hat{\mathbf{x}})/(Nn_y - n_x)$ for the point target model. N is number of samples, n_y the dimension of each measurement and n_x the state dimension.

Vehicle	$V(\hat{\mathbf{x}})/(Nn_y - n_x)$	N	n_y	n_x
1	360	70	6	15
2	142	54	6	15
3	10	32	6	15
4	14	44	6	15
5	51	27	6	15
6	17	22	6	15

Finally, by simulating the model with the estimated parameter $\hat{\mathbf{x}}$ we get an estimate of the measured quantity $\hat{\mathbf{y}}_{j,k} = \mathbf{h}_{j,k}(\hat{\mathbf{x}})$, which can be compared with the measured magnetic field $\mathbf{y}_{j,k}$. Note that the residual $\|\mathbf{y}_{j,k} - \hat{\mathbf{y}}_{j,k}\|_{R_j}$ is exactly what is being minimized in the weighted nonlinear least squares framework. In Figure 6a the estimated x-component of the magnetic field for sensor 1, $\hat{y}_{j=1,k}^x$, is compared with its measured equivalence $y_{j=1,k}^x$. We can see that the main character of the signal has been caught. However, there is potential to get a better fit.

6.4 Extended Target Model Validation

In order to improve the model fit, the extended target model (16) with $d > 1$ will be considered.

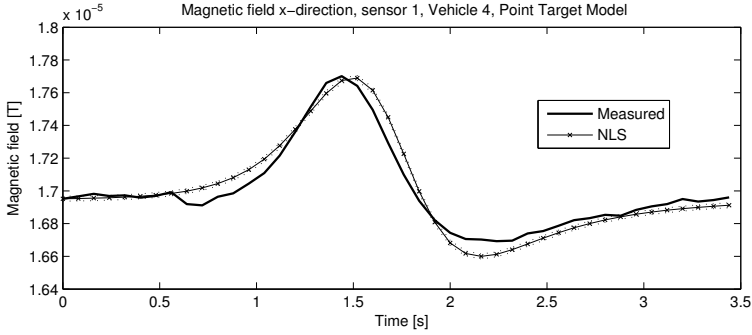
Model Order Selection and Model Validation

For an extended target model, an arbitrary model order can be chosen which here is the number of dipoles d . In Figure 7, the normalized cost function (51) is displayed as a function of the model order d .

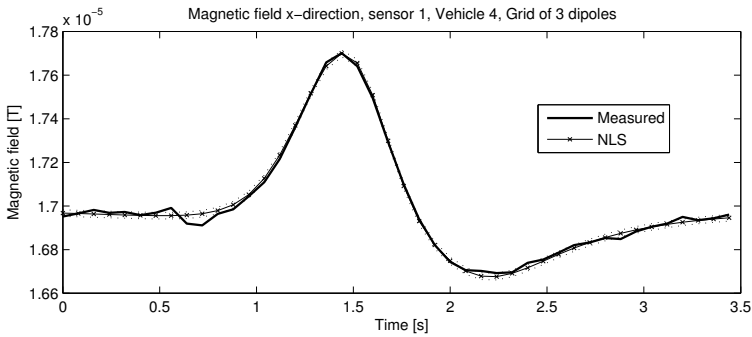
For most vehicles, the normalized cost function rapidly decreases with higher model order d . For the smaller vehicles it can be seen that the normalized cost function converges towards 1, which corresponds to a correct model.

With the model order $d = 3$, the equivalent plot to Figure 6a can be found in Figure 6b. From this it can be concluded that an almost perfect fit has been achieved. This model order will be used for a more thorough analysis and all results are presented in Tables 2, 3, 4 and 5 for each vehicle.

In Table 2 the normalized cost function for the vehicles is given. We have seen that this quantity should equal one for correct models. By comparing Table 2 with Table 1, we see that the small vehicles 3–6 have taken huge steps in this direction, whereas the large vehicles 1–2 still have a long way to go. This illustrates the real difficulties finding feasible models for large vehicles using models with a reasonable state space dimension.



(a) The point target model with one dipole



(b) The extended target model with a row of three dipoles

Figure 6: The measured magnetic field $y_{j=1,k}^x$ in the x -direction together with the NLS-estimated value $h_{j=1,k}^x(\hat{\mathbf{x}})$ for vehicle 4 with a 90 % confidence interval.

Length Estimation

Extended target models also produce new states, where the length of the row of dipoles has a direct physical interpretation. The estimate of this length is also presented in Table 2 and do correspond to the size of the vehicles given in Figure 5. Notice that this length does not exactly correspond to the actual length of the vehicle since it is based on an approximation of the target using a finite number of dipoles. However, a long dipole row should indicate a long vehicle and vice versa, which then might be used for classifying vehicles of different sizes.

Initial state and Velocity Estimation

Furthermore, the extended target model produces reasonable estimates of the initial position $\hat{\mathbf{r}}_0$, Table 3, and the velocity $\hat{\mathbf{v}}_0$, Table 4. All target trajectories are almost parallel to the x -axis in accordance with the experimental setup. Furthermore, Vehicle 1, 3 and 4 are estimated to head in positive x -direction (right) (see Table 4), which is correct according to Figure 5.

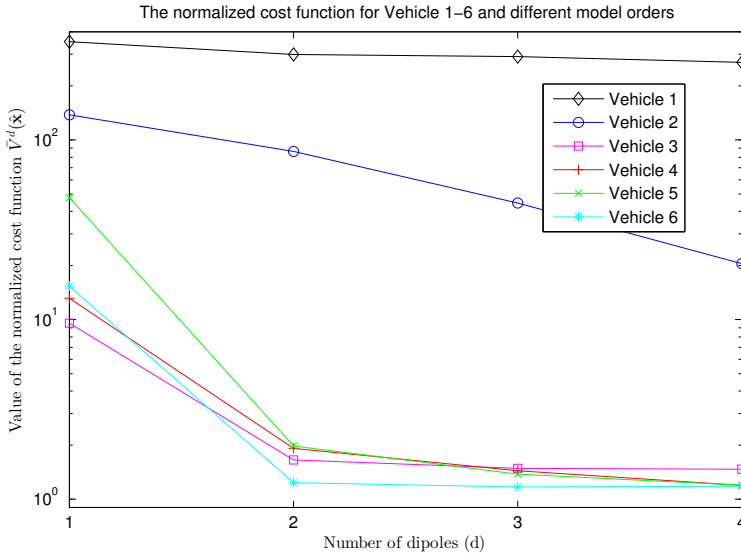


Figure 7: The normalized cost function $\bar{V}^d(\hat{\mathbf{x}})$ as a function of the model order d of the extended target model.

Height Estimation

The z -component of the initial position $\hat{\mathbf{r}}_0$ has the interpretation of being the height of the car's metallic center over the road plane. According to Table 3 this estimate is reasonable, being positive for all vehicles and significantly larger for Vehicle 1.

Dipole Estimation

Finally, by making use of the superposition principle (9), the total magnetic dipole moment of the vehicles can be calculated by summarizing all dipoles. This estimate is given in Table 5. However, for these values we do not have any reference data more than that large $\hat{\mathbf{m}}$ should correspond to large vehicles.

6.5 Validation of Direction Dependent Target Model

The decomposition the magnetic dipole moment \mathbf{m} into two components as described in (15) cannot be validated from only one scenario with constant heading since the two components cannot be resolved. As stated by Casalegno (2002), different observations of the same target at multiple headings are needed to allow the induced and permanent dipole moments to be resolved. In this validation, Vehicle 5, Figure 5e, has been used in controlled experiments heading at different speeds in four different directions, 2–4 times in each direction.

For each scenario the corresponding $\hat{\mathbf{m}}(\Psi)$ has been estimated with the row of dipoles extended target model with model order $d = 3$, which in Section 6.4 has

Table 2: The normalized cost function for the extended target model $d = 3$ and the estimated length between the first and the last dipole with the corresponding standard deviation.

Nr	$V(\hat{\mathbf{x}})/(Nn_y - n_x)$	N	n_y	n_x	Length [m]
1	302.6	70	6	22	9.09 (0.03)
2	76.7	54	6	22	11.25 (0.04)
3	1.6	32	6	22	3.95 (0.36)
4	1.5	44	6	22	3.56 (0.15)
5	1.5	27	6	22	4.98 (0.25)
6	1.3	22	6	22	2.07 (0.24)

Table 3: The estimated initial position $\hat{\mathbf{r}}_0$ in Cartesian coordinates (xyz) for the extended target model $d = 3$. Standard deviations in parenthesis. Also reference data for the three Cartesian coordinates is given. For example, for Vehicle 1 the x-component of $\hat{\mathbf{r}}_0$ is -12.47 m with a standard deviation of 0.04 m and according to the reference data this parameter should be negative.

Nr	Estimated initial position $\hat{\mathbf{r}}_0$ [m]						Ref. data
1	-12.47,	0.13,	4.36	(0.04,	0.02,	0.04)	-, 0, +
2	13.68,	-0.21,	0.32	(0.06,	0.03,	0.05)	+, 0, +
3	-10.49,	-1.47,	0.57	(0.27,	0.09,	0.09)	-, 0, +
4	-8.73,	-2.00,	0.25	(0.14,	0.08,	0.07)	-, 0, +
5	11.43,	-1.47,	0.59	(0.20,	0.10,	0.10)	+, 0, +
6	8.78,	0.93,	0.42	(0.22,	0.14,	0.09)	+, 0, +

been proved to be a good model. Now we define

$$\mathbf{Y} = \begin{bmatrix} \hat{\mathbf{m}}(\Psi_1) \\ \hat{\mathbf{m}}(\Psi_2) \\ \vdots \\ \hat{\mathbf{m}}(\Psi_i) \\ \vdots \\ \hat{\mathbf{m}}(\Psi_n) \end{bmatrix}, \quad \Phi^T = \begin{bmatrix} Q(\Psi_1) & \mathbf{B}_0/\mu_0 \\ Q(\Psi_2) & \mathbf{B}_0/\mu_0 \\ \vdots & \vdots \\ Q(\Psi_i) & \mathbf{B}_0/\mu_0 \\ \vdots & \vdots \\ Q(\Psi_n) & \mathbf{B}_0/\mu_0 \end{bmatrix}, \quad \boldsymbol{\theta} = \begin{bmatrix} \mathbf{m}_0 \\ D \end{bmatrix},$$

$$\mathbf{R} = \begin{bmatrix} \text{Cov}(\hat{\mathbf{m}}(\Psi_1)) & & \mathbf{0} \\ & \ddots & \\ \mathbf{0} & & \text{Cov}(\hat{\mathbf{m}}(\Psi_n)) \end{bmatrix},$$

where i are the different scenarios performed at heading angle Ψ_i . The weighted least squares estimate of $\boldsymbol{\theta}$ can be found by minimizing the residual $\|\mathbf{Y} - \Phi^T \hat{\boldsymbol{\theta}}\|_{\mathbf{R}}$, i.e. by solving

$$(\Phi \mathbf{R}^{-1} \Phi^T) \hat{\boldsymbol{\theta}} = \Phi \mathbf{R}^{-1} \mathbf{Y}$$

Table 4: The estimated velocity $\hat{\mathbf{v}}_0$ in Cartesian coordinates (xyz) for the extended target model $d = 3$. Standard deviations in parenthesis. Also reference data is given.

Nr	Estimated velocity $\hat{\mathbf{v}}_0$ [m/s]						Ref. data		
1	6.41,	-0.27,	-1.54	(0.02,	0.01,	0.02)	+	0,	0
2	-5.98,	0.20,	0.28	(0.03,	0.01,	0.02)	-	0,	0
3	7.37,	0.33,	0.21	(0.16,	0.06,	0.06)	+	0,	0
4	5.34,	0.28,	0.20	(0.08,	0.05,	0.04)	+	0,	0
5	-9.74,	0.34,	0.02	(0.15,	0.09,	0.08)	-	0,	0
6	-11.56,	1.18,	0.03	(0.25,	0.19,	0.11)	-	0,	0

Table 5: The values of the estimated total magnetic moment $\hat{\mathbf{m}} = \sum_{i=1}^d \hat{\mathbf{m}}^i$ in Cartesian coordinates (xyz) for the extended target model $d = 3$. Standard deviations in parenthesis. Also reference data for the three Cartesian coordinates is given.

Nr	Estimated dipole moment $\hat{\mathbf{m}}$ [Am ²]						$\ \hat{\mathbf{m}}\ $	Rf.
1	25,	-819,	-1528	(10,	5,	10)	1734	Large
2	305,	62,	-1872	(12,	5,	12)	1897	Large
3	-22,	-5,	-580	(8,	5,	13)	581	Small
4	-129,	-71,	-430	(8,	5,	12)	454	Small
5	-142,	142,	-438	(8,	7,	13)	482	Small
6	195,	-62,	-265	(10,	7,	19)	335	Small

with the corresponding covariance matrix

$$P = (\Phi R^{-1} \Phi^T)^{-1}.$$

The estimated parameters $\hat{\theta} = \begin{bmatrix} \hat{m}_0 \\ \hat{D} \end{bmatrix}$ are given in Table 6 together with their standard deviations $\sqrt{P_{ii}}$.

Table 6: The estimated hard iron dipole moment $\hat{\mathbf{r}}_0$ in Cartesian coordinates (xyz) and estimated soft iron scalar \hat{D} . Standard deviations in parenthesis.

Estimated hard iron dipole moment $\hat{\mathbf{m}}_0$ [Am ²]						\hat{D} [m ³]	
-203,	124,	-267	(2.1,	1.7,	4.9)	1.054	(0.011)

In order to validate (15), predictions of the magnetic dipole moment \mathbf{m} for new Ψ can be made by using $\hat{\mathbf{m}}_0$ and \hat{D}

$$\hat{\mathbf{m}}(\Psi) = Q(\Psi)\hat{\mathbf{m}}_0 + \frac{\hat{D}}{\mu_0}\mathbf{B}_0. \quad (53)$$

The predictions can be compared with the previously estimated $\hat{\mathbf{m}}(\Psi_i)$. In Figure 8 the excellent fit for the x- and y-component of $\hat{\mathbf{m}}(\Psi_i)$ and $\hat{\mathbf{m}}(\Psi_i)$ is displayed.

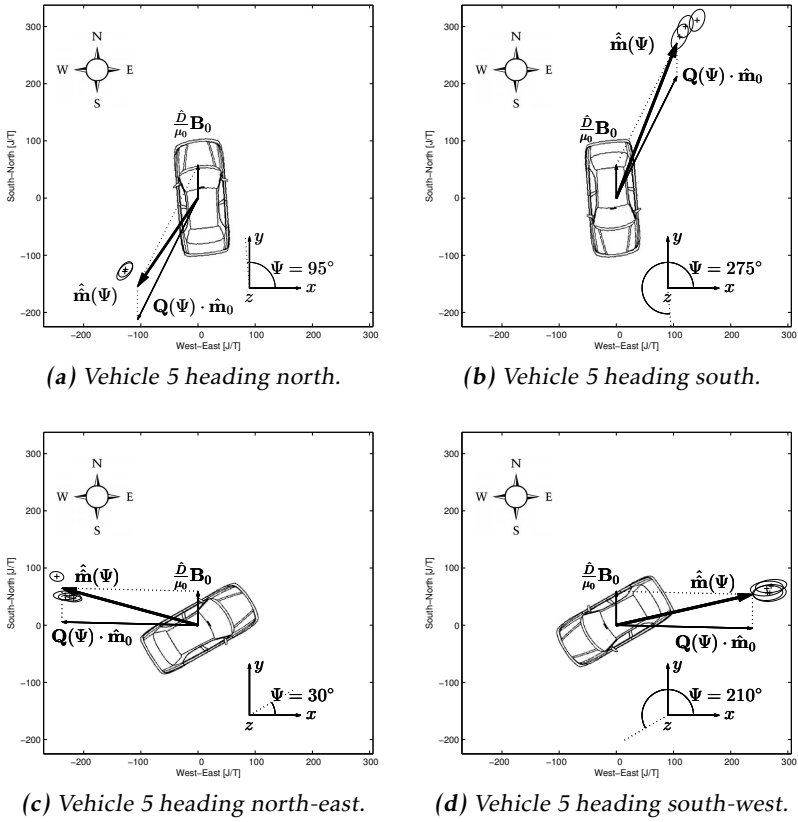


Figure 8: The estimated magnetic dipole moments $\hat{\mathbf{m}}(\Psi)$ (the crosses) for different heading angles Ψ given with a 90% confidence interval (the small ellipses) together with the simulated $\hat{\mathbf{m}}(\Psi)$ using the estimated parameter. The magnetic dipole moment can successfully be divided into two components, one being parallel to the earth magnetic field, and one being oriented in the reference frame of the vehicle.

By this it can be verified that the magnetic dipole moment \mathbf{m} can be decomposed into two components: one being parallel to the earth magnetic field with the scalar multiplier D/μ_0 , and one being oriented in the reference frame of the vehicle \mathbf{m}_0 where the parameters \mathbf{m}_0 and D are vehicle specific. Note that \mathbf{m}_0 and D cannot be found only from a single measurement since $\hat{\mathbf{m}}(\Psi)$ contains three components whereas \mathbf{m}_0 and D in total contains four. In other words, the target needs to make maneuvers in order to excite its complete magnetic signature.

7 Conclusions

In this paper, we have addressed the problem of localizing metallic targets using magnetometers. We have presented general sensor model based in the magnetic dipole model. This models has been extended by introducing a novel model consisting of a series of dipoles, which also contains the length of the vehicle in an extended state vector. Also a new model with heading angle dependent dipole moments has been proposed, which has been accomplished by decomposing the influence of soft and hard iron. The sensor model allows the target to be observed in an arbitrary magnetometer network.

We have also provided a detailed observability analysis of the model and compared it to other models based on the so called Anderson functions in the closest related papers.

Further, our model has been validated with a selection of dedicated field experiments. It has been found that the natural single dipole model does not work for larger vehicles when a commercial-grade sensor is used in its field of coverage. It has been found that this extended target model works excellently on small vehicles. However, for large vehicles challenging modeling work still remains. Finally, target orientation dependent dipole moment are identifiable only if the vehicle is observed in different orientations. Therefore, this model has been validated using the same vehicle in controlled experiments heading in different directions with excellent results. In addition, these experiments also verify that the dipole vectors are reproducible for a certain vehicle.

Bibliography

- M. Birsan. Non-linear Kalman filters for tracking a magnetic dipole. In *Proceedings of the International Conference on Marine Electromagnetics*, London, UK, Mar 2004.
- M. Birsan. Unscented particle filter for tracking a magnetic dipole target. In *Proceedings of MTS/IEE OCEANS*, Washington DC, USA, Sep 2005.
- M. Birsan. Electromagnetic source localization in shallow waters using Bayesian matched-field inversion. *Inverse Problems*, 22(1):43–53, 2006.
- J. Callmer, M. Skoglund, and F. Gustafsson. Silent localization of underwater sensors using magnetometers. *Eurasip Journal on Advances in Signal Processing*, 2009.
- J.W. Casalegno. All-weather vehicle classification using magnetometer arrays. In *Proceedings of SPIE Unattended Ground, Sea, and Air Sensor Technologies and Applications IX*, volume 4743, pages 205–212, Orlando, FL, USA, 2002. SPIE.
- S. Y. Cheung and P. Varaiya. Traffic surveillance by wireless sensor networks: Final report. Technical report, Traffic surveillance, University of California, Berkeley, 2007.
- S. Y. Cheung, S. Coleri, B. Dundar, S. Ganesh, C.W. Tan, and P. Varaiya. Traffic measurement and vehicle classification with single magnetic sensor. *Journal of the Transportation Research Board*, 2005.
- C.T. Christou and G.M. Jacyna. Vehicle detection and localization using unattended ground magnetometer sensors. In *Proceedings of 13th International Conference on Information Fusion*, Edinburgh, UK, Jul 2010.
- Z.A. Daya, D.L. Hutt, and T.C. Richards. Maritime electromagnetism and DRDC signature management research. Technical report, Defence R&D Canada, 2005.
- A.S. Edelstein. Magnetic tracking methods and systems, 2004. Patent.
- F. Gustafsson. *Statistical Sensor Fusion*. Studentlitteratur, 1 edition, 2010. Page 257-272.
- J.D. Jackson. *Classical Electrodynamics*. John Wiley and Sons, Inc., 3 edition, 1998.
- S.M. Kay. *Fundamentals of Statistical Signal Processing: Estimation Theory*. Prentice Hall, 1993. ISBN 0-13-345711-7.
- R. J. Kozick and B. M. Sadler. Joint processing of vector-magnetic and acoustic-sensor data. In *Proceedings of SPIE Unattended Ground, Sea, and Air Sensor Technologies and Applications IX*, volume 6562, Orlando, Florida, United States, April 2007a.
- R. J. Kozick and B. M. Sadler. Classification via information-theoretic fusion of vector-magnetic and acoustic sensor data. In *Proceedings of the International*

- Conference on Acoustics, Speech and Signal Processing*, volume 2, pages II-953 –II-956, april 2007b.
- R.J. Kozick and B.M. Sadler. Algorithms for tracking with an array of magnetic sensors. In *Proceedings of Sensor Array and Multichannel Signal Processing Workshop*, pages 423 –427, Jul 2008. doi: 10.1109/SAM.2008.4606904.
- J. Lenz. A review of magnetic sensors. *Proceedings IEEE*, 78:973–989, June 1990.
- J. Lenz and S. Edelstein. Magnetic sensors and their applications. *Sensors Journal, IEEE*, 6:631 –649, Jun 2006.
- J. C. Maxwell. A dynamical theory of the electromagnetic field. *Philosophical Transactions of the Royal Society of London*, 155:459–513, 1865.
- L. Merlat and P. Naz. Magnetic localization and identification of vehicles. In *Unattended Ground Sensor Technologies and Applications V*, volume 5090, pages 174–185. SPIE, 2003.
- M. Rakijas. Magnetic object tracking based on direct observation of magnetic sensor measurement, 2001. Patent.
- D. Törnqvist. Statistical fault detection with applications to IMU disturbances, 2006. Licentiate thesis.
- N. Wahlström and F. Gustafsson. Magnetometer modeling and validation for tracking metallic targets. *IEEE Transactions on Signal Processing*, 2012. Under revision.
- N. Wahlström, J. Callmer, and F. Gustafsson. Magnetometers for tracking metallic targets. In *Proceedings of 13th International Conference on Information Fusion (FUSION)*, Edinburgh, Scotland, July 2010.
- N. Wahlström, J. Callmer, and F. Gustafsson. Single target tracking using vector magnetometers. In *Proceedings of the International Conference on Acoustics, Speech and Signal Processing (ICASSP)*, pages 4332–4335, Prague, Czech Republic, May 2011.
- W.M. Wynn. Detection, localization, and characterization of static magnetic dipole sources. In *Detection and Identification of Visually Obscured Targets*, pages 337–374. Taylor and Francis, 1999.
- MTi and MTx User Manual and Technical Documentation*. Xsens Technologies B.V., <http://www.xsens.com>, 2005.

Paper B

Classification of Driving Direction in Traffic Surveillance using Magnetometers

Authors: Niklas Wahlström, Roland Hostettler, Fredrik Gustafsson and Wolfgang Birk

Edited version of the paper:

N. Wahlström, R. Hostettler, F. Gustafsson, and W. Birk. Classification of driving direction in traffic surveillance using magnetometers. *IEEE Transactions on Intelligent Transportation Systems*, 2012c. Submitted.

Early version of this work was presented in:

N. Wahlström, R. Hostettler, F. Gustafsson, and W. Birk. Rapid classification of vehicle heading direction with two-axis magnetometer. In *Proceedings of the International Conference on Acoustics, Speech and Signal Processing (ICASSP)*, pages 3385–3388, Kyoto, Japan, March 2012b.

Classification of Driving Direction in Traffic Surveillance using Magnetometers

Niklas Wahlström*, Roland Hostettler**, Fredrik Gustafsson* and Wolfgang Birk**

*Dept. of Electrical Engineering,
Linköping University,
SE-581 83 Linköping, Sweden
{nikwa, fredrik}@isy.liu.se

**Division of Systems and Interaction
Luleå University of Technology
SE-971 87, Luleå, Sweden
{rolhos, wolfgang}@ltu.se

Abstract

We present an approach for computing the driving direction of a vehicle by processing measurements from one 2-axis magnetometer. The proposed method relies on a non-linear transformation of the measurement data comprising only two inner products. Deterministic analysis of the signal model reveals how the driving direction affects the measurement signal and the proposed classifier is analyzed in terms of its statistical properties. The method is compared with a model based likelihood test using both simulated and experimental data. The experimental verification indicates that good performance is achieved under the presence of saturation, measurement noise, and near field effects.

1 Introduction

Existing methods for traffic monitoring such as inductive loops are more and more challenged by emerging solutions based on small-size, low-cost sensors such as microphones or magnetometers. These sensors are often incorporated in sensor nodes for wireless sensor networks (WSN). One of the biggest advantages of using this technology is its flexibility. Nodes can be easily deployed at points of interest and due to their connectivity, the measurement data can be made available almost instantly. Furthermore, the low cost makes them very attractive (Birk et al., 2009; Cheung and Varaiya, 2007; Chinrungrueng et al., 2010).

However, such sensor nodes also bring certain challenges. Generally, the energy budget is limited as the units are powered by either batteries or solar panels (Girban and Popa, 2010). Furthermore, computational resources are scarce for reasons such as power saving (e.g. duty-cycling of the computations or low-power processors) or sharing of the microcontroller between different tasks (measuring, computing, communication, etc.), see, for example, Giannecchini et al. (2004) or Yu and Prasanna (2005). Thus, it is very important that the computation

time for each task is reduced to a minimum, which emphasizes the need for low-complexity data processing algorithms.

One of the quantities of interest for road administrations, urban planners, or traffic management centers is traffic flow and, associated with that, the driving direction. Consider, for example, a single sensor monitoring a two lane road. In order to be able to quantify the traffic volume on the individual lanes, the driving direction is crucial or, if one sensor for each lane is used, one would like to exclude vehicles on the farther lane. Thus, the traffic volume that is normally measured by a simple detector can be analyzed more thoroughly and better conclusions for future measures such as road planning can be drawn. Another application where the driving direction is of utmost importance is the detection of wrong-way drivers. Wrong-way drivers are a very hazardous threat to other road users and can cause serious accidents (Moler, 2002). Particularly on highways, wrong-way drivers can cause serious head-on collisions and in 2010, wrong-way drivers accounted for 3.1 % of fatal crashes in the USA, causing 1,356 fatalities (National Highway Traffic Safety Administration, 2010). Thus, a system for detecting this kind of driving behavior can be of much help for authorities to detect vehicles driving in the wrong direction early on and warning other road users about the threat.

There are a number of different methods using various types of sensors for estimating the driving direction of a vehicle available today. One straight-forward approach is to use imaging sensors such as cameras or infrared laserscanners for tracking vehicles (Zhang and Forshaw, 1997; Goyat et al., 2006). Such sensors can provide very rich information and the driving direction of vehicles can be easily determined based on the estimated vehicle trajectory. However, challenging weather or illumination conditions degrade the performance significantly. One way of addressing this problem is to fuse the visual data with another type of sensor as proposed by Pucher et al. (2010) where a combination of a camera and a microphone array was used. While these approaches are viable and used in practice, they are not well suited for large scale deployment (for example at every highway ramp) due to their requirements. Solutions more tailored for a system following the requirements stated in the beginning are often based on two spatially separated sensors (Cheung and Varaiya, 2007; Mimbela and Klein, 2000). However, the need for a second sensor can increase the cost considerably (up to twice the cost for only one sensor in the worst case) and introduces other challenges such as vehicle re-identification (Sun et al., 2004; Kwong et al., 2009) or the requirement of communication between the sensors (Pantazis and Vergados, 2007). Each of these activities will inevitably increase the energy consumption, which is a limited resource. Furthermore, a system based on only one single sensor is presumably more reliable since it does not depend on any second sensor that could break down.

In contrast to these approaches, this paper introduces a method for classifying the driving direction of a vehicle in a fast and efficient way addressing the initially stated requirements of a wireless sensor node. The method is based on one single

magnetometer which measures magnetic field distortions induced by vehicles in its vicinity. Intuitively, extracting size and speed from this signal is rather straightforward. The basic principle is that the peak value of the measured signal corresponds to the size of the car, and the duration of the response corresponds to the speed of the vehicle. However, obtaining the driving direction requires more physical insight about the signal. In its simplest form, the proposed driving direction classification method only comprises a difference of two inner products of two vectors (Wahlström et al., 2012a).

Specifically, the contributions of this work are:

- A driving direction classification method including a analysis of its statistical properties based on one single sensor.
- Verification of the proposed method using simulations as well as real measurement data.
- Comparison of the proposed method with a standard likelihood classification scheme.
- An optional sensor fusion strategy for a multi-sensor scenario.

The outline of this paper is as follows. The signal model describing the magnetic field distortion caused by a vehicle is presented in Section 2, followed by a likelihood classifier based on this model in Section 3. The signal property exploited to derive a simplified classifier is presented in Section 4 and the classifier and its statistical properties are given in Section 5. The properties are verified and discussed by using Monte Carlo simulations in Section 6 and finally, the method is applied to real data in Section 7, followed by conclusions in Section 8.

2 Signal Model

When a metallic target passes a stationary magnetometer, a distortion of the magnetic field is measured (Honeywell, 2005). This distortion contains rich information which is associated with both the target trajectory as well as target specific parameters. One example of such a distortion is shown in Figure 1, where two components of the magnetic vector field are measured.

In this work we are only interested in finding the driving direction of the target. Consequently, the method should be insensitive to other quantities such as velocity, distance between the sensor and the trajectory, magnetic signature, and target extension. Additionally, the following physical limitations of the sensor apply:

- *The magnetometer has only two axes:* This means that the magnetometer only measures the two components of the magnetic field parallel to the ground and not the third component orthogonal to the ground.
- *The signal might be saturated:* Especially when large targets pass close to the sensor, the measured distortion can become saturated as shown in Figure 1.

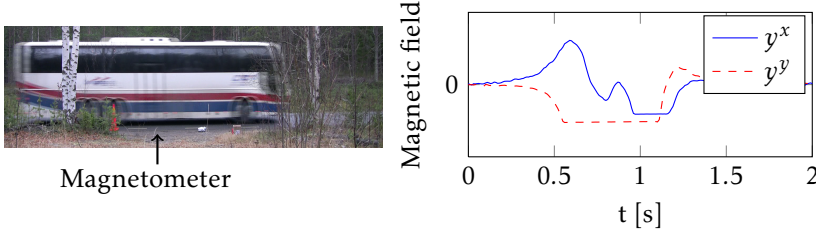


Figure 1: A metallic vehicle gives rise to a magnetic field distortion. Is it possible to determine the driving direction of the vehicle from this information?

- *Measurement noise:* The magnetometer measures the magnetic field disturbed by noise.

One way of solving the problem is to approximately model the target as a magnetic dipole. This approximation holds if the distance between the target and the sensor is large in comparison to the characteristic length of the target (Jackson, 1998). This gives rise to a magnetic dipole field $\mathbf{h}(t)$ expressed as

$$\mathbf{h}(t) = \frac{3(\mathbf{r}(t) \cdot \mathbf{m})\mathbf{r}(t) - \|\mathbf{r}(t)\|^2 \mathbf{m}}{\|\mathbf{r}(t)\|^5}, \quad (1a)$$

where $\mathbf{r}(t) = [r^x(t) \ r^y(t) \ r^z(t)]^\top$ is the position of the target relative to the sensor and $\mathbf{m} = [m^x \ m^y \ m^z]^\top$ is the magnetic dipole moment, which can be considered as a target specific parameter (Wahlström et al., 2010). Two components of the magnetic field (1a) can then be measured with a two-axis magnetometer

$$\begin{aligned} \mathbf{y}_k &= \begin{bmatrix} y^x(kT) \\ y^y(kT) \end{bmatrix} = \begin{bmatrix} h^x(kT) \\ h^y(kT) \end{bmatrix} + \begin{bmatrix} e^x(kT) \\ e^y(kT) \end{bmatrix} \\ &= \bar{\mathbf{h}}_k + \mathbf{e}_k, \end{aligned} \quad (1b)$$

where T is the sampling time, k denotes the sampling instant, $\bar{\mathbf{h}}_k$ is a 2×1 vector containing the x - and y -components (the first two components) of the 3×1 vector $\mathbf{h}_k = \mathbf{h}(kT)$, and \mathbf{e}_k is measurement noise assumed to be independent, zero mean white Gaussian noise of the form

$$\mathbf{e}_k \sim \mathcal{N}(0, \sigma^2 \mathbf{I}_2). \quad (1c)$$

where \mathbf{I}_2 is the 2×2 identity matrix.

The model in (1) can now be used to classify the motion direction of the vehicle. One way of doing this is by estimating the unknowns $\mathbf{r}(t)$ and \mathbf{m} from the measurement of \mathbf{y}_k and extract the direction information from the estimated trajectory $\hat{\mathbf{r}}(t)$. However, this is a non-linear problem and convergence to a global optimum is not guaranteed. Furthermore, if the target is close to the sensor, a higher order model including more parameters is needed to describe the sig-

nal accurately, for example by including higher order moments of the magnetic field or by modeling the target as a grid of dipoles (Wynn, 1999). Unfortunately, the computational cost of the corresponding estimation problem would in the worst case grow exponentially with the number of parameters (Boyd and Vandenberghe, 2004).

Instead, an approach using the above model in a likelihood ratio test with assumptions on certain parameters is derived first in the following section. This test can be seen as a common practice procedure and is often used in detection and classification problems in all kinds of disciplines and is thus also used as a benchmark (Kay, 1998; Root, 1970). Then, the signal model (1a) is analyzed more thoroughly and a unique feature providing the driving direction is derived in Section 4.

3 Likelihood Test

As indicated above, a straight-forward approach for classifying the driving direction of a vehicle is by deriving a likelihood ratio test based on the measurement model (1). This approach is pursued in this section.

3.1 Single Sensor

Assuming a vehicle passing the sensor with a constant velocity and constant lateral distance, \mathbf{r}_k can be rewritten as

$$\mathbf{r}_k = \mathbf{r}(kT) = \begin{bmatrix} v(kT - t_{\text{CPA}}) \\ r^y \\ 0 \end{bmatrix}, \quad (2)$$

where v is the vehicle speed, t_{CPA} is the closest point of approach time, and r^y the lateral distance between the target and the sensor.

It can be safely assumed that most of the vehicles will adhere to the known speed limit v_{limit} for a given road and thus, vehicles passing the sensor can be classified according to the following two hypotheses:

$$\mathcal{H}_L: \quad \boldsymbol{\theta}_1^* = [v_{\text{limit}} \quad r_1^y]^\top \quad (3a)$$

$$\mathcal{H}_R: \quad \boldsymbol{\theta}_2^* = [-v_{\text{limit}} \quad r_2^y]^\top, \quad (3b)$$

where $\boldsymbol{\theta}_i^*$ is the hypothesis parametrization which is known. The lateral distances r_1^y and r_2^y are derived from the road geometry. For example, in a traffic counting scenario, they would correspond to the distances to the closer and farther lane, respectively. On the other hand, when detecting wrong-way drivers on a highway ramp, they would be equal. The hypothesis \mathcal{H}_L corresponds to a vehicle passing the sensor from left to right and \mathcal{H}_R to a vehicle passing the sensor from right to left.

The remaining parameters $\boldsymbol{\theta} = [m^x \quad m^y \quad m^z \quad t_{\text{CPA}}]^\top$ in (1a) are all unknown (op-

posite to θ^* which holds the known parameters determined as described above) and the measurement model can be rewritten as

$$\bar{\mathbf{h}}_k(\theta_i^*, \theta_i) = \begin{bmatrix} 1 & 0 & 0 \\ 0 & 1 & 0 \end{bmatrix} \cdot \frac{(3\mathbf{r}_k \mathbf{r}_k^\top + \|\mathbf{r}_k\|^2 \mathbf{I}_3)}{\|\mathbf{r}_k\|^5} \mathbf{m}, \quad (4)$$

where the position \mathbf{r}_k is a function of the parameters r_i^y , v_i and t_{CPA} as given by (2). The measurement model is linear in the unknown vehicle dependent parameters \mathbf{m} and non-linear in t_{CPA} . These have to be estimated before the actual likelihood test can be performed. This can be done by using a maximum likelihood estimator which yields a generalized likelihood ratio test (GLRT) (Kay, 1998).

The joint probability density function for all N vector samples is given by

$$\begin{aligned} p(Y_{1:N}; \theta_i^*, \theta_i) &= \prod_{k=1}^N p(\mathbf{y}_k; \theta_i^*, \theta_i) = \frac{1}{(2\pi\sigma^2)^N} \exp\left(-\frac{1}{2\sigma^2} \sum_{k=1}^N \|\mathbf{y}_k - \bar{\mathbf{h}}_k(\theta_i^*, \theta_i)\|_2^2\right) \\ &= \frac{1}{(2\pi\sigma^2)^N} \exp\left(-\frac{1}{2\sigma^2} \|Y_{1:N} - H_{1:N}(\theta_i^*, \theta_i)\|_2^2\right) \end{aligned} \quad (5)$$

where the measurement samples are stacked as $Y_{m:n} = [Y_{m:n}^x \quad Y_{m:n}^y]^\top$. Here $Y_{m:n}^\alpha = [y_m^\alpha \quad y_{m+1}^\alpha \quad \dots \quad y_n^\alpha]^\top$, and similarly for $H_{1:N}$. The maximum likelihood estimator (Kay, 1993) for the parameters θ_i is then simply

$$\hat{\theta}_i = \underset{\theta_i}{\operatorname{argmax}} p(Y_{1:N}; \theta_i^*, \theta_i) \quad \text{for } i = 1, 2. \quad (6)$$

Once the estimation $\hat{\theta}_i$ is obtained, the likelihood ratio can be calculated as

$$l = \frac{p(Y_{1:N}; \theta_1^*, \hat{\theta}_1)}{p(Y_{1:N}; \theta_2^*, \hat{\theta}_2)} \underset{\mathcal{H}_R}{\overset{\mathcal{H}_L}{\gtrless}} 1. \quad (7)$$

If $l > 1$, the hypothesis \mathcal{H}_L is more likely to be true and \mathcal{H}_R otherwise. Using (5) and (7), the log-likelihood ratio is given by

$$\begin{aligned} \lambda &= \log(l) \\ &= -\frac{1}{2\sigma^2} \|Y_{1:N} - H_{1:N}(\theta_1^*, \hat{\theta}_1)\|_2^2 + \frac{1}{2\sigma^2} \|Y_{1:N} - H_{1:N}(\theta_2^*, \hat{\theta}_2)\|_2^2 \underset{\mathcal{H}_R}{\overset{\mathcal{H}_L}{\gtrless}} 0 \end{aligned} \quad (8)$$

and the decision rule becomes

$$\tilde{\lambda}_1 \underset{\mathcal{H}_R}{\overset{\mathcal{H}_L}{\gtrless}} \tilde{\lambda}_2 \quad (9)$$

with

$$\tilde{\lambda}_i = -\|Y_{1:N} - H_{1:N}(\theta_i^*, \hat{\theta}_i)\|_2^2 \quad (10)$$

Note that the two test statistics $\tilde{\lambda}_1$ and $\tilde{\lambda}_2$ are easily calculated. However, the parameter estimation step to be executed still requires solving a (separable) non-

linear problem. Hence, this method is not well tailored for implementation in systems with limited computational power since it requires an iterative solver which might not converge to the global optimum.

3.2 Sensor Fusion

If there is data from more than one sensor available, the likelihood test can take advantage of all this information in order to make a well-balanced decision. For J sensors, the joint PDF is given by

$$p(\Upsilon; \theta_i^*, \theta_i) = \prod_{j=1}^J p(Y_{1:N,j}; \theta_i^*, \theta_i), \quad (11)$$

where $\Upsilon = [Y_{1:N,1}^\top \ Y_{1:N,2}^\top \ \dots \ Y_{1:N,J}^\top]^\top$. The overall likelihood ratio and decision rule are then given by

$$l_J = \frac{p(\Upsilon; \theta_1^*, \theta_1)}{p(\Upsilon; \theta_2^*, \theta_2)} \underset{\mathcal{H}_R}{\overset{\mathcal{H}_L}{\geq}} 1, \quad (12)$$

which results in the log likelihood

$$\lambda_J = \log(l_J) = \sum_{j=1}^J \frac{1}{2\sigma_j^2} \tilde{\lambda}_{1,j} - \sum_{j=1}^J \frac{1}{2\sigma_j^2} \tilde{\lambda}_{2,j} = \sum_{j=1}^J \frac{1}{2\sigma_j^2} (\tilde{\lambda}_{1,j} - \tilde{\lambda}_{2,j}) \underset{\mathcal{H}_R}{\overset{\mathcal{H}_L}{\geq}} 0. \quad (13)$$

Finally, if all the sensors suffer from the same noise, that is, $\sigma_j^2 = \sigma^2$ for all $j = 1, \dots, J$, then (13) simplifies to

$$\sum_{j=1}^J \tilde{\lambda}_{1,j} \underset{\mathcal{H}_R}{\overset{\mathcal{H}_L}{\geq}} \sum_{j=1}^J \tilde{\lambda}_{2,j}. \quad (14)$$

4 Integral Feature

Even though the method introduced in Section 3 yields a valid test for determining the driving direction, it will be shown in this section that the nature of the measured signal carries the same information in a way that can be exploited more easily.

4.1 Measurement Data Example

Consider the two dimensional magnetometer signal in Figure 1. The desired information can partly be revealed by plotting the two components of the measurement against each other in a graph as presented in Figure 2a. As it will be shown, the measurement trajectory is turning clockwise in the x - y -plane as time increases. Further, it is easy to realize that the measurement trajectory would turn counterclockwise if the same vehicle reversed in the opposite direction. This can be seen by changing the time direction for the measurement sequence. Con-

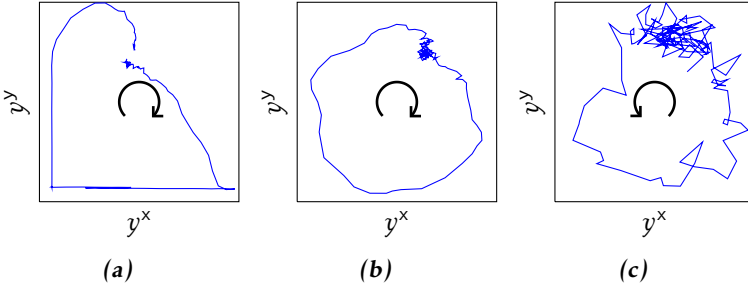


Figure 2: Measurement trajectories for three different vehicles. Figures (a) and (b) display vehicles passing from left to right, (c) vehicle passing from right to left. The arrow indicates the direction of the measurement trajectory as time increases.

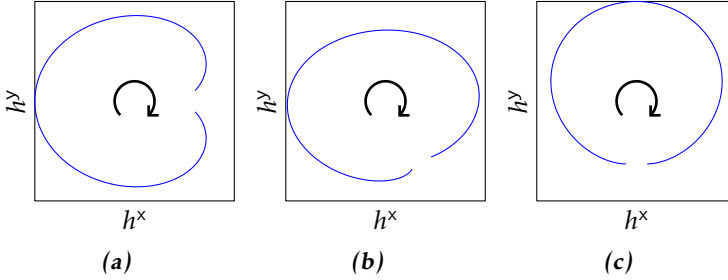


Figure 3: Simulated trajectories for vehicles moving from left to right with (a) $\mathbf{m} = [1 \ 0 \ 0]^T$, (b) $\mathbf{m} = [1 \ 1 \ 0]^T$, and (c) $\mathbf{m} = [0 \ 1 \ 0]^T$.

sequently, the rotation direction of the measurement trajectory might indicate the driving direction of the target. The equivalent plot can be made for other vehicles, and, according to Figures 2b and 2c, this pattern is observed for them as well.

Next, the dipole model (1a) is used in order to see whether this observation is supported by the model or not.

4.2 Simulated Example

Assume a linear trajectory orthogonal to the z -direction $\mathbf{r}(t) = [t \ 1 \ 0]^T$ and a magnetic dipole moment $\mathbf{m} = [m^x \ m^y \ m^z]^T$. From (1a) we obtain

$$\mathbf{h}(t) = \frac{1}{\sqrt{t^2 + 1}^5} \begin{bmatrix} 2m^x t^2 + 3m^y t - m^x \\ -m^y t^2 + 3m^x t + 2m^x \\ (t^2 + 1)m^z \end{bmatrix}. \quad (15)$$

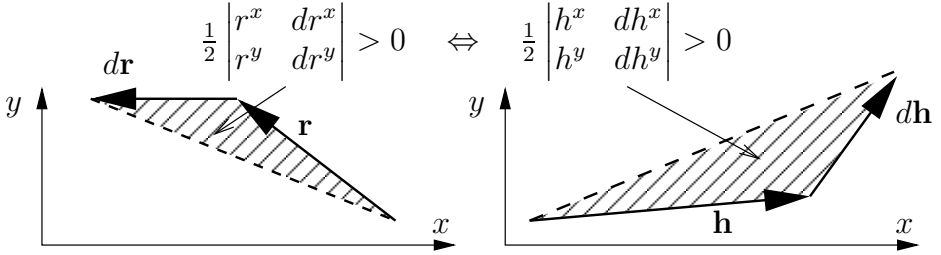


Figure 4: Graphical illustration of Theorem 1.

By plotting the x and y components of $\mathbf{h}(t)$ against each other for different values of \mathbf{m} , we conclude that all trajectories of $\mathbf{h}(t)$ turn clockwise (see Figure 3). To prove this property for this special case, one can form the function $\arctan(h^y(t)/h^x(t))$, differentiate with respect to time and prove that it is always negative (since the car passes from left to right in this example). However, we will provide a formal proof of the more general case in the next section.

Furthermore, from (15) we observe that the $h^z(t)$ does not contain any driving direction information since it is an even function, which is a consequence of the assumption that $r^z(t) = 0$. Thus, for a magnetometer only measuring the x - and y -components of the magnetic field, the exclusion of the z -component should not lead to any information loss regarding the driving direction.

4.3 Deterministic Analysis

Next, we will prove that the conclusion from the example will hold for all \mathbf{m} and arbitrary trajectories as long as they lie in the x - y -plane. The proof is accomplished by computing the area that the target trajectory and the measurement trajectory are enclosing. These two areas will be proved to have the same sign. For an infinitesimal position change $d\mathbf{r}$ this area equalizes the area of the triangle that \mathbf{r} and $d\mathbf{r}$ are spanning, see Figure 4. From linear algebra it is known that this area can be computed with the determinant of the 2×2 -matrix, whose columns consist of the vectors spanning the triangle.

Theorem 1 will show that this area has the same sign for the target trajectory as for the measurement trajectory. Consequently, if the target trajectory is turning clockwise around the sensor, the trajectory of the magnetic field $\mathbf{h}(t)$ will also turn clockwise and vice versa. This is also illustrated in Figure 4.

1 Theorem. *Assume the magnetic dipole model*

$$\mathbf{h} = \frac{3(\mathbf{r} \cdot \mathbf{m})\mathbf{r} - \|\mathbf{r}\|^2\mathbf{m}}{\|\mathbf{r}\|^5}. \quad (16)$$

Let $\mathbf{r} = [r^x \ r^y \ 0]^T$, $d\mathbf{r} = [dr^x \ dr^y \ 0]^T$ and $\mathbf{m} = [m^x \ m^y \ m^z]^T$. Then,

$$\begin{vmatrix} h^x & dh^x \\ h^y & dh^y \end{vmatrix} = \beta \begin{vmatrix} r^x & dr^x \\ r^y & dr^y \end{vmatrix}, \quad \beta > 0, \quad (17)$$

where

$$\begin{bmatrix} h^x & h^y & h^z \end{bmatrix}^T \triangleq \mathbf{h} \quad \text{and} \quad \begin{bmatrix} dh^x & dh^y & dh^z \end{bmatrix}^T \triangleq d\mathbf{h} = \frac{\partial \mathbf{h}}{\partial \mathbf{r}} d\mathbf{r}.$$

Proof: Starting from (16) we can compute

$$d\mathbf{h} = \frac{\partial \mathbf{h}}{\partial \mathbf{r}} d\mathbf{r} = \frac{3}{\|\mathbf{r}\|^5} \left((\mathbf{r} \cdot \mathbf{m}) d\mathbf{r} + (\mathbf{m} \cdot d\mathbf{r}) \mathbf{r} + (\mathbf{r} \cdot d\mathbf{r}) \mathbf{m} - 5 \frac{(\mathbf{r} \cdot \mathbf{m})(\mathbf{r} \cdot d\mathbf{r})}{(\mathbf{r} \cdot \mathbf{r})} \mathbf{r} \right). \quad (18)$$

Now, define the notation of a pair of two orthogonal 2-dimensional vectors from $\mathbf{u} \in \mathbb{R}^3$

$$\bar{\mathbf{u}} = [u^x \ u^y]^T \quad \text{and} \quad \bar{\mathbf{u}}_{\perp} = [u^y \ -u^x]^T, \quad (19)$$

where $\mathbf{u} = [u^x \ u^y \ u^z]^T$. Furthermore, for $\bar{\mathbf{u}}, \bar{\mathbf{v}}, \bar{\mathbf{w}} \in \mathbb{R}^2$ it can easily be verified that

$$(\bar{\mathbf{u}} \cdot \bar{\mathbf{v}}_{\perp}) = -(\bar{\mathbf{u}}_{\perp} \cdot \bar{\mathbf{v}}) \quad (20a)$$

$$(\bar{\mathbf{u}} \cdot \bar{\mathbf{u}})(\bar{\mathbf{v}} \cdot \bar{\mathbf{w}}) = (\bar{\mathbf{v}} \cdot \bar{\mathbf{u}})(\bar{\mathbf{u}} \cdot \bar{\mathbf{w}}) + (\bar{\mathbf{v}} \cdot \bar{\mathbf{u}}_{\perp})(\bar{\mathbf{u}}_{\perp} \cdot \bar{\mathbf{w}}). \quad (20b)$$

In addition, we also notice that a 2×2 determinant can be rewritten as an inner product

$$\begin{vmatrix} u^x & v^x \\ u^y & v^y \end{vmatrix} = (\bar{\mathbf{u}} \cdot \bar{\mathbf{v}}_{\perp}). \quad (21)$$

Since $r^z = 0$ and $dr^z = 0$, the two-dimensional version of (16) and (18) can now easily be stated as

$$\bar{\mathbf{h}} = \frac{3(\bar{\mathbf{r}} \cdot \bar{\mathbf{m}})\bar{\mathbf{r}} - \|\bar{\mathbf{r}}\|^2 \bar{\mathbf{m}}}{\|\bar{\mathbf{r}}\|^5} \quad (22a)$$

$$d\bar{\mathbf{h}} = \frac{3}{\|\bar{\mathbf{r}}\|^5} \left((\bar{\mathbf{r}} \cdot \bar{\mathbf{m}}) d\bar{\mathbf{r}} + (\bar{\mathbf{m}} \cdot d\bar{\mathbf{r}}) \bar{\mathbf{r}} + (\bar{\mathbf{r}} \cdot d\bar{\mathbf{r}}) \bar{\mathbf{m}} - 5 \frac{(\bar{\mathbf{r}} \cdot \bar{\mathbf{m}})(\bar{\mathbf{r}} \cdot d\bar{\mathbf{r}})}{(\bar{\mathbf{r}} \cdot \bar{\mathbf{r}})} \bar{\mathbf{r}} \right). \quad (22b)$$

Combining (22) and the identities (20) yields

$$\begin{aligned} \frac{\|\bar{\mathbf{r}}\|^{10}}{3} (\bar{\mathbf{h}} \cdot d\bar{\mathbf{h}}_{\perp}) &= 3(\bar{\mathbf{r}} \cdot \bar{\mathbf{m}})^2 (\bar{\mathbf{r}} \cdot d\bar{\mathbf{r}}_{\perp}) + \underbrace{(\bar{\mathbf{r}} \cdot \bar{\mathbf{m}})(\bar{\mathbf{r}} \cdot d\bar{\mathbf{r}})(\bar{\mathbf{m}} \cdot \bar{\mathbf{r}}_{\perp}) - \|\bar{\mathbf{r}}\|^2 (\bar{\mathbf{m}} \cdot \bar{\mathbf{r}})(\bar{\mathbf{m}} \cdot d\bar{\mathbf{r}}_{\perp})}_{+(\bar{\mathbf{r}} \cdot \bar{\mathbf{m}}_{\perp})^2 (\bar{\mathbf{r}} \cdot d\bar{\mathbf{r}}_{\perp})} \\ &\quad + \underbrace{(\bar{\mathbf{r}} \cdot \bar{\mathbf{m}})(\bar{\mathbf{r}} \cdot d\bar{\mathbf{r}})(\bar{\mathbf{m}} \cdot \bar{\mathbf{r}}_{\perp}) - \|\bar{\mathbf{r}}\|^2 (\bar{\mathbf{m}} \cdot d\bar{\mathbf{r}})(\bar{\mathbf{m}} \cdot \bar{\mathbf{r}}_{\perp})}_{-(\bar{\mathbf{r}} \cdot \bar{\mathbf{m}})^2 (\bar{\mathbf{r}} \cdot d\bar{\mathbf{r}}_{\perp})} \\ &= \left[2(\bar{\mathbf{r}} \cdot \bar{\mathbf{m}})^2 + (\bar{\mathbf{r}} \cdot \bar{\mathbf{m}}_{\perp})^2 \right] (\bar{\mathbf{r}} \cdot d\bar{\mathbf{r}}_{\perp}). \end{aligned}$$

Finally, by using the relation (21), we will arrive at the result in (17) with

$$\beta \triangleq \frac{3}{\|\mathbf{r}\|^{10}} \left[2(\bar{\mathbf{r}} \cdot \bar{\mathbf{m}})^2 + (\bar{\mathbf{r}} \cdot \bar{\mathbf{m}}_{\perp})^2 \right] > 0. \quad (23)$$

□

We can now define an indicator for the driving direction based on the magnetic field components by integrating over all infinitesimal area segments

$$f^{\star} = \int \left| \begin{matrix} h^x & dh^x \\ h^y & dh^y \end{matrix} \right| = \int \left| \begin{matrix} h^x(t) & dh^x(t)/dt \\ h^y(t) & dh^y(t)/dt \end{matrix} \right| dt. \quad (24)$$

Finally, the discrete time version of (24) will then be

$$f = \sum_{k=1}^{N-1} \left| \begin{matrix} h_k^x & (h_{k+1}^x - h_k^x)/T \\ h_k^y & (h_{k+1}^y - h_k^y)/T \end{matrix} \right| T = \sum_{k=1}^{N-1} (h_k^x h_{k+1}^y - h_k^y h_{k+1}^x). \quad (25)$$

which corresponds to the sum of the triangles spanned by two adjacent samples of the trajectory. Note that since all the triangles are completely enclosed in the true trajectory, f systematically underestimates the true area f^{\star} .

5 Cross-Correlation based Classifier

As shown in Section 4, the direction information can be obtained by computing the rotation direction of the magnetic field vector components. However, due to the noise that disturbs the measurement as illustrated in (1b), the stochastic properties of the noise have to be taken into account when calculating the driving direction. This section shows how this can be handled. Note that the assumption

$$\bar{\mathbf{h}}_k = \mathbf{0} \quad \text{for } k \leq 0 \vee k > N, \quad (26)$$

that is, that the magnetic signal has decayed to zero within the given window of N samples (however, \mathbf{e}_k is non-zero) is made throughout the rest of the paper.

5.1 Cross-Correlation with Lag One

A straight forward way to estimate f in (25) is to directly replace the true magnetic field vector $\bar{\mathbf{h}}$ with its noisy counterpart $\bar{\mathbf{y}}$

$$\hat{f} = \sum_{k=1}^N (y_k^x y_{k+1}^y - y_k^y y_{k+1}^x). \quad (27)$$

which can be interpreted as being the difference of the cross-correlations between y^x and y^y with lag 1 and -1 respectively. Since the measurement noise is assumed to be zero mean and i.i.d. (1c), it can be easily shown that the estimator (27) is

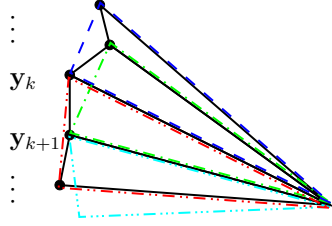


Figure 5: The estimator \hat{f} sums over the black solid line triangles whereas \hat{f}_2 averages over the colored dashed triangles.

unbiased

$$\begin{aligned} \mathbb{E}[\hat{f}] &= \mathbb{E}\left[\sum_{k=1}^N (y_k^x y_{k+1}^y - y_k^y y_{k+1}^x)\right] = \sum_{k=1}^N \mathbb{E}[y_k^x y_{k+1}^y - y_k^y y_{k+1}^x] \\ &= \sum_{k=1}^N h_k^x h_{k+1}^y - h_k^y h_{k+1}^x = f. \end{aligned} \quad (28)$$

Further, the variance of (27) is given by

$$\begin{aligned} \sigma_{\hat{f}}^2 &\triangleq \text{Var}(\hat{f}) = \mathbb{E}[(\hat{f} - \mathbb{E}[\hat{f}])^2] \\ &= \mathbb{E}\left[\left(\frac{1}{p} \sum_{k=1}^N (h_k^x + e_k^x)(h_{k+1}^y + e_{k+1}^y) - (h_k^y + e_k^y)(h_{k+1}^x + e_{k+1}^x) - (h_k^x h_{k+1}^y - h_k^y h_{k+1}^x)\right)^2\right] \\ &= \mathbb{E}\left[\left(\sum_{k=1}^N h_k^x e_{k+1}^y + h_{k+1}^y e_k^x - h_k^y e_{k+1}^x - h_{k+1}^x e_k^y + e_{k+1}^y e_k^x - e_{k+1}^x e_k^y\right)^2\right]. \end{aligned} \quad (29)$$

Analyzing the sum in (29) it can be seen that every e_k^α appears twice in the whole sum, once scaled by h_{k+1}^β and once by $-h_{k-1}^\beta$ (where the superscript β denotes the in-plane component perpendicular to α). Making use of this and (26) yields

$$\begin{aligned} \sigma_{\hat{f}}^2 &= \mathbb{E}\left[\left(\sum_{k=1}^N (h_{k+1}^y - h_{k-1}^y) e_k^x - (h_{k+1}^x - h_{k-1}^x) e_k^y + e_{k+1}^y e_k^x - e_{k+1}^x e_k^y\right)^2\right] \\ &= \sigma^2 \sum_{k=1}^N \left\| (\bar{\mathbf{h}}_{k+1} - \bar{\mathbf{h}}_{k-1}) \right\|^2 + 2N\sigma^4. \end{aligned} \quad (30)$$

From (30) it is seen that the variance is increased by the norm of the (approximate) gradient of the magnetic field vector $\nabla \mathbf{h}_k \approx \|(\bar{\mathbf{h}}_{k+1} - \bar{\mathbf{h}}_{k-1})\|/2$ as well as the window length. Finally, note that the distribution of \hat{f} is given by $\hat{f} \sim \mathcal{N}(f, \sigma_{\hat{f}}^2)$ as $N \rightarrow \infty$ as shown in Proposition 2 in Appendix A using $p = 1$.

5.2 Cross-Correlation with Arbitrary Lag

As shown above, the variance in the cross-correlation method with lag 1 scales badly if the noise is large since the second term in (30) scales with σ^4 . It is thus desirable to reduce this effect. This can be achieved by using an averaging estimator with lag p in order to reduce the noise sensitivity. Instead of calculating the triangular area of two neighboring measurement points k and $k + 1$ on the trajectory, larger area segments between the points k and $k + p$ are considered. This procedure is illustrated in Figure 5. In this case, however, each individual segment between k and $k + 1$ will be counted p times and thus, the estimator has to be normalized by $1/p$. This yields the cross-correlation estimator with lag p

$$\hat{f}_p = \frac{1}{p} \sum_{k=1}^N (y_k^x y_{k+p}^y - y_k^y y_{k+p}^x). \quad (31)$$

Analog to (28) it is straight forward to show that for $p \neq 1$

$$\mathbb{E}[\hat{f}_p] = \frac{1}{p} \underbrace{\sum_{k=1}^N h_k^x h_{k+p}^y - h_k^y h_{k+p}^x}_{\triangleq f_p} \neq f \quad (32)$$

and (31) is thus a biased estimator of (25). However, since only the sign of f is of interest, this is acceptable. The variance is given by

$$\begin{aligned} \sigma_{\hat{f}_p}^2 &\triangleq \text{Var}(\hat{f}_p) = \mathbb{E}[(\hat{f}_p - \mathbb{E}[\hat{f}_p])^2] \\ &= \mathbb{E}\left[\left(\frac{1}{p} \sum_{k=1}^N (h_k^x + e_k^x)(h_{k+p}^y + e_{k+p}^y) - (h_k^y + e_k^y)(h_{k+p}^x + e_{k+p}^x) - (h_k^x h_{k+p}^y - h_k^y h_{k+p}^x)\right)^2\right] \\ &= \mathbb{E}\left[\left(\frac{1}{p} \sum_{k=1}^N h_k^x e_{k+p}^y + h_{k+p}^y e_k^x - h_k^y e_{k+p}^x - h_{k+p}^x e_k^y + e_{k+p}^y e_k^x - e_{k+p}^x e_k^y\right)^2\right]. \end{aligned} \quad (33)$$

As in (29)-(30), the coefficients for e_k^α can be grouped which gives

$$\begin{aligned} \sigma_{\hat{f}_p}^2 &= \mathbb{E}\left[\left(\frac{1}{p} \sum_{k=1}^N (h_{k+p}^y - h_{k-p}^y) e_k^x - (h_{k+p}^x - h_{k-p}^x) e_k^y + e_{k+p}^y e_k^x - e_{k+p}^x e_k^y\right)^2\right] \\ &= \frac{\sigma^2}{p^2} \sum_{k=1}^N \|\bar{\mathbf{h}}_{k+p} - \bar{\mathbf{h}}_{k-p}\|^2 + \frac{2N}{p^2} \sigma^4. \end{aligned} \quad (34)$$

From (34) it is seen that the variance is greatly reduced compared to (30). The second term scales with $1/p^2$ compared to the second term in (30). As for the unbiased estimator \hat{f} , the distribution of \hat{f}_p converges to the normal distribution $\hat{f}_p \sim \mathcal{N}(f_p, \sigma_{\hat{f}_p}^2)$ where f_p is the mean value as illustrated in (32) (see Proposition 2 in Appendix A).

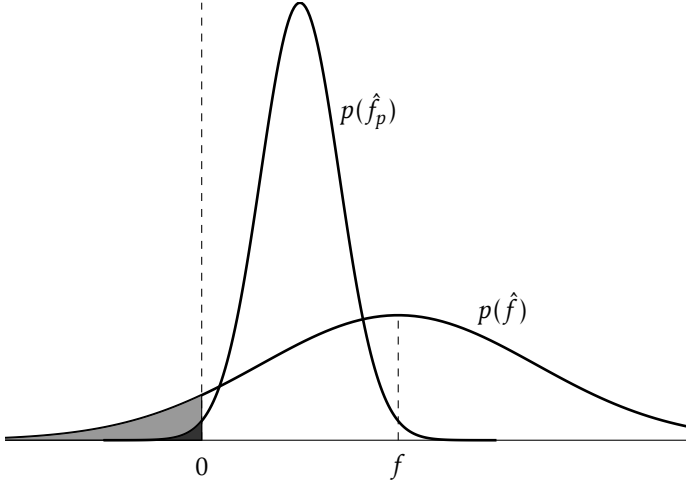


Figure 6: Comparison of the probability density functions of the estimators \hat{f} and \hat{f}_p . The expected value of \hat{f}_p is biased towards zero compared to \hat{f} , however, the error probability (shaded areas) is much smaller.

The averaging effect is illustrated in Figure 6. Assuming that the true value f is positive, the expected value of the averaging estimator is moved towards zero due to the bias. However, the averaging reduces the variance and thus the total error probability (the shaded area under the probability density function up to zero) is reduced significantly.

In practice, it is of interest to estimate the error probability coupled to the estimate \hat{f}_p obtained from (31). For that reason, the variance (34) is of interest. Noting that

$$\mathbb{E} \left[\|\mathbf{y}_{k+p} - \mathbf{y}_{k-p}\|^2 \right] = \mathbb{E} \left[(y_{k+p}^x - y_{k-p}^x)^2 + (y_{k+p}^y - y_{k-p}^y)^2 \right]$$

and letting $z_k^\alpha = y_{k+p}^\alpha - y_{k-p}^\alpha$ it follows that $z_k^\alpha \sim \mathcal{N}(h_{k+p}^\alpha - h_{k-p}^\alpha, 2\sigma^2)$. Thus,

$$\mathbb{E} \left[(z_k^x)^2 + (z_k^y)^2 \right] = (h_{k+p}^x - h_{k-p}^x)^2 + 2\sigma^2 + (h_{k+p}^y - h_{k-p}^y)^2 + 2\sigma^2$$

and finally

$$\mathbb{E} \left[\|\mathbf{y}_{k+p} - \mathbf{y}_{k-p}\|^2 \right] = \|\bar{\mathbf{h}}_{k+p} - \bar{\mathbf{h}}_{k-p}\|^2 + 4\sigma^2. \quad (35)$$

Using (34) and (35) we can then estimate $\text{Var}(\hat{f}_p)$ as follows

$$\begin{aligned}\hat{\sigma}_{\hat{f}_p}^2 &= \frac{\sigma^2}{p^2} \sum_{k=1}^N (\|\mathbf{y}_{k+p} - \mathbf{y}_{k-p}\|^2 - 4\sigma^2) + \frac{2N}{p^2} \sigma^4 \\ &= \frac{\sigma^2}{p^2} \sum_{k=1}^N \|\mathbf{y}_{k+p} - \mathbf{y}_{k-p}\|^2 - \frac{2N}{p^2} \sigma^4.\end{aligned}\quad (36)$$

The probability that the estimator \hat{f}_p takes on the wrong sign is given by

$$\Pr(\hat{f}_p < 0) = \int_{-\infty}^0 \mathcal{N}(x; f_p, \sigma_{\hat{f}_p}^2) dx = \frac{1}{2} \text{erfc}\left(\frac{f_p}{\sqrt{2}\sigma_{\hat{f}_p}}\right) \quad (37a)$$

for $f_p > 0$ and

$$\Pr(\hat{f}_p > 0) = \int_0^{\infty} \mathcal{N}(x; f_p, \sigma_{\hat{f}_p}^2) dx = \frac{1}{2} \text{erfc}\left(-\frac{f_p}{\sqrt{2}\sigma_{\hat{f}_p}}\right) \quad (37b)$$

for $f_p < 0$. (37) can be simplified for arbitrary f_p as

$$\Pr(\text{sgn}(\hat{f}_p) \neq \text{sgn}(f_p)) = \frac{1}{2} \text{erfc}\left(\frac{|f_p|}{\sqrt{2}\sigma_{\hat{f}_p}}\right). \quad (38)$$

Since neither the true f_p nor $\sigma_{\hat{f}_p}^2$ are known, the estimated values \hat{f}_p and $\hat{\sigma}_{\hat{f}_p}^2$ can be used instead. The estimated error probability (38) then becomes

$$\hat{P}_E = \frac{1}{2} \text{erfc}\left(\frac{|\hat{f}_p|}{\sqrt{2}\hat{\sigma}_{\hat{f}_p}}\right), \quad (39)$$

which can be evaluated numerically. Note, however, that (39) has a slightly different meaning than (38). It indicates the probability of f_p having a different sign compared to the given \hat{f}_p .

We can finally summarize the proposed estimators as follows

$$\hat{f}_p = \frac{1}{p} \left((\mathbf{Y}_{1:N}^x)^\top \mathbf{Y}_{(1+p):N+p}^y - (\mathbf{Y}_{1:N}^y)^\top \mathbf{Y}_{(1+p):N+p}^x \right) \stackrel{\mathcal{H}_R}{\underset{\mathcal{H}_L}{\gtrless}} 0 \quad (40a)$$

$$\begin{aligned}\hat{\sigma}_{\hat{f}_p}^2 &= \frac{\sigma^2}{p^2} \left((\mathbf{Y}_{1+p:N+p}^x - \mathbf{Y}_{1-p:N-p}^x)^\top \cdot (\mathbf{Y}_{1+p:N+p}^x - \mathbf{Y}_{1-p:N-p}^x) \right. \\ &\quad \left. + (\mathbf{Y}_{1+p:N+p}^y - \mathbf{Y}_{1-p:N-p}^y)^\top \cdot (\mathbf{Y}_{1+p:N+p}^y - \mathbf{Y}_{1-p:N-p}^y) \right) - \frac{2N}{p^2} \sigma^4,\end{aligned}\quad (40b)$$

where the notation $\mathbf{Y}_{m:n}^\alpha$ is defined in Section 3. Note that only simple additions, subtractions and inner products of vectors are used in order to calculate (40) which is very beneficial for efficient implementation.

5.3 Optimizing the Lag

The lag p introduced in (31) will improve the classification result as explained in Section 5.2. Our objective is to choose a value p which minimizes the overall estimated error probability (39). In theory this could be done for each detection separately. However, that would require a non-linear search in the parameter p for each detection, which does not meet the needs for a computationally efficient implementation. Instead we will minimize the mean of the estimated error probabilities from a training set of estimation data $l = 1, \dots, L$ and use this value p afterwards. Given a set of estimation data $(Y_{1:N})_{1:L}$ we compute p as

$$p = \underset{p}{\operatorname{argmin}} \frac{1}{L} \sum_{l=1}^L \hat{P}_{E,l} = \underset{p}{\operatorname{argmin}} \sum_{l=1}^L \operatorname{erfc} \left(\frac{|\hat{f}_{p,l}|}{\sqrt{2} \hat{\sigma}_{f_{p,l}}} \right). \quad (41)$$

After finding this value p , all future classifications can be performed by computing (40a) only by using the given value p .

5.4 Multiple Sensors

As with the likelihood test, information from multiple sensors can be fused together in order to arrive at a joint-classification of multiple sensors. The fusion rule (54) for Bernoulli random variables as derived in Appendix B is used in order to reach a joint decision of the driving direction of J sensors as follows. Let p_j be the probability that the car is passing the sensor from left to right (hypothesis \mathcal{H}_L true) which is given by

$$p_j = \Pr(\mathcal{H}_L | \hat{f}_{p,j}, \hat{\sigma}_{f_{p,j}}) = \frac{1}{2} \operatorname{erfc} \left(\frac{\hat{f}_{p,j}}{\sqrt{2} \hat{\sigma}_{f_{p,j}}} \right). \quad (42)$$

A Bernoulli random variable k with

$$p(k|p_j) = p_j^k (1 - p_j)^{1-k} \quad \text{for } k \in \{0, 1\} \quad (43)$$

can now be used to represent the probability of each hypothesis where the value $k = 0$ is assigned to \mathcal{H}_R and $k = 1$ to \mathcal{H}_L . Finally, using (54) (see Appendix B) and (43) yields the sensor fusion decision rule given by

$$\Pr(\mathcal{H}_L | \mathbf{p}) = \frac{\prod_{j=1}^J p_j}{\prod_{j=1}^J (1 - p_j) + \prod_{j=1}^J p_j} \underset{\mathcal{H}_L}{\overset{\mathcal{H}_R}{\geq}} \frac{1}{2}, \quad (44)$$

where $\mathbf{p} = [p_1 \ \dots \ p_J]^\top$. Equation (44) can also be rewritten as

$$\Pr(\mathcal{H}_L | \mathbf{p}) = \frac{\prod_{j=1}^J \Pr(\mathcal{H}_L | \hat{f}_{p,j})}{\prod_{j=1}^J \Pr(\mathcal{H}_R | \hat{f}_{p,j}) + \prod_{j=1}^J \Pr(\mathcal{H}_L | \hat{f}_{p,j})},$$

which can be interpreted as the joint probability for all sensors indicating \mathcal{H}_L at the same time, normalized by the sum of the same and its complementary event,

that is, all sensors indicating \mathcal{H}_R at the same time.

6 Simulation

Before applying the estimator derived in the previous section on real data, a simulation will be used to visualize and validate the results. Consider a discrete time version of the example in (15), with a linear trajectory heading in positive x -direction, starting at $\mathbf{r}_0 = [-5 \ 1 \ 0]^T$ and ending at $\mathbf{r}_{N-1} = [5 \ 1 \ 0]^T$ divided into $N = 100$ data points in between. Furthermore, assume a magnetic dipole moment of $\mathbf{m} = [1 \ 1 \ 1]^T$. We will simulate this example with different levels of the signal to noise ratio (SNR), which is defined as

$$\text{SNR} = 10 \log_{10} \left(\frac{\frac{1}{N} \sum_{k=1}^N \|\bar{\mathbf{h}}_k\|^2}{\sigma^2} \right) \quad [\text{dB}], \quad (45)$$

where σ^2 is the variance of the measurement noise.

6.1 Estimate and Variance Estimate

In (31) and (34) expressions of the mean $E[\hat{f}_p]$ and variance $\sigma_{\hat{f}_p}^2$ of the estimators are given. These expressions are verified by performing 1,000 Monte Carlo simulations for the presented example with different noise realization for each run. The result is presented in Figure 7 with $\text{SNR} = -10$ dB and $p = 15$ together with the theoretical distribution of the estimator $\hat{f}_p \sim \mathcal{N}(f_p, \sigma_{\hat{f}_p}^2)$.

According to the result, the theoretical distribution corresponds well to the empirical one. Furthermore, note that the estimate is biased $E[\hat{f}_p] \neq f$, as already stated in (34). We can also conclude that the Gaussian assumption of the estimator distribution is indeed valid.

Each sequence of data does not only provide us with the estimate (31), but also with an estimate of its variance (36). In Figure 8, this estimated variance is compared with the true variance, using the same 1,000 Monte Carlo simulations as previously. According to this result, the variance estimate seems to be unbiased as expected from the derivation.

6.2 Dependency of P_E on SNR and p

In (38) a scheme for computing the error probability is proposed by knowing the true mean and variance of the estimator. This value has been compared with the actual error classification rate by performing 1,000 Monte Carlo Simulations for different values of p and SNR. The result is provided in Figure 9 and the theoretical values display a good agreement with the simulations. Also the classification performance increases with higher SNR which is natural.

Furthermore, this result also displays the classification improvement of cross-

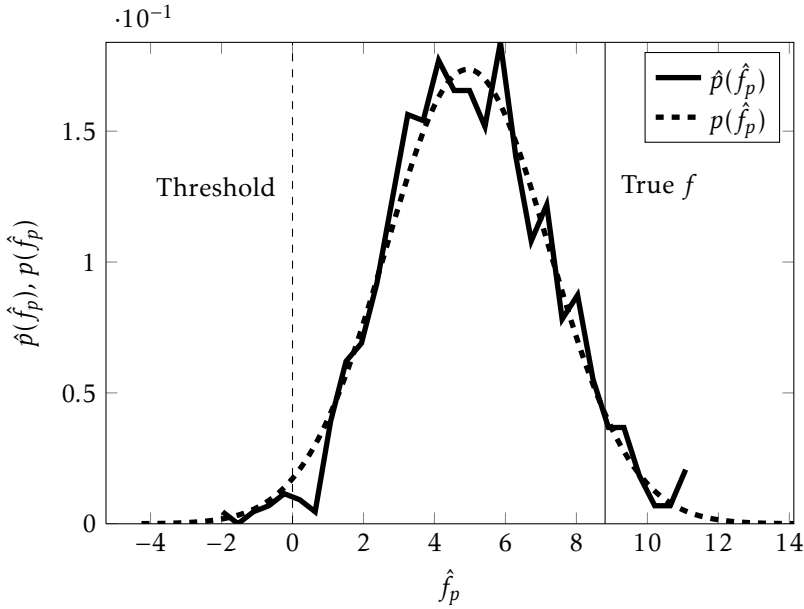


Figure 7: Empirical distribution $\hat{p}(\hat{f}_p)$ using simulated values of the estimator for SNR = -10 dB and $p = 15$ together with the theoretical distribution $p(\hat{f}_p)$.

correlation method by choosing a lag $p > 1$. Also note, that for the chosen simulation scenario, there is an optimal $p \approx 15$ which is fairly independent of the SNR. However, this will depend on the magnetic moment of the vehicle \mathbf{m} , the trajectory \mathbf{r}_k , and the data length N .

6.3 Comparison with Likelihood Test

The proposed classifier can now be compared to the likelihood test presented in Section 3. Again, 1,000 Monte Carlo simulations with $p = 15$ for the correlation classifier and the true values for v_1 , v_2 , r_1^y and r_2^y for the likelihood test were run. Figure 10 shows the error rates for the two classifiers as functions of the SNR. As it can be expected, both classifiers perform well for high SNRs, down to about -5 dB where the error rates start to increase until the point of "tossing a coin" somewhere below -20 dB is reached. It should be noted, however, that the correlation classifier requires an SNR of about 5 dB higher than the likelihood classifier in order to achieve the same classification rate. This is not very surprising since the likelihood test is expected to be the optimal test for this scenario since the likelihood test is performed under the same model and model parameter as we have been used in the simulation.

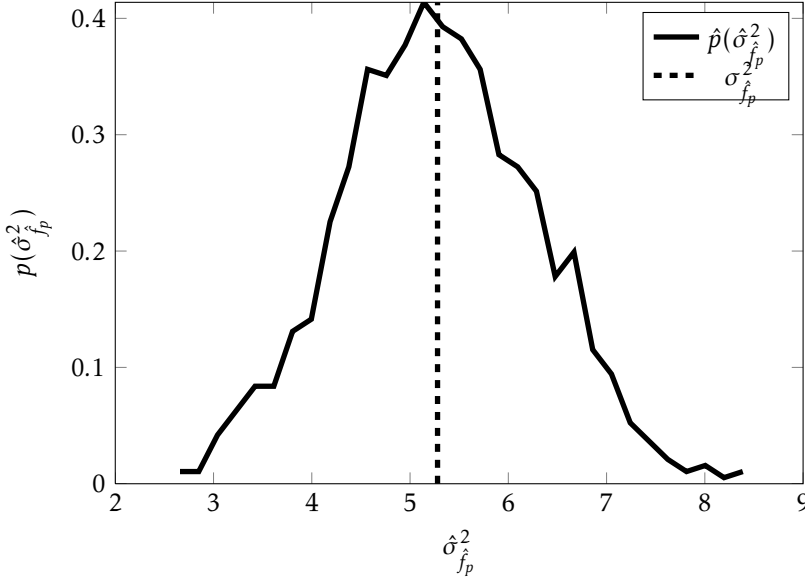


Figure 8: Empirical distribution $\hat{p}(\hat{\sigma}_{f_p}^2)$ using simulated values of the variance estimate for for SNR = -10 dB and $p = 15$ together with the theoretical variance.

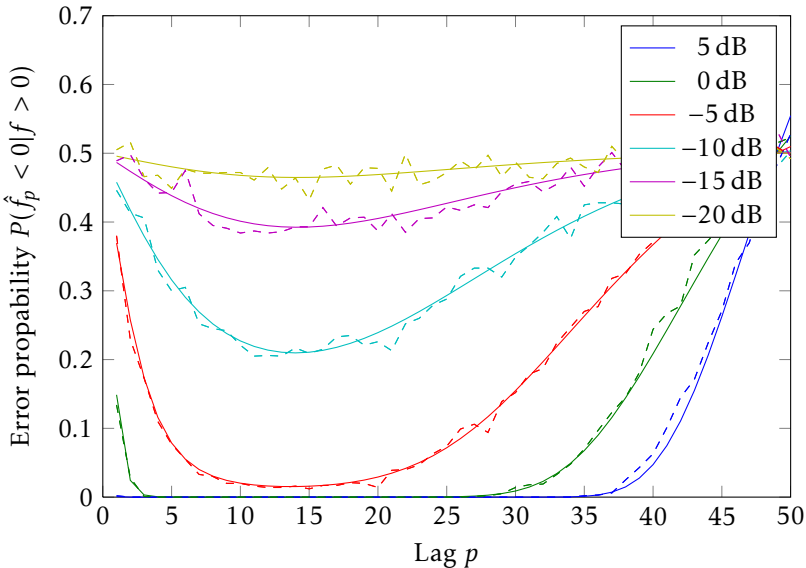


Figure 9: Classification performance as a function of the lag p for different SNRs . The solid line is the theoretical performance P_E according to (38) and the dashed line the average error probability of the 1,000 Monte Carlo simulations.

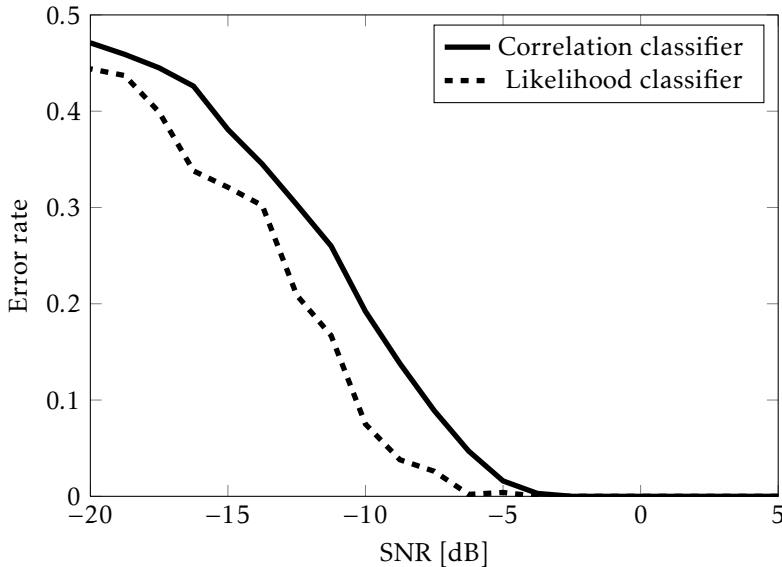


Figure 10: Classification performance compared with the likelihood test as a function of the SNR.

7 Experimental Results and Discussion

The simulations in the preceding section indicate that the proposed classifier works according to the expectations from its derivation. This section will now show how the classifier performs on real data where a bigger amount of uncertainty and challenges are to be expected.

7.1 Experiment Setup

Experiments were conducted in order to verify the proposed algorithm on real data. The measurements were performed on a two-way country road with moderate traffic density and a speed limit of 90 km/h. Two commercially available 2-axis magnetometers (Honeywell, 2007) including the corresponding signal conditioning and acquisition hardware sampling at 100 Hz were placed on both sides of the road as illustrated in Figure 11. The traffic was measured during three separate periods for a total of 158 minutes and 362 vehicles traveling south-north (close to sensor 1) and 305 vehicles traveling north-south (close to sensor 2) were measured. Furthermore, the whole experiment was recorded on video.

From the video recording the true passing time of the vehicles as well as their driving directions were manually determined in order to establish a ground truth. This ground truth was then used to extract the magnetometer signal from the raw measurement data in order to evaluate the direction classification algorithms as presented in the previous sections. In this way, the detection problem does not

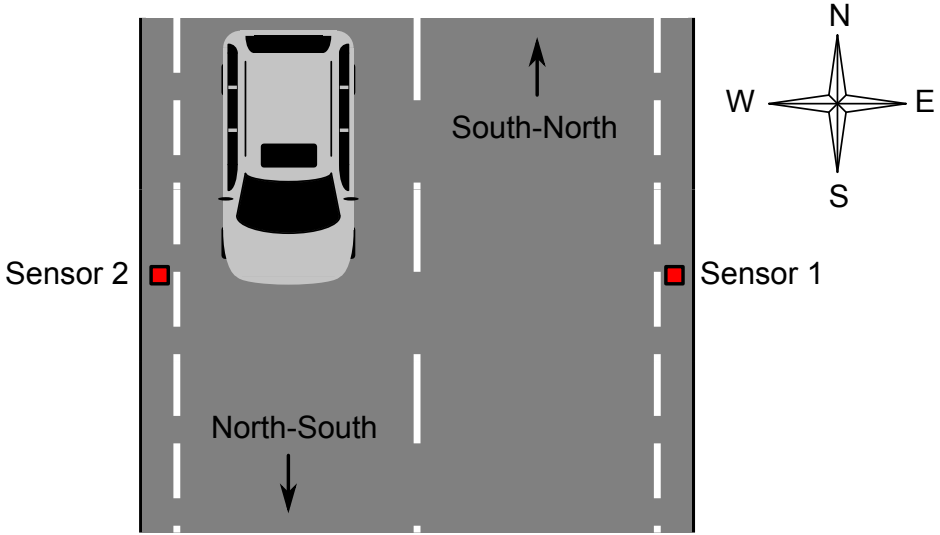


Figure 11: Illustration of the experiment setup showing the two sensors on each side of the road as well as the driving directions.

affect the comparison of the two classification algorithms.

Note that the two sensor setup is only used for increasing the amount of data and for evaluating the presented fusion framework. The presented classifier in its simplest form still only needs one sensor for classifying the driving direction.

7.2 Results

As indicated above, the ground truth data was used in order to measure the performance of the two classifiers. For each passage, a 1.5 s long time window from the magnetometer signal was extracted and the driving direction was determined. For the likelihood classifier introduced in Section 3, the chosen parametrization was as follows:

$$\begin{aligned}\mathcal{H}_L: \theta_1^* &= [25 \text{ m/s} \quad 3.5 \text{ m}] \\ \mathcal{H}_R: \theta_2^* &= [-25 \text{ m/s} \quad 6.5 \text{ m}]\end{aligned}$$

which corresponds to the actual road geometry and speed limit at the place where the measurements were performed. The loop detector was tuned using the tuning algorithm described in Section 5.3 using the first measurement set (71 vehicles close to sensor 1 and 85 vehicles close to sensor 2) resulting in $p = 11$.

Finally, the two algorithms were run on the remaining two datasets and the results are shown in Table 1. As it can be seen in the table, the correlation classifier performs very well. For the vehicles passing close to the sensor, only one out of the 511 vehicles is misclassified. As expected due to the lower SNR compared to vehicles passing close to the sensor, the performance is worse for the vehicles

Table 1: Results of applying the driving direction classification to the measurement data. For example, 290 out of the 291 vehicles traveling south-north were classified correctly by the correlation classifier using the measurements of sensor 1.

Direction	# Vehicles	Sensor 1		Sensor 2		Fusion	
		Correlation	Likelihood	Correlation	Likelihood	Correlation	Likelihood
South-North	291	290	278	265	215	283	273
North-South	220	189	164	220	210	211	207
Total	511	479	442	485	425	494	480

Table 2: Results of applying the driving direction classification to the measurement data. For example, 710 out of the 722 vehicles which are more than 2 second separated from the closest vehicle, were classified correctly by the cross-correlation based classifier.

Distance to closest vehicle	# Vehicles	Correlation	Likelihood
More than 2 s	722	710	642
Less than 2 s	300	254	225

passing on the lane farther from the sensor. Here, in total 57 vehicles are wrongly classified.

Also the likelihood classifier performs well for vehicles close to the sensor but not quite as well as the cross-correlation classifier. 23 vehicles are wrongly classified for the case where the vehicles pass close to the sensor and 132 – around 2 times as many as for the correlation classifier – are wrongly classified for vehicles passing far from the sensor.

The incorrect classifications for the two classifiers can be divided into three main sources of error:

1. If multiple vehicles are present at the same time, the single target assumption made in the dipole model (1a) is violated. This situation occurs if two vehicles heading in different directions are passing each other in front of the sensors or if a train of vehicles is passing the sensors with short distance between the vehicles.
2. For large vehicles the dipole model (1a) is also violated. This is because the dipole model does not assume any geometrical extent of the vehicle. Furthermore, for very big vehicles this will give raise to a saturated signal as displayed in Figure 1, which clearly violates the assumption in (1a).
3. Finally, if the SNR is poor the classification result will become worse as also concluded in the simulations in Section 6.

In order to quantify the impact of the first source of error on the two classifiers, the available data was first split into two groups – one group where the vehicles are more than 2 seconds separated from each other and one group where the vehicles are less than 2 seconds separated from each other. Each vehicle gives rise to two data sets since we have two sensors. Therefor in total $511 * 2 = 1,022$ data sets are considered here. The classification results for these two groups are presented in Table 2. According to these results both classifiers are degraded when the single target assumption is violated, however the likelihood test suffers more from this violation than the correlation classifier does.

Furthermore, when the distance between the vehicles is larger than 2 second and the single target assumption applies, the correlation classifier also performs better than the likelihood test. In order to further investigate these differences, this

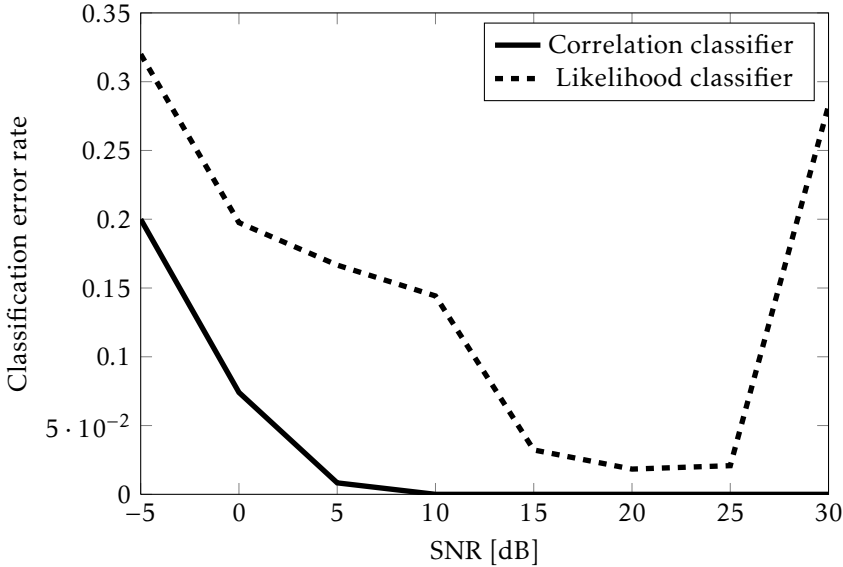


Figure 12: Classification performance compared with the likelihood test as a function of SNR.

group of data has been grouped into 8 classes of different SNR levels, each class having an interval of 5 dB. In Figure 12 the classification result for these groups is presented as a function of the SNR, which was computed as

$$\text{SNR} = 10 \log_{10} \left(\frac{\frac{1}{N} \sum_{k=1}^N \|\bar{\mathbf{h}}_k\|^2}{\sigma^2} \right) \quad [\text{dB}] \approx 10 \log_{10} \left(\frac{\frac{1}{N} \sum_{k=1}^N \|\mathbf{y}_k\|^2 - \sigma^2}{\sigma^2} \right) \quad [\text{dB}],$$

where σ^2 is the variance of the measurement noise.

According to Figure 12 the correlation classifier performs better than the likelihood test for all present SNR levels. Also notice that the correlation classifier has a zero error rate where $\text{SNR} \gtrsim 10$ dB, which the likelihood does not. As a matter of fact, the likelihood test performs even worse for $\text{SNR} \gtrsim 25$ dB corresponding to large vehicles close to the sensor. As explained above, this is because large vehicles violate the point target assumption, which the dipole model (1a) is based upon. However, the correlation classifier is insensitive to these model violations since it does not use that model explicitly, but only one property of it. According to the experimental results, this property is still valid even in a near field scenario since we still have excellent classification results, even for high SNRs.

It is instructive to compare the classification performance evaluated on real data in Figure 12 with the performance on simulated data in Figure 10. When evaluating the classification on simulated data the likelihood classifier performs better than the correlation classifier does. However, for real data the likelihood classifier is heavily disadvantaged such it performs worse than the correlation classifier

due to the reasons discussed above.

Finally, the last two columns in Table 1 show the results for sensor fusion where the classification of both sensors were taken into account. Clearly, the total performance is improved for both classifiers since the total number of correct classifications is larger than for the case when only one sensor was used. Interestingly however, is, that a single sensor performs better for classifying vehicles passing it closely.

7.3 Discussion

As the results in the preceding sections indicate, the proposed driving direction classifier performs very well. The problems encountered and elaborated in the previous section are not specific to the proposed method but rather cases that are challenging for any algorithm. One of the problems was related to scenarios with multiple vehicles in the scene. This violates the single target assumption, which both classifiers are based upon. The likelihood test could be extended to handle this case by modifying the model (4) to include multiple dipoles, which requires even more parameters to estimate. For the proposed correlation classifier such an extension is not possible since the feature has been extracted under the single target assumption and is otherwise not valid. This might be considered as a disadvantage of this classification method. However, in case of multiple targets both classifiers most likely will classify according to the vehicle with the highest SNR.

One approach to improve the results for the likelihood test when multiple vehicles are passing the sensors very closely could be to extend the method as follows. First, one could determine the number of vehicles and then take this information into account when trying to determine the driving direction. Especially for vehicles passing the sensor in different directions at the same time it seems natural that the vehicle causing the stronger magnetic distortion – in most cases the vehicle closer to the sensor – will dominate the signal. Thus, it is very unlikely that such a scenario can be successfully resolved using a single target assumption only.

A disadvantage of the proposed method is the fact that large averaging windows (large p) will cause problems at high speeds (compared to the sampling rate). If a vehicle passes the sensor very fast, only few points of the loop trajectory will be measured. Averaging over these few points will have unwanted effects and it might happen that the estimation becomes wrong. However, note that the correlation classifier behaves better in general since no assumption on the vehicle trajectory and/or speed was made, compared to the likelihood test in Section 3. Clearly, the likelihood test could also be extended to take variations in these parameters into account, however, at a cost of higher complexity.

8 Conclusions

In this paper, a method for fast and efficient classification of the vehicle motion direction using a two-axis magnetometer has been proposed. Its properties were first analyzed theoretically and then verified by using Monte Carlo simulations before it was applied to real measurement data from commercially available sensor. The method was also compared to a generalized likelihood ratio test and it was shown how the method can be extended to incorporate data from multiple independent sensor nodes in a sensor network.

The results show that the performance of the proposed method is very good for vehicles passing on the lane close to the sensor where $> 99\%$ of all vehicles were classified correctly (sample size: 511 vehicles). As it can be expected, performance degrades as the signal-to-noise ratio decreases which reflects in the fact that the classification rate for vehicles on the lane farther from the sensor dropped to approximately 89%. Comparing this method to the generalized likelihood ratio test, it is seen that the latter is outperformed in every aspect. It is very likely that one particular reason for this behavior is the fact that one or more of the assumptions (for example, dipole model, speed, or trajectory) made to derive the GLRT are violated. The biggest difficulties arise in cases where two vehicles meet right in front of the sensor. Apparently, the vehicle generating the stronger field distortion will dominate the signal and the second vehicle is shadowed.

Future work should focus on finding solutions for the cases that are hard to resolve, possibly by fusing information from other sensor types. Furthermore, the implementation in a real sensor platform should be targeted and the performance in a real time system analyzed.

A Distributions

2 Proposition. *Assume the estimator \hat{f}_p given by (31) and the measurement signal \mathbf{y}_k as in (1b) and (1c). Then, the estimator \hat{f}_p is distributed according to*

$$\hat{f}_p \sim \mathcal{N}(f_p, \sigma_{\hat{f}_p}^2) \quad \text{when } N \rightarrow \infty \quad (46)$$

where f_p and $\sigma_{\hat{f}_p}^2$ are given by (32) and (34), respectively.

Proof: As stated above, the mean and variance of \hat{f}_p have been derived in (32) and (34). What remains to show is that \hat{f}_p is normal distributed. Starting by

expanding the original expression for \hat{f}_p yields

$$\begin{aligned}
 \hat{f}_p &= \frac{1}{p} \sum_{k=1}^N (y_k^x y_{k+p}^y - y_k^y y_{k+p}^x) \\
 &= \frac{1}{p} \sum_{k=1}^N (h_k^x + e_k^x)(h_{k+p}^y + e_{k+p}^y) - (h_k^y + e_k^y)(h_{k+p}^x + e_{k+p}^x) \\
 &= \frac{1}{p} \sum_{k=1}^N h_k^x h_{k+p}^y + h_k^x e_{k+p}^y + e_k^x h_{k+p}^y + e_k^x e_{k+p}^y - (h_k^y h_{k+p}^x + h_k^y e_{k+p}^x + e_k^y h_{k+p}^x + e_k^y e_{k+p}^x).
 \end{aligned} \tag{47}$$

Similar to (33)-(34), the sum in (47) can now be rearranged so that all the deterministic coefficients of e_k^α are gathered together:

$$\hat{f}_p = \frac{1}{p} \sum_{k=1}^N h_k^x h_{k+p}^y - h_k^y h_{k+p}^x + (h_{k+p}^y - h_{k-p}^y) e_k^x - (h_{k+p}^x - h_{k-p}^x) e_k^y + e_{k+p}^y e_k^x - e_{k+p}^x e_k^y. \tag{48}$$

Distributing the sum to the individual terms finally gives

$$\begin{aligned}
 \hat{f}_p &= \frac{1}{p} \sum_{k=1}^N (h_k^x h_{k+p}^y - h_k^y h_{k+p}^x) + \frac{1}{p} \sum_{k=1}^N (h_{k+p}^y - h_{k-p}^y) e_k^x \\
 &\quad - \frac{1}{p} \sum_{k=1}^N (h_{k+p}^x - h_{k-p}^x) e_k^y + \frac{1}{p} \sum_{k=1}^N e_{k+p}^y e_k^x - \frac{1}{p} \sum_{k=1}^N e_{k+p}^x e_k^y.
 \end{aligned} \tag{49}$$

Since $\mathbf{e}_k \sim \mathcal{N}(0, \sigma^2 \mathbf{I})$, the second and third term in (49) will also be normal distributed. Furthermore, since all $e_1^x, \dots, e_N^x, e_1^y, \dots, e_N^y$ are independent, the overall variance is simply the sum of the individual variances for each variable and the distributions for these two terms are

$$\mathcal{N}\left(0, \frac{\sigma^2}{p^2} \sum_{k=1}^N (h_{k+p}^y - h_{k-p}^y)^2\right) \quad \text{and} \quad \mathcal{N}\left(0, \frac{\sigma^2}{p^2} \sum_{k=1}^N (h_{k+p}^x - h_{k-p}^x)^2\right). \tag{50a}$$

The last two terms in (49) are sums of normal product distributed variables. The variance for each such variable is

$$\text{Var}(e_{k+p}^y e_k^x) = \text{Var}(e_{k+p}^y) \text{Var}(e_k^x) = \sigma^2 \sigma^2 = \sigma^4 \tag{50b}$$

and since $e_{k+p}^y e_k^x$ are all independent and $\sigma^4 < \infty$, the Central Limit Theorem (see, for example, Billingsley (1995)) yields

$$\frac{1}{p} \sum_{k=1}^N e_{k+p}^y e_k^x \xrightarrow{d} \mathcal{N}\left(0, \frac{N\sigma^4}{p^2}\right) \quad \text{and} \quad \frac{1}{p} \sum_{k=1}^N e_{k+p}^x e_k^y \xrightarrow{d} \mathcal{N}\left(0, \frac{N\sigma^4}{p^2}\right) \tag{50c}$$

as $N \rightarrow \infty$.

Consequently, \hat{f}_p is a sum of one deterministic constant and four zero mean normal distributed variables and since a sum of (possibly dependent) normal distributed variables is also normal distributed we have that

$$\hat{f}_p \sim \mathcal{N}(f_p, \sigma_{\hat{f}_p}^2) \quad \text{when } N \rightarrow \infty. \quad (51)$$

□

B Fusion of Conditional Bernoulli Random Variables

Given multiple conditional PDFs $p(x|y_1), \dots, p(x|y_J)$ it is of interest to find the joint-conditional PDF $p(x|y_1, \dots, y_J)$. Using Bayes rule and assuming that all y_1, \dots, y_J are statistically independent given the true x (conditional independence) yields

$$p(x|y_1, \dots, y_J) = \frac{p(y_1, \dots, y_J|x)p(x)}{p(y_1, \dots, y_J)} = p(x) \frac{\prod_{j=1}^J p(y_j|x)}{p(y_1, \dots, y_J)}$$

and using Bayes' rule on each $p(y_j|x)$ gives

$$\begin{aligned} p(x|y_1, \dots, y_J) &= \frac{p(x)}{p(y_1, \dots, y_J)} \prod_{j=1}^J \frac{p(x|y_j)p(y_j)}{p(x)} \\ &= \frac{\prod_{j=1}^J p(y_j)}{p(x)^{J-1} p(y_1, \dots, y_J)} \prod_{j=1}^J p(x|y_j). \end{aligned}$$

Assuming the uninformative prior $p(x) \propto 1$ yields that $p(x|y_1, \dots, y_J) \propto \prod_{j=1}^J p(x|y_j)$ and thus

$$p(x|\mathbf{y}) = \frac{1}{\eta} \prod_{j=1}^J p(x|y_j) \quad \text{where} \quad \eta = \int_{\mathcal{D}} \prod_{j=1}^J p(x|y_j) dx, \quad (52)$$

with $\mathbf{y} = [y_1 \ y_2 \ \dots \ y_J]^\top$ and η being a normalization constant.

Using (52) for a set of Bernoulli random variables described by the PDF

$$p(k|p_j) = p_j^k (1 - p_j)^{1-k} \quad \text{for } k \in 0, 1, \quad (53)$$

where p_j is the probability of success, the fused PDF becomes

$$p(k|\mathbf{p}) = \frac{\prod_{j=1}^J p_j^k (1 - p_j)^{1-k}}{\prod_{j=1}^J (1 - p_j) + \prod_{j=1}^J p_j}. \quad (54)$$

Bibliography

- P. Billingsley. *Probability and measure*. John Wiley & Sons, 1995.
- Wolfgang Birk, Evgeny Osipov, and Jens Eliasson. iRoad – cooperative road infrastructure systems for driver support. In *16th ITS World Congress 2009, Stockholm Sweden*, September 2009.
- S. Boyd and L. Vandenberghe. *Convex Optimization*. Cambridge University Press, 2004.
- S.-Y. Cheung and P. Varaiya. Traffic surveillance by wireless sensor networks: Final report. Technical report, California Path Program, Institute of Transportation Studies, University of California, Berkeley, 2007.
- J. Chinrungrueng, S. Kaewkamnerd, R. Pongthornseri, S. Dumnin, U. Sunantachaikul, S. Kittipiyakul, S. Samphanyuth, A. Intarapanich, S. Charoenkul, and P. Boonyanant. Wireless sensor network: Application to vehicular traffic. *Advances in Wireless Sensors and Sensor Networks*, pages 199–220, 2010.
- S. Giannecchini, M. Caccamo, and Chi-Sheng Shih. Collaborative resource allocation in wireless sensor networks. In *Proceedings of 16th Euromicro Conference on Real-Time Systems (ECRTS)*, pages 35–44, Catania, Sicily, Italy, June 2004.
- G. Girban and M. Popa. A glance on WSN lifetime and relevant factors for energy consumption. In *Proceedings of the International Joint Conference on Computational Cybernetics and Technical Informatics*, pages 523–528, Timisoara, Romania, May 2010.
- Y. Goyat, T. Chateau, L. Malaterre, and L. Trassoudaine. Vehicle trajectories evaluation by static video sensors. In *Proceedings of the 9th International IEEE Conference on Intelligent Transportation Systems (ITSC)*, pages 864–869, Toronto, Canada, September 2006.
- Honeywell. Vehicle detection using AMR sensors. Technical report, Honeywell International Inc., 2005.
- Honeywell. *2-Axis Magnetic Sensor Circuit HMC6042*, 2007. Datasheet.
- J.D. Jackson. *Classical Electrodynamics*. John Wiley and Sons, Inc., 3 edition, 1998.
- S.M. Kay. *Fundamentals of Statistical Signal Processing: Estimation Theory*. Prentice Hall, 1993. ISBN 0-13-345711-7.
- S.M. Kay. *Fundamentals of Statistical Signal Processing: Detection Theory*. Prentice Hall, 1998.
- K. Kwong, R. Kavalier, R. Rajagopal, and P. Varaiya. Arterial travel time estimation based on vehicle re-identification using wireless magnetic sensors. *Transportation Research Part C: Emerging Technologies*, 17(6):586–606, 2009.

- L.E.Y. Mimbela and L.A. Klein. Summary of vehicle detection and surveillance technologies used in intelligent transportation systems. Technical report, Federal Highway Administration, 2000.
- S. Moler. Stop. You're going the wrong way! *Public Roads*, 66(2), September/October 2002.
- National Highway Traffic Safety Administration. Traffic safety facts 2010: A compilation of motor vehicle crash data from the fatality analysis reporting system and the general estimates system, 2010.
- N.A. Pantazis and D.D. Vergados. A survey on power control issues in wireless sensor networks. *Communications Surveys & Tutorials, IEEE*, 9(4):86–107, 2007.
- M. Pucher, D. Schabus, P. Schallauer, Y. Lypetsky, F. Graf, H. Rainer, M. Stadtschnitzer, S. Sternig, J. Birchbauer, W. Schneider, and B. Schalko. Multimodal highway monitoring for robust incident detection. In *Proceedings of the 13th International IEEE Conference on Intelligent Transportation Systems (ITSC)*, pages 837–842, Madeira Island, Portugal, September 2010.
- William L. Root. An introduction to the theory of the detection of signals in noise. *Proceedings of the IEEE*, 58(5):610–623, May 1970.
- C.C. Sun, G.S. Arr, R.P. Ramachandran, and S.G. Ritchie. Vehicle reidentification using multidetector fusion. *Intelligent Transportation Systems, IEEE Transactions on*, 5(3):155–164, 2004.
- N. Wahlström, J. Callmer, and F. Gustafsson. Magnetometers for tracking metallic targets. In *Proceedings of 13th International Conference on Information Fusion (FUSION)*, Edinburgh, Scotland, July 2010.
- N. Wahlström, R. Hostettler, F. Gustafsson, and W. Birk. Rapid classification of vehicle heading direction with two-axis magnetometer. In *Proceedings of the International Conference on Acoustics, Speech and Signal Processing (ICASSP)*, pages 3385–3388, Kyoto, Japan, March 2012a.
- N. Wahlström, R. Hostettler, F. Gustafsson, and W. Birk. Classification of driving direction in traffic surveillance using magnetometers. *IEEE Transactions on Intelligent Transportation Systems*, 2012b. Submitted.
- W.M. Wynn. Detection, localization, and characterization of static magnetic dipole sources. In *Detection and Identification of Visually Obscured Targets*, pages 337–374. Taylor and Francis, 1999.
- Y. Yu and V.K. Prasanna. Energy-balanced task allocation for collaborative processing in wireless sensor networks. *Mobile Networks and Applications*, 10: 115–131, 2005. ISSN 1383-469X.
- X. Zhang and M.R.B. Forshaw. A parallel algorithm to extract information about the motion of road traffic using image analysis. *Transportation Research Part C: Emerging Technologies*, 5(2):141–152, 1997.

Paper C

Modeling Magnetic Fields using Gaussian Processes

Authors: Niklas Wahlström, Manon Kok, Thomas B. Schön, and Fredrik Gustafsson

Edited version of the paper:

N. Wahlström, M. Kok, T.B. Schön, and F. Gustafsson. Modeling magnetic fields using Gaussian processes. In *Proceedings of the the 38th International Conference on Acoustics, Speech, and Signal Processing (ICASSP)*, Vancouver, Canada, May 2013. Submitted.

Modeling Magnetic Fields using Gaussian Processes

Niklas Wahlström, Manon Kok, Thomas B. Schön, and Fredrik Gustafsson

Dept. of Electrical Engineering,
Linköping University,
SE-581 83 Linköping, Sweden
{nikwa,manko,schon,fredrik}@isy.liu.se

Abstract

Starting from the electromagnetic theory, we derive a Bayesian non-parametric model allowing for joint estimation of the magnetic field and the magnetic sources in complex environments. The model is a Gaussian process which exploits the divergence- and curl-free properties of the magnetic field by combining well-known model components in a novel manner. The model is estimated using magnetometer measurements and spatial information implicitly provided by the sensor. The model and the associated estimator are validated on both simulated and real world experimental data producing Bayesian non-parametric maps of magnetized objects.

1 Introduction

The magnetic field has for a long time been used in navigation for providing seafarers and merchants as well as orienteers and migrating birds with heading information. In indoor environments this navigation task is challenged by the magnetic distortions caused by the ferromagnetic structure in buildings. However, these distortions can also provide position information using a magnetic map of the environment, either by navigating within a precomputed map or by performing simultaneous localization and mapping (SLAM). This requires good models of the magnetic field which will be investigated more deeply in this work by addressing the electromagnetic theory. The relation between the magnetic sources and their induced magnetic field is well understood and was already formulated by Maxwell (1865), see also Jackson (1998). However, little work has been done incorporating this knowledge into a statistical framework suitable for estimating magnetic fields in complex magnetic environments based on noisy data. We present a Bayesian nonparametric model (a particular Gaussian process) capable of modeling the magnetic field as well as the magnetic sources, see Figure 3. Our model exploits the divergence- and curl-free properties of the magnetic field inherited by the electromagnetic theory.

Gaussian processes (Rasmussen and Williams, 2006) have previously been used for modeling magnetic fields in an indoor environment to enable SLAM (Vallivaara et al., 2010, 2011). Their navigation platform is equipped with a three axis magnetometer and the positioning is aided with odometry. However, in contrast to our work, the model of the magnetic map does not incorporate knowledge from Maxwell's equations and is not able to estimate the location of the magnetic sources. The same model has been investigated further by Kempainen et al. (2011). Gaussian processes have recently also been used for SLAM in a scalar potential field (Murphy and Godsill, 2012). However, we consider multiple vector fields rather than one scalar potential field in this work. Vissière et al. (2007) also use the magnetic disturbances to improve IMU-based position estimation. That work uses the restrictions induced by the electromagnetic theory, but does not construct any magnetic map and does not localize the magnetic sources. (Chung et al., 2011) uses only four tilt-compensated magnetometers to accomplish indoor localization. The magnetic map is captured in advance consisting of a collection of magnetic signatures. The localization is performed using magnetic map fingerprints, where the performance is enhanced by the multiplicity of the magnetometers. Also fusion of magnetic field anomalies and laser has been investigated (Zhang and Martin, 2011).

This work only addresses the modeling aspects of the magnetic field and the magnetic sources. The localization problem we consider separately (Kok et al., 2013), but the model is also suitable for being used in the applications presented above. The contributions of this work are:

- A Gaussian process model which in a novel manner exploits the divergence- and curl-free properties of the magnetic field.
- The model enables the magnetic field and the magnetic sources to be estimated jointly.
- Interference with both magnetic field measurements and spatial information is possible.
- We validate the model using both simulations and real world experimental data.

The divergence- and curl-free properties of a vector field have previously been used for estimating fluid flows using Gaussian processes (Macêdo and Castro, 2008). However, to the best authors' knowledge this has previously not been used in modeling magnetic fields.

2 Magnetic Fields

A magnetic field is a mathematical construction used for describing forces induced by magnetic materials and electric currents. For each point in space the magnetic field can be described using a vector and as such it is a vector field. There are two different, but closely related ways to describe the magnetic field,

denoted with the symbols \mathbf{B} and \mathbf{H} , where boldface denotes vector-valued quantities.

These fields can not be any two arbitrary vector fields, but need to obey physical laws, which in their most general form are known as Maxwell's equations (Jackson, 1998). By assuming absence of free currents and time-dependent effects, these equations will reduce to

$$\nabla \cdot \mathbf{B} = 0, \quad (1a)$$

$$\nabla \times \mathbf{H} = \mathbf{0}, \quad (1b)$$

which means that the \mathbf{B} -field is divergence-free and the \mathbf{H} -field is curl-free. Further, these two fields are coupled as

$$\mathbf{M} = \frac{1}{\mu_0} \mathbf{B} - \mathbf{H}, \quad (2)$$

where \mathbf{M} is the magnetization describing our magnetic environment and μ_0 is the vacuum permeability, which is a physical constant having the value $\mu_0 = 4\pi \times 10^{-7} \text{Vs A}^{-1} \text{m}^{-1}$. These fields will be illustrated with the following example. More details on the derivation can be found in Jackson (1998).

1 Example: Uniformly magnetized sphere

Consider a sphere with a uniform permanent magnetization as depicted in Figure 1c. By solving (1) and (2) for this special geometry we will end up in a dipole field outside the sphere as depicted in Figure 1a and 1b. Note that the \mathbf{B} - and the \mathbf{H} -field will be identical (up to the proportional constant μ_0) outside the sphere, which follows directly from (2) using $\mathbf{M} = \mathbf{0}$. However, inside the sphere the \mathbf{B} - and the \mathbf{H} -field will be aligned in opposite directions in order to ensure that the \mathbf{B} -field is divergence-free (no sources or sinks) and that the \mathbf{H} -field is curl-free (no swirls).

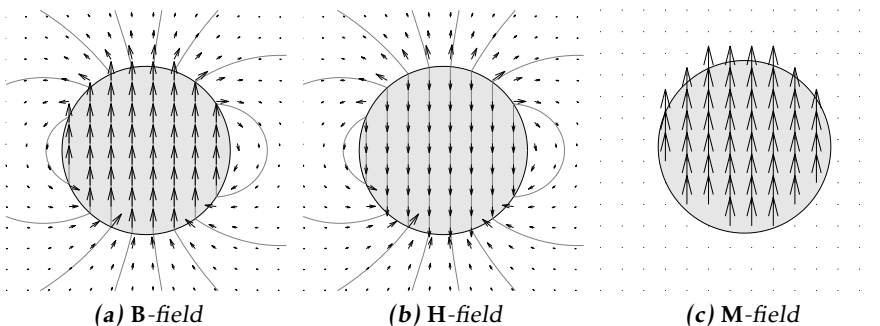


Figure 1: The \mathbf{B} -, \mathbf{H} - and \mathbf{M} -field of a uniformly magnetized sphere. The \mathbf{B} -field is here normalized with μ_0 .

By using (1)-(2) and prior knowledge of the magnetic environment, a number

of things can be concluded, which will be used in Section 4 when modeling the magnetic fields:

1. **Additional information** In all non-magnetic materials the magnetization is equal to zero, $\mathbf{M} = \mathbf{0}$. This is especially true in locations where we measure the magnetic field, since air is non-magnetic. Due to physical constraints the sensor cannot be inside a magnetic material and we know that $\mathbf{M} = \mathbf{0}$ at these positions. This additional information will be used in our framework as an extra measurement. Sensor fusion with other sensors such as camera and laser range sensor, providing even richer information of where $\mathbf{M} = \mathbf{0}$, is possible. However, this is not considered in this work.
2. **External field** Most environments of interest consist of an external homogeneous field \mathbf{B}_0 or \mathbf{H}_0 , usually the earth magnetic field or a slight deformation of it. Due to the linearity of the field equations (1), this external field can be superimposed throughout all space, where (2) gives the relation $\mathbf{B}_0 = \mu_0 \mathbf{H}_0$. We will therefore later model the \mathbf{B} - and the \mathbf{H} -field to have a common, but unknown mean.
3. **Smoothness** If $\mathbf{M}(\mathbf{u}) = \mathbf{0}$ in a neighborhood of \mathbf{u} , the field equations (1) will ensure that \mathbf{B} and \mathbf{H} are infinitely continuously differentiable at \mathbf{u} . This gives the magnetic field a "smooth" character and the magnetic field at \mathbf{u}_1 will be very similar to the magnetic field at \mathbf{u}_2 if \mathbf{u}_1 and \mathbf{u}_2 are close. This property motivates us to employ Gaussian processes in modeling these fields, as will be explained in the next section.

3 Gaussian Processes

A Gaussian process (GP) (Rasmussen and Williams, 2006) is a stochastic process suitable for modeling spatially correlated measurements. GPs can be seen as a distribution over functions

$$\mathbf{f}(\mathbf{u}) \sim \mathcal{GP}(\boldsymbol{\mu}(\mathbf{u}), \mathbf{K}(\mathbf{u}, \mathbf{u}')), \quad (3)$$

where the process is uniquely defined with its mean function $\boldsymbol{\mu}(\mathbf{u})$ and covariance function $\mathbf{K}(\mathbf{u}, \mathbf{u}')$.

The GP is a generalization of the multivariate Gaussian probability distribution in the sense that the function values evaluated for a finite number of inputs $\mathbf{u}_1, \dots, \mathbf{u}_N$ are normally distributed

$$\begin{bmatrix} \mathbf{f}(\mathbf{u}_1) \\ \vdots \\ \mathbf{f}(\mathbf{u}_N) \end{bmatrix} \sim \mathcal{N}(\boldsymbol{\mu}, \mathbf{K}), \quad \text{where } \boldsymbol{\mu} = \begin{bmatrix} \boldsymbol{\mu}(\mathbf{u}_1) \\ \vdots \\ \boldsymbol{\mu}(\mathbf{u}_N) \end{bmatrix}, \quad \mathbf{K} = \begin{bmatrix} \mathbf{K}(\mathbf{u}_1, \mathbf{u}_1) & \cdots & \mathbf{K}(\mathbf{u}_1, \mathbf{u}_N) \\ \vdots & & \vdots \\ \mathbf{K}(\mathbf{u}_N, \mathbf{u}_1) & \cdots & \mathbf{K}(\mathbf{u}_N, \mathbf{u}_N) \end{bmatrix}. \quad (4a)$$

3.1 Mean Function

In this work we will consider a constant, but unknown mean function $\boldsymbol{\mu}(\mathbf{u}) = \boldsymbol{\beta}$, where we put a Gaussian prior on the mean

$$\mathbf{f}(\mathbf{u}) \sim \mathcal{GP}(\boldsymbol{\beta}, \mathbf{K}(\mathbf{u}, \mathbf{u}')), \quad \text{where } \boldsymbol{\beta} \sim \mathcal{N}(\mathbf{0}, \sigma_{\beta}^2 \mathbf{I}). \quad (5a)$$

By integrating out the parameter $\boldsymbol{\beta}$, this can be reformulated as a zero mean GP

$$\mathbf{f}(\mathbf{u}) \sim \mathcal{GP}(\mathbf{0}, \mathbf{K}(\mathbf{u}, \mathbf{u}') + \sigma_{\beta}^2 \mathbf{I}). \quad (5b)$$

3.2 Vector-Valued Covariance Functions

The covariance function (a.k.a. kernel) is the crucial component when modeling using a GP. This function encodes the assumptions we make on the functions to be learned. For modeling smooth functions (as desired in Item 3 in Section 2) with scalar output the most common choice is the squared exponential (SE) covariance function

$$\mathbf{K}(\mathbf{u}, \mathbf{u}') = k(\mathbf{u}, \mathbf{u}') = \sigma_f^2 e^{-\frac{\|\mathbf{u}-\mathbf{u}'\|^2}{2l^2}}, \quad (6)$$

where σ_f is the expected amplitude and l the expected length-scale of the function we want to learn. This covariance function can be extended for learning functions with multiple outputs as presented below. Learning functions with multiple outputs has recently attracted more attention. A review can be found in Álvarez et al. (2012), which discusses different kernels for learning vector-valued functions.

Diagonal Squared Exponential Covariance Function

The most obvious extension of (6) to multiple outputs is to model each component $f_i(\mathbf{u})$ separately using a scalar SE covariance functions resulting in a diagonal SE kernel

$$\mathbf{K}(\mathbf{u}, \mathbf{u}') = \sigma_f^2 e^{-\frac{\|\mathbf{u}-\mathbf{u}'\|^2}{2l^2}} \cdot \mathbf{I}_{n_y}, \quad (7)$$

where n_y is the dimension of the output. The kernel (7) can be extended to have different hyperparameters l and σ_f for each output dimension. This kernel was used by Vallivaara et al. (2010) and Vallivaara et al. (2011) in modeling the magnetic field of an indoor environment. However, this kernel does not allow for the possibility of modeling correlations between the different components $f_i(\mathbf{u})$. Specially, it does not produce functions which necessarily obey the field equations (1). This is made possible by the two covariance functions introduced below.

Divergence- and Curl-Free Covariance Functions

A kernel for learning divergence-free vector fields was first introduced by Narcowich and Ward (1994). Based on the scalar SE kernel (6), this kernel reads

$$\mathbf{K}_{\mathbf{B}}(\mathbf{u}, \mathbf{u}') = \sigma_f^2 e^{-\frac{\|\mathbf{u}-\mathbf{u}'\|^2}{2l^2}} \cdot \left(\left(\frac{\mathbf{u}-\mathbf{u}'}{l} \right) \left(\frac{\mathbf{u}-\mathbf{u}'}{l} \right)^{\top} + \left(n_y - 1 - \frac{\|\mathbf{u}-\mathbf{u}'\|^2}{l^2} \right) \mathbf{I}_{n_y} \right) \quad (8)$$

which ensures that all functions sampled from a GP with such a kernel will be divergence-free. Similarly, Fuselier Jr (2006) introduced a kernel for learning curl-free vector fields, where the extension of (6) reads

$$K_{\mathbf{H}}(\mathbf{u}, \mathbf{u}') = \sigma_f^2 e^{-\frac{\|\mathbf{u}-\mathbf{u}'\|^2}{2l^2}} \left(\mathbf{I}_{n_y} - \left(\frac{\mathbf{u}-\mathbf{u}'}{l} \right) \left(\frac{\mathbf{u}-\mathbf{u}'}{l} \right)^\top \right). \quad (9)$$

The interested reader can refer to Fuselier Jr (2006); Macêdo and Castro (2008); Baldassarre et al. (2010) for more analysis and discussion on these two kernels.

3.3 Regression

GPs are also capable of handling noisy measurements \mathbf{y}_k of the function $\mathbf{f}(\mathbf{u}_k)$. We consider the measurement model

$$\mathbf{y}_k = \mathbf{f}(\mathbf{u}_k) + \mathbf{e}_k, \quad \mathbf{e}_k \sim \mathcal{N}(\mathbf{0}, \Sigma), \quad (10)$$

where \mathbf{e}_k has the interpretation of being measurement noise. Our objective is to use a set of measurements together with their corresponding inputs $\{\mathbf{u}_k, \mathbf{y}_k | k = 1, \dots, N\}$ to learn the function values for other test inputs $\mathbf{f}_* = [\mathbf{f}(\mathbf{u}_1^*)^\top \dots \mathbf{f}(\mathbf{u}_{N_*}^*)^\top]^\top$. In the same manner as in (4) the joint distribution for the measurements $\mathbf{y} = [\mathbf{y}_1^\top \dots \mathbf{y}_N^\top]^\top$ and the test output \mathbf{f}_* is

$$\begin{bmatrix} \mathbf{y} \\ \mathbf{f}_* \end{bmatrix} \sim \mathcal{N} \left(\mathbf{0}, \begin{bmatrix} \mathbf{K}(\mathbf{U}, \mathbf{U}) + \mathbf{I}_N \otimes \Sigma & \mathbf{K}(\mathbf{U}, \mathbf{U}_*) \\ \mathbf{K}(\mathbf{U}_*, \mathbf{U}) & \mathbf{K}(\mathbf{U}_*, \mathbf{U}_*) \end{bmatrix} \right), \quad (11)$$

where \otimes denote the Kronecker product,

$$\mathbf{K}(\mathbf{U}, \mathbf{U}_*) = \begin{bmatrix} \mathbf{K}(\mathbf{u}_1, \mathbf{u}_1^*) & \dots & \mathbf{K}(\mathbf{u}_1, \mathbf{u}_{N_*}^*) \\ \vdots & & \vdots \\ \mathbf{K}(\mathbf{u}_N, \mathbf{u}_1^*) & \dots & \mathbf{K}(\mathbf{u}_N, \mathbf{u}_{N_*}^*) \end{bmatrix} \quad (12)$$

and similarly for the other matrices $\mathbf{K}(\mathbf{U}, \mathbf{U})$, $\mathbf{K}(\mathbf{U}_*, \mathbf{U})$ and $\mathbf{K}(\mathbf{U}_*, \mathbf{U}_*)$. From the joint Gaussian distribution $p(\mathbf{y}, \mathbf{f}_*)$ in (11) the conditional distribution $p(\mathbf{f}_* | \mathbf{y})$ can easily be computed as

$$\mathbf{f}_* | \mathbf{y} \sim \mathcal{N}(\boldsymbol{\mu}_{\mathbf{f}_*}, \Sigma_{\mathbf{f}_*}), \quad (13a)$$

$$\boldsymbol{\mu}_{\mathbf{f}_*} = \mathbf{K}_*^\top \mathbf{K}_y^{-1} \mathbf{y}, \quad \Sigma_{\mathbf{f}_*} = \mathbf{K}_{**} - \mathbf{K}_*^\top \mathbf{K}_y^{-1} \mathbf{K}_*, \quad (13b)$$

where $\mathbf{K} = \mathbf{K}(\mathbf{U}, \mathbf{U})$, $\mathbf{K}_* = \mathbf{K}(\mathbf{U}, \mathbf{U}_*)$, $\mathbf{K}_{**} = \mathbf{K}(\mathbf{U}_*, \mathbf{U}_*)$ and $\mathbf{K}_y = \mathbf{K}(\mathbf{U}, \mathbf{U}) + \mathbf{I}_N \otimes \Sigma$.

3.4 Estimating Hyperparameters

The hyperparameters of the covariance function $\mathbf{K}(\mathbf{u}, \mathbf{u}')$ and the measurement noise covariance matrix Σ can be estimated from the data $\{\mathbf{u}_k, \mathbf{y}_k | k = 1, \dots, N, \}$, which makes the learning of the function values \mathbf{f}_* completely data driven in the sense that no tuning parameters are needed. This will be accomplished by maximizing the log marginal likelihood $\log p(\mathbf{y}, | \mathbf{U}, \boldsymbol{\theta})$, where $\boldsymbol{\theta}$ denote the hyperparameters of $\mathbf{K}(\mathbf{u}, \mathbf{u}')$ and Σ . From (11) we have that $\mathbf{y} | \mathbf{U}, \boldsymbol{\theta} \sim \mathcal{N}(\mathbf{0}, \mathbf{K}_y)$, which

gives

$$\log p(\mathbf{y}|\mathbf{U}, \boldsymbol{\theta}) = -\frac{1}{2}\mathbf{y}^\top \mathbf{K}_y^{-1} \mathbf{y} - \frac{1}{2} \log |\mathbf{K}_y| - \frac{n_y N}{2} \log 2\pi. \quad (14)$$

Following Rasmussen and Williams (2006), the gradient of the log marginal likelihood w.r.t. the hyperparameters can be computed as

$$\frac{\partial}{\partial \theta_j} \log p(\mathbf{y}|\mathbf{U}, \boldsymbol{\theta}) = \frac{1}{2} \text{tr} \left((\boldsymbol{\alpha} \boldsymbol{\alpha}^\top - \mathbf{K}_y^{-1}) \frac{\partial \mathbf{K}_y}{\partial \theta_j} \right), \quad (15)$$

where $\boldsymbol{\alpha} = \mathbf{K}_y^{-1} \mathbf{y}$. This enables an efficient gradient based optimizing routine for maximizing (14). In this work the BFGS method (Nocedal and Wright, 1999) has been used.

4 Modeling

The GP framework will now be combined with the electromagnetic theory to construct a model for jointly estimating the \mathbf{B} - and the \mathbf{M} -field using a three-axis magnetometer. We assume that the measurements of the magnetic field are corrupted with Gaussian noise

$$\mathbf{y}_{\mathbf{B},k} = \mathbf{f}_{\mathbf{B}}(\mathbf{u}_k) + \mathbf{e}_{\mathbf{B},k}, \quad \mathbf{e}_{\mathbf{B},k} \sim \mathcal{N}(\mathbf{0}, \sigma_n^2 \mathbf{I}_3), \quad (16a)$$

where $\mathbf{y}_{\mathbf{B},k}$ is a three-axis magnetometer measurement transformed into world coordinates and $\mathbf{f}_{\mathbf{B}}(\mathbf{u}_k)$ is a function being equal to the \mathbf{B}/μ_0 -field (the \mathbf{B} -field normalized with μ_0) at location \mathbf{u}_k . As discussed in Item 1 in Section 2 we also know that the \mathbf{M} -field is zero at location \mathbf{u}_k , where the measurement $\mathbf{y}_{\mathbf{B},k}$ was collected. This information is incorporated by considering a noise free measurement $\mathbf{y}_{\mathbf{M},k} = \mathbf{0}$ with the following measurement equation

$$\mathbf{y}_{k,\mathbf{M}} = \mathbf{f}_{\mathbf{M}}(\mathbf{u}_k) = \mathbf{f}_{\mathbf{B}}(\mathbf{u}_k) - \mathbf{f}_{\mathbf{H}}(\mathbf{u}_k), \quad (16b)$$

where $\mathbf{f}_{\mathbf{M}}(\mathbf{u}_k)$ and $\mathbf{f}_{\mathbf{H}}(\mathbf{u}_k)$ are functions corresponding to the \mathbf{M} - and the \mathbf{H} -field and where we have used the coupling given by (2). Note that this coupling is the key equation for our model since it enables us to jointly estimate the \mathbf{B} -field as well as the \mathbf{M} -field in contrast to prior work.

We put this into a statistical framework by considering $\mathbf{f}_{\mathbf{B}}$ and $\mathbf{f}_{\mathbf{H}}$ (and consequently also $\mathbf{f}_{\mathbf{M}}$ via (16b)) to be GPs. Following the discussion in Item 2 in Section 2 we consider $\mathbf{f}_{\mathbf{B}}$ and $\mathbf{f}_{\mathbf{H}}$ to have a common constant mean function (corresponding to the earth magnetic field) and we use the covariance functions given in (8) and (9) to preserve the divergence- and curl-free properties of $\mathbf{f}_{\mathbf{B}}$ and $\mathbf{f}_{\mathbf{H}}$ according to the field equations (1). This gives

$$\mathbf{f}_{\mathbf{B}} \sim \mathcal{GP}(\boldsymbol{\beta}, \mathbf{K}_{\mathbf{B}}(\mathbf{u}, \mathbf{u}')), \quad \mathbf{f}_{\mathbf{H}} \sim \mathcal{GP}(\boldsymbol{\beta}, \mathbf{K}_{\mathbf{H}}(\mathbf{u}, \mathbf{u}')), \quad (16c)$$

$$\boldsymbol{\beta} \sim \mathcal{N}(\mathbf{0}, \sigma_\beta^2 \mathbf{I}_3), \quad (16d)$$

where we have used a Gaussian prior on the unknown mean $\boldsymbol{\beta}$.

The model (16) can be reformulated into the standard model description outlined in Section 3

$$\mathbf{y}_k = \mathbf{f}(\mathbf{u}_k) + \mathbf{e}_k, \quad (17a)$$

$$\mathbf{f}(\mathbf{u}) \sim \mathcal{GP}(\mathbf{0}, \mathbf{K}(\mathbf{u}, \mathbf{u}')), \quad \mathbf{e}_k \sim \mathcal{N}(\mathbf{0}, \Sigma), \quad (17b)$$

by augmenting the measurements and the noise covariance matrices

$$\mathbf{y}_k = \begin{bmatrix} \mathbf{y}_{\mathbf{B},k} \\ \mathbf{y}_{\mathbf{M},k} \end{bmatrix} \quad \text{and} \quad \Sigma = \begin{bmatrix} \sigma_n^2 \mathbf{I}_3 & \mathbf{0}_3 \\ \mathbf{0}_3 & \mathbf{0}_3 \end{bmatrix} \quad (17c)$$

as well as the outputs of the functions that we want to learn

$$\mathbf{f}(\mathbf{u}) = \begin{bmatrix} \mathbf{f}_{\mathbf{B}}(\mathbf{u}) \\ \mathbf{f}_{\mathbf{M}}(\mathbf{u}) \end{bmatrix} = \begin{bmatrix} \mathbf{I}_3 & \mathbf{0}_3 \\ \mathbf{I}_3 & -\mathbf{I}_3 \end{bmatrix} \begin{bmatrix} \mathbf{f}_{\mathbf{B}}(\mathbf{u}) \\ \mathbf{f}_{\mathbf{H}}(\mathbf{u}) \end{bmatrix} \sim \mathcal{GP}(\mathbf{0}, \mathbf{K}), \quad (17d)$$

where $\mathbf{K} = \mathbf{K}(\mathbf{u}, \mathbf{u}')$. The augmented function $\mathbf{f} : \mathbb{R}^3 \rightarrow \mathbb{R}^6$ will then have the covariance function

$$\mathbf{K} = \begin{bmatrix} \mathbf{K}_{\mathbf{B}} + \sigma_{\beta}^2 \mathbf{I}_3 & \mathbf{K}_{\mathbf{B}} \\ \mathbf{K}_{\mathbf{B}} & \mathbf{K}_{\mathbf{B}} + \mathbf{K}_{\mathbf{H}} \end{bmatrix}, \quad (17e)$$

where the relation $\mathbf{f}(\mathbf{u}) \sim \mathcal{GP}(\mathbf{0}, \mathbf{K}) \Rightarrow \mathbf{Cf}(\mathbf{u}) \sim \mathcal{GP}(\mathbf{0}, \mathbf{CKC}^T)$ has been used as well as (5) to reformulate this as a zero mean GP. Finally, we encode

$\theta \triangleq [\log \sigma_f^2 \log l^2 \log \sigma_{\beta}^2 \log \sigma_n^2]$, where the logarithm ensures the positiveness of σ_f^2 , l^2 , σ_{β}^2 and σ_n^2 .

5 Results

The ability of the proposed model to model magnetic fields will be evaluated by using a simulated data set as well as a real world data set. The results will be reported in this section.

5.1 Simulated Experiment

The setup with a uniformly magnetized sphere presented in Example 1 is used to estimate the \mathbf{B} -, \mathbf{H} - and \mathbf{M} -field given in Figure 1. Consider a sphere centered at the origin with radius 3 m having a uniform magnetization of $\mathbf{M} = [0 \ 1 \ 0]^T \text{ A m}^{-1}$. In total $N = 50$ training inputs are chosen from a region outside the sphere and inside a square with dimension 10 m \times 10 m aligned with the xy -plane, which also is centered at the origin. For each training input the corresponding training output is computed using the true field perturbed with Gaussian noise having a standard deviation of $\sigma_n = 0.01$. The test inputs are chosen from a grid xy -plane with an interval of 0.75 m. The estimated magnetic field at these test inputs is then compared with the true magnetic fields. Both the SE kernel (7) and the proposed kernel (17) are applied to the data, where the hyperparameters for each kernel are estimated as described in Section 3.4. The results are given in Figure 2.

Both the SE kernel and the proposed kernel (17) are able to reproduce the character of the true \mathbf{B} -field as given in Figure 1a. By comparing the estimated \mathbf{B} -field with the true \mathbf{B} -field, the proposed covariance function is only slightly better with a root mean square error of 0.33 A m^{-1} , whereas the corresponding number for the SE covariance function is 0.38 A m^{-1} . However, the great advantage with the proposed covariance function is its ability to estimate the \mathbf{M} -field as shown in Figure 2c, which resembles the true \mathbf{M} -field in Figure 1c. Both the location of the magnetic source and the direction of its magnetization are correctly captured.

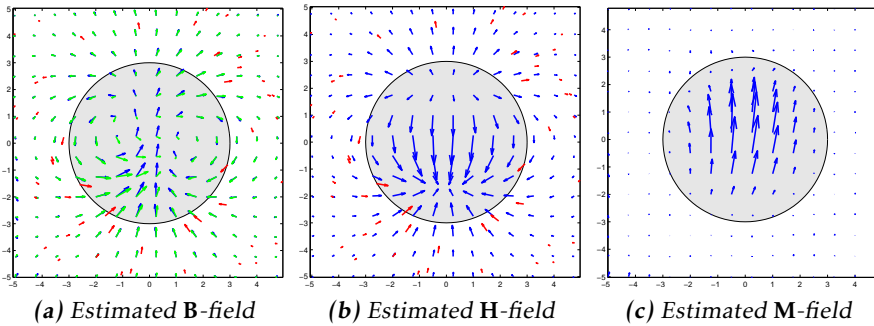


Figure 2: Estimated fields induced by a uniformly magnetized sphere (see Example 1) using our proposed kernel (17) (blue) and the SE kernel (6) (green) together with the training data (red).

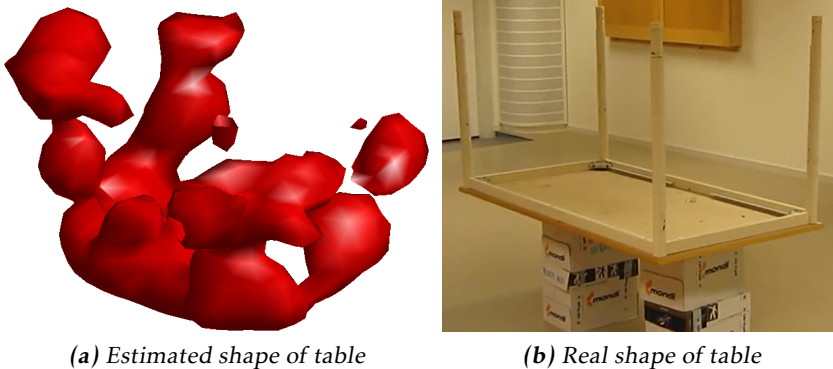


Figure 3: Estimated magnetic content in a table turned upside down.

5.2 Real World Experiment

A real world experiment was conducted in a magnetic environment consisting of a table with metal frame turned upside down as displayed in Figure 3b. A three axis magnetometer has been used to measure the magnetic field at various locations around that table and the position and the orientation of the magnetometer unit was measured using an optical reference system (Vicon). The magnetometer measurements were then transformed into world coordinates using the orientation provided by the reference. This data has been downsampled to 2 Hz to reduce the number of data points. Together with the position estimate from the reference this comprises the training data as displayed in Figure 4. For this dataset the hyperparameters have not been estimated but rather tuned to $\sigma_f = 0.3$, $l = 0.15$, $\sigma_b = 1$ and $\sigma_n = 0.3$ for reasons discussed below. In Figure 3a the region of the \mathbf{M} -field which exceeds 30% of the maximal estimated \mathbf{M} -field is displayed. This estimated magnetic map has visual similarities with the real table in Figure 3b. All four table legs can be distinguished as well as the frame on which the table top is attached.

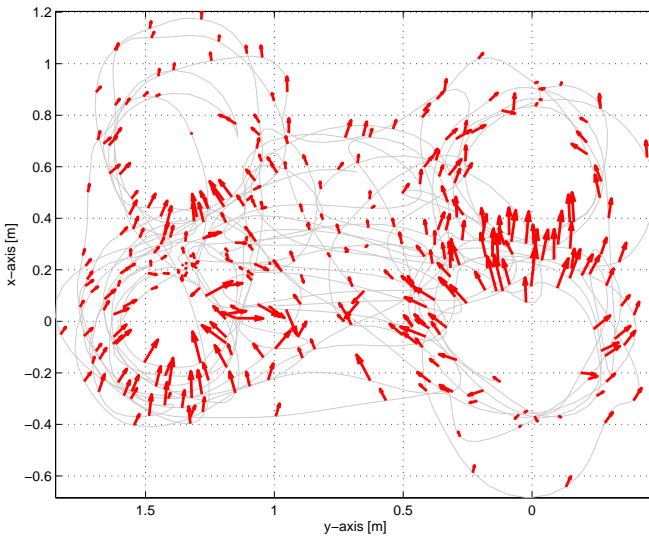


Figure 4: The training data in the real world experiment seen from above together with the trajectory that the magnetometer has followed.

The proposed GP (as any other stationary GP) is restricted to using the same set of hyperparameters for all data. This is problematic in environments which have different characteristic length scales and signal amplitudes in different regions in space. When estimating the hyperparameters in the proposed manner using data collected in such environments, the result might not be sound. The hyperparameters have therefore been considered as tuning parameters.

6 Conclusion and Future Work

We have introduced a Bayesian nonparametric model for jointly estimating both the magnetic field and the magnetic sources. The model is based on a vector-valued stationary Gaussian process (GP) with a covariance function exploiting the divergence- and curl-free properties of the magnetic field derived from the electromagnetic theory. The model has been compared with a component-wise GP proposed by Vallivaara et al. (2010) for modeling magnetic fields. In the comparison only a small improvement in estimation performance could be reported. However, the great advantage of the proposed method is its ability to also model the magnetic sources in a nonparametric manner, which has been illustrated using both simulated and real world data.

In future work we will extend our nonparametric model to handle more complex environments. One promising idea is to use a multiplicity of GPs governed by a hierarchical Dirichlet process (Teh et al., 2006). Our final target is a full SLAM framework.

Bibliography

- M. A. Álvarez, L. Rosasco, and N.D. Lawrence. Kernels for vector-valued functions: A review. *Found. Trends Mach. Learn.*, 4(3):195–266, March 2012. ISSN 1935-8237.
- L. Baldassarre, L. Rosasco, A. Barla, and A. Verri. Vector field learning via spectral filtering. *Machine Learning and Knowledge Discovery in Databases*, pages 56–71, 2010.
- J. Chung, M. Donahoe, C. Schmandt, I.J. Kim, P. Razavai, and M. Wiseman. Indoor location sensing using geo-magnetism. In *Proceedings of the 9th International Conference on Mobile systems, Applications, and Services*, pages 141–154, Bethesda, USA, June 2011.
- E.J. Fuselier Jr. *Refined error estimates for matrix-valued radial basis functions*. PhD thesis, Texas A&M University, 2006.
- J.D. Jackson. *Classical Electrodynamics*. John Wiley & Sons, Inc, 3rd edition, 1998.
- A. Kemppainen, J. Haverinen, I. Vallivaara, and J. Röning. Near-optimal Exploration in Gaussian Process SLAM: Scalable Optimality Factor and Model Quality Rating. In *Proceedings of European Conference on Mobile Robots*, pages 283–290, Örebro, Sweden, September 2011.
- M. Kok, N. Wahlström, T.B. Schön, and F. Gustafsson. MEMS-based inertial navigation based on a magnetic field map. In *Proceedings of the 38th International Conference on Acoustics, Speech, and Signal Processing (ICASSP)*, Vancouver, Canada, May 2013. Submitted.
- I. Macêdo and R. Castro. Learning divergence-free and curl-free vector fields with matrix-valued kernels. Technical report, Technical report, Instituto Nacional de Matematica Pura e Aplicada, 2008.
- J.C. Maxwell. A dynamical theory of the electromagnetic field. *Philosophical Transactions of the Royal Society of London*, 155:459–512, 1865.
- J. Murphy and S. Godsill. Simultaneous localization and mapping for non-parametric potential field environments. In *Proceedings of the 15th International Conference on Information Fusion*, Singapore, July 2012.
- E.J. Narcowich and J.D. Ward. Generalized hermite interpolation via matrix-valued conditionally positive definite functions. *Mathematics of Computation*, 63(208):661–688, 1994.
- J. Nocedal and S.J. Wright. *Numerical optimization*. Springer verlag, 1999.
- C.E. Rasmussen and C.K.I. Williams. *Gaussian processes for machine learning*. MIT press Cambridge, MA, 2006.

- Y.W. Teh, M.I. Jordan, M.J. Beal, and D.M. Blei. Hierarchical Dirichlet processes. *Journal of the American Statistical Association*, 101(476):1566–1581, 2006.
- I. Vallivaara, J. Haverinen, A. Kemppainen, and J. Roning. Simultaneous localization and mapping using ambient magnetic field. In *Proceedings of the IEEE Conference on Multisensor Fusion and Integration for Intelligent Systems (MFI)*, pages 14–19, Salt Lake City, USA, September 2010.
- I. Vallivaara, J. Haverinen, A. Kemppainen, and J. Roning. Magnetic field-based SLAM method for solving the localization problem in mobile robot floor-cleaning task. In *Proceedings of the 15th International Conference on Advanced Robotics (ICAR)*, pages 198–203, Tallin, Estonia, June 2011.
- D. Vissière, A.P. Martin, and N. Petit. Using magnetic disturbances to improve IMU-based position estimation. In *Proceedings of the European Control Conference*, pages 2853–2858, Kos, Greece, July 2007.
- N. Wahlström, M. Kok, T.B. Schön, and F. Gustafsson. Modeling magnetic fields using Gaussian processes. In *Proceedings of the the 38th International Conference on Acoustics, Speech, and Signal Processing (ICASSP)*, Vancouver, Canada, May 2013. Submitted.
- H. Zhang and F. Martin. Robotic mapping assisted by local magnetic field anomalies. In *Proceedings of the IEEE Conference on Technologies for Practical Robot Applications (TePRA)*, pages 25–30, Woburn, USA, April 2011.

Paper D

A Voyage to Africa by Mr Swift

Authors: Niklas Wahlström, Fredrik Gustafsson and Susanne Åkesson

Edited version of the paper:

N. Wahlström, F. Gustafsson, and S. Åkesson. A Voyage to Africa by Mr Swift. In *Proceedings of the 15th International Conference on Information Fusion (FUSION)*, pages 808–815, Singapore, July 2012a.

A Voyage to Africa by Mr Swift

Niklas Wahlström*, Fredrik Gustafsson* and Susanne Åkesson **

*Dept. of Electrical Engineering,
Linköping University,
SE-581 83 Linköping, Sweden
{nikwa, fredrik}@isy.liu.se

**Department of Biology
Centre for Animal Movement Research
Lund University,
SE-221 00 Lund, Sweden
susanne.akesson@biol.lu.se

Abstract

A male common swift *Apus apus* was equipped with a light logger on August 5, 2010, and again captured in his nest 298 days later. The data stored in the light logger enables analysis of the fascinating travel he made in this time period.

The state of the art algorithm for geolocation based on light loggers consists in computing first sunrise and sunset from the logged data, which are then converted to midday (gives longitude) and day length (gives latitude). This approach has singularities at the spring and fall equinoxes, and gives a bias for fast day transitions in the east-west direction.

We derive a flexible particle filter solution, where sunset and sunrise are processed separately in two different measurement updates, and where the motion model has two modes, one for migration and one for stationary long time visits, which are designed to fit the flying pattern of the swift. This approach circumvents the aforementioned problems with singularity and bias, and provides realistic confidence bounds on the geolocation as well as an estimate of the migration mode.

1 Introduction

Geolocation for learning migration behavior of animals is an important area for ecologists and epidemiologists. With an ever lasting improvement in sensor technology and miniaturization of electronics, more and smaller species can be studied. More specifically, researchers are no longer limited to satellite based geolocation, which requires substantial battery capacity and in practice also radio transmitters to communicate the geolocation data, which in turn requires even more battery with the consequence that only larger birds can be studied. One such enabling technology is light loggers permitting documentation of migration by individual small songbirds, waders and swifts, which so far is not extensively studied. Commercial versions include a light sensor, a battery, a memory and a



Figure 1: A male common swift after his voyage to Africa and back. During the journey a light logger mounted to his back recording the light intensity.

clock enclosed in a small housing that can be fit to the tarsus or mounted with a harness to the back of the bird. As a rule of thumb, the sensor can weigh at most 5% of a bird's weight. State of the art sensors weigh 2 grams, and thus as small birds as a swift (40g) can be marked. The sensor unit cannot communicate, so this approach hinges on that the birds are caught or found when they die, so the memory can be read off.

The swift is an interesting bird, since it is believed to spend all of its life on the wings, except for the nesting period. This makes the light data particular good, since there is barely any surrounding vegetation that disturb the measurements. Also the migration pattern of the swift is fascinating, since it travels long distances over the seasons, but always returns to basically the same place for mating in the summer. This unique navigation ability is believed to be genetically inherited, and it might have persisted since the last ice age. The swift in Figure 1 is a young male and one of the first marked swift that has been found. The researchers know very little about the migration pattern for swifts during the winter time in Africa, since there are almost no reports from Africa on found species with the classical ring.

The light logger samples light intensity every 5-10 minutes. It is quite a coarse information suffering from saturation at both ends. Thus, it is only the transitions between night and day and *vice versa* that contain information with the current sensor. The theory of geolocation by light levels is described by Hill (1994) for elephant seals, where sensitivity and geometrical relations are discussed in detail. The accuracy of the geolocation is evaluated on different sharks by comparing to a satellite navigation system, and the result is shown to be in the order of 1 degree in longitude and latitude.

If the animal is known to be at rest during the night, the two positions corresponding to sunset and sunrise can be assumed the same, and the unknown longitude and latitude can be solved from the two measurements uniquely. This is the basis for the geolocation software that comes with the sensor. There is an obvious singularity for the two days of equinox when the sun is in the same plane as the equator, and thus the two manifolds in Figure 2 are vertical lines. In praxis 15 days on each side of spring and autumn equinoxes are omitted from analyses (Stutchbury et al., 2009). Another problem occurs if the bird is moving between sunrise and sunset, in which case midday and daylength is shifted slightly causing a bias in the position. This is especially a problem during fast migration flights, when a swift may cover up to 650 km/day (Åkesson et al., 2012).



Figure 2: Binary day-light model for a particular time t . The shape of the dark area depends on the time of the year, and the horizontal position of the dark area depends on the time of the day.

We propose a nonlinear filtering framework, where the sunset and sunrise are treated as separate measurement updates, and an irregularly sampled motion model is used for the time update. This removes the bias problem and also a noise correlation artifact. It also mitigates the singularity at the equinox, where still useful positions can be computed. The motion model has two modes, corresponding to stationary and migrating flight. The filter thus has adaptive sensitivity, giving higher position accuracy at the stationary mode.

Animal geolocation based on light levels can be traced back to at least 1986 (Smith and Goodman, 1986). Other publications such as Wilson et al. (1992); Hill (1994); Ekstrom (2004); Stutchbury et al. (2009) have also studied this problem. However, to the best of the authors knowledge, this is the first time that this applications has been put into a statistical filtering framework using separate measurement updates for sunset and sunrise.

The paper outline is as follows: In Section 2 an appropriate sensor and motion model for this application will be presented and the state estimation algorithm is given in Section 3. The paper is concluded with the results on real world data in Section 4 followed by the conclusions in Section 5.

2 Models

The mathematical framework can be summarized in a state space model with state \mathbf{x}_k , position dependent measurement \mathbf{y}_k , process noise \mathbf{w}_k , and measurement noise \mathbf{e}_k :

$$\mathbf{x}_{k+1} = \mathbf{f}(\mathbf{x}_k) + \mathbf{w}_k, \quad (1a)$$

$$\mathbf{y}_k = \mathbf{h}(\mathbf{x}_k) + \mathbf{e}_k. \quad (1b)$$

The state includes position (x_k, y_k) encoded as longitude x_k and latitude y_k , a velocity (\dot{x}_k, \dot{y}_k) as well as a mode parameter δ_k .

2.1 Sunrise and Sunset Models

Figure 2 shows how the sunset and sunrise, respectively, at each time defines a manifold on earth (Meeus, 1991). A sensor consisting of a light-logger and clock can detect these two events. The bright part of the earth is limited by a great circle orthogonal to the sun at each time as depicted in Figure 4.

The time of the sunrise and sunset can easily be derived when knowing the daylength and the time of the midday. The midday will only depend on the longitude of the observer. At longitude $x_k = 0^\circ$ the midday occurs approximately at 12.00 noon. When going $x = 360^\circ/24 = 15^\circ$ east, the midday occurs one hour earlier at 11.00 a.m (earlier, since the sun rises in the east). This gives the relation

$$h^{\text{midday}}(x_k) = 12 - \frac{1}{15}x_k. \quad (2)$$

Further, the daylength will depend on the latitude of the observer as well as on the time of the year. The relation can be derived by making use of the coordinate transformation from the equatorial coordinate system to the horizontal coordinate system. These coordinate systems are used for mapping positions on the celestial sphere and can thus be utilized for describing the position of the sun.

The horizontal coordinate system uses the observer's local horizon as the fundamental plane and the position of the sun is described with its altitude h above the horizon and its azimuth A measured from the south increasing towards the west, see Figure 3.

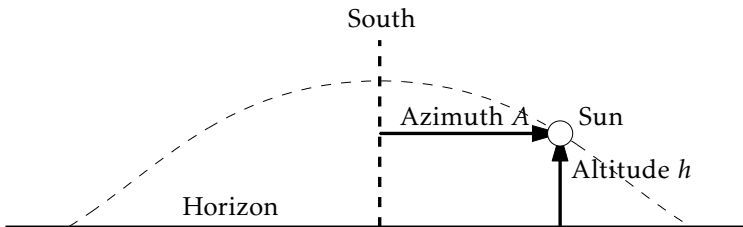


Figure 3: The horizontal coordinate system. The position of the sun is defined with its altitude h and azimuth A .

In the equatorial coordinate system the fundamental plane is defined by the Earth's equator. Here, the position of the sun is described with the local hour angle of the sun H expressed in angular measurement from the solar noon, and the declination of the sun d .

All of these four angles are defined on the celestial sphere (Meeus, 1991; Montenbruck and Pflieger, 1991). However, in this work we are interested in describing the position of the observer on the earth rather than the position of the sun on the celestial sphere. Therefore, in Figure 4, the corresponding angles on the earth are depicted. Here, the altitude h has the interpretation of being the orthogonal distance (measured in degrees) to the great circle separating the bright and dark part of the earth, the local hour angle H is the longitude relative to the solar noon meridian and the declination d is the tilt of the earth's axis towards the sun as well as the latitude where the sun reaches its zenith.

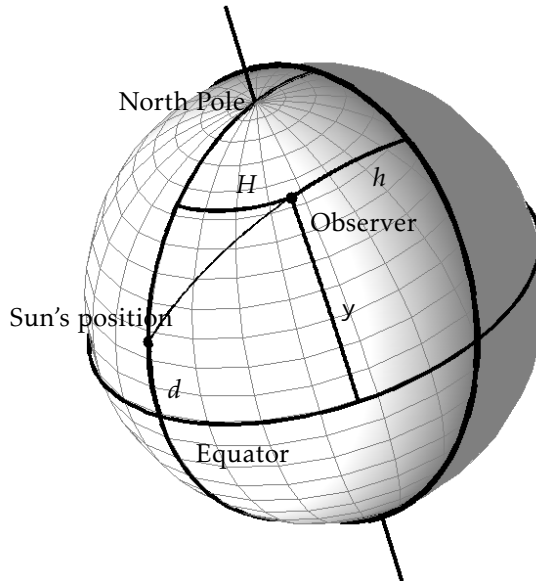


Figure 4: The local hour angle H , declination d and altitude h depicted on the earth, together with the observer's latitude y . Sun's position is the location in the earth where the sun is at its zenith. The geometry of these angles gives the relation (3a).

Following Meeus (1991), these two coordinate systems are related as

$$\sin h = \sin y \sin d + \cos y \cos d \cos H \quad (3a)$$

$$\tan A = \frac{\sin H}{\cos H \sin y - \tan d \cos y}, \quad (3b)$$

where y is the latitude of the observer. The declination of the sun can also be seen

as the angle between the Earth's axis and a line perpendicular to the Earth's orbit. Thus, the declination will change over the year and is given by

$$d(t_k) = -23.439^\circ \cos\left(\frac{360^\circ}{365.25} t_k\right), \quad (4)$$

where t_k is the number of days after the winter solstice. Since a day of 24 hours corresponds to an local hour angle of $H = 360^\circ$, (3a) gives us the relation for the time from a sunrise to the next sunset

$$h^{\text{daylength}}(t_k, y_k) = 2 \frac{24}{360^\circ} \arccos\left(\frac{\sin h_0 - \sin y_k \sin d(t_k)}{\cos y_k \cos d(t_k)}\right). \quad (5)$$

The altitude h_0 is here considered as a constant. It represents the geometrical altitude of the sun at the time apparent rising and setting. Due to atmospheric refraction, these events occur already when the sun geometrically is below the horizon at an altitude of $h_0 = -0^\circ.83$ (Meeus, 1991). Furthermore, the light intensity starts increasing before the sunrise and is still increasing after the event. Noticeable is that the most distinct transition between day and night occurs when the sun is about 6° below the horizon (Hill, 1994). Thus, the altitude h_0 will in practice depend on how the light intensity data is thresholded.

Note that if the argument of arccosine in (5) is larger than 1 in absolute value, the sun will remain either above or below the horizon the whole day.

With this information we can define a measurement model for sunrise and sunset respectively

$$y^{\text{rise}}(t_k) = h^{\text{rise}}(t_k, x_k, y_k) + e_k^{\text{rise}}, \quad (6a)$$

$$y^{\text{set}}(t_l) = h^{\text{set}}(t_l, x_l, y_l) + e_l^{\text{set}}. \quad (6b)$$

where

$$h^{\text{rise}}(t_k, x_k, y_k) = h^{\text{midday}}(x_k) - \frac{h^{\text{daylength}}(t_k, y_k)}{2} \quad (6c)$$

$$h^{\text{set}}(t_l, x_l, y_l) = h^{\text{midday}}(x_l) + \frac{h^{\text{daylength}}(t_l, y_l)}{2} \quad (6d)$$

2.2 Sensor Error Model

The errors $e^{\text{rise}}(t_k)$ and $e^{\text{set}}(t_l)$ for sunrise and sunset, respectively, consist of different kinds of errors:

1. Detection errors from the light logger data. The data in Figure 8 indicates that this error is Gaussian with a standard deviation of slightly more than four minutes. Note that four minutes corresponds to 1 degree, which is 120 km in north-south direction and 120 times cosine of latitude in east-west direction.
2. Position dependent variations. For instance, the days are longer over sea than land (Hill, 1994). We will neglect this error, since the bird appears to

be over land most of the time. It would be no problem to cover this in our framework, though.

3. Also the latitude and time of year may affect the error. This is a subject for future studies.
4. Weather dependent variations, where sunny days are longer than cloudy ones. This can be incorporated by using data from historic weather data bases in our framework, but this is also a subject for future studies.

Note that the errors in sunset and sunrise can be seen as independent, and thus the error in day length and midday are actually correlated.

2.3 Kinematic Model

The kinematic model of migrating birds is characterized by two modes consisting of a *stationary mode* on their breeding, wintering or moulting sites, as well as a *migration mode* (Newton, 2008). In order to describe the transition from the stationary mode to the migration mode a *transition mode* is used. The mode parameter $\delta_k \in \{\text{stationary mode, transition mode, migration mode}\}$ is here modeled as a hidden Markov state with a specified transition probability Π_k resulting in

$$p(\delta_{k+1}|\delta_k) = \Pi_k^{(\delta_{k+1}, \delta_k)}. \quad (7)$$

In Figure 5 the corresponding Markov chain is drawn.

In the stationary mode it is sufficient to model the dynamics of the swift with a *constant position* model, which uses a two dimensional position

$$\mathbf{x}(t) = \begin{pmatrix} x(t) \\ y(t) \end{pmatrix}, \quad \dot{\mathbf{x}}(t) = \begin{pmatrix} w^x(t) \\ w^y(t) \end{pmatrix} \quad (8a)$$

The corresponding discrete time model is given by

$$\mathbf{x}_{k+1} = \begin{pmatrix} 1 & 0 \\ 0 & 1 \end{pmatrix} \mathbf{x}_k + \begin{pmatrix} T & 0 \\ 0 & T \end{pmatrix} \begin{pmatrix} w_k^x \\ w_k^y \end{pmatrix}. \quad (8b)$$

where the input \mathbf{w}_k is considered as random process noise. In the migration mode the velocity of the bird will be of great importance when predicting the next position. This can be captured by using a *constant velocity* model. This is still a fairly simple motion model, yet one of the most common ones in target tracking applications where no inertial measurements are available.

$$\mathbf{x}(t) = \begin{pmatrix} x(t) \\ y(t) \\ \dot{x}(t) \\ \dot{y}(t) \end{pmatrix}, \quad \dot{\mathbf{x}}(t) = \begin{pmatrix} \dot{x}(t) \\ \dot{y}(t) \\ w^x(t) \\ w^y(t) \end{pmatrix} \quad (9a)$$

The corresponding discrete time model is given by

$$\mathbf{x}_{k+1} = \underbrace{\begin{pmatrix} 1 & 0 & T & 0 \\ 0 & 1 & 0 & T \\ 0 & 0 & 1 & 0 \\ 0 & 0 & 0 & 1 \end{pmatrix}}_{=F_{CV}} \mathbf{x}_k + \underbrace{\begin{pmatrix} T^2/2 & 0 \\ 0 & T^2/2 \\ T & 0 \\ 0 & T \end{pmatrix}}_{=G_{CV}} \begin{pmatrix} w_k^x \\ w_k^y \end{pmatrix}. \quad (9b)$$

In a similar manner the constant position model (8b) can be redefined to include the velocity, even though it is not used in the position update

$$\mathbf{x}_{k+1} = \underbrace{\begin{pmatrix} 1 & 0 & 0 & 0 \\ 0 & 1 & 0 & 0 \\ 0 & 0 & 1 & 0 \\ 0 & 0 & 0 & 1 \end{pmatrix}}_{=F_{CP}} \mathbf{x}_k + \underbrace{\begin{pmatrix} T & 0 \\ 0 & T \\ 1 & 0 \\ 0 & 1 \end{pmatrix}}_{=G_{CP}} \begin{pmatrix} w_k^x \\ w_k^y \end{pmatrix}. \quad (10)$$

In order to initialize the velocity correctly during the transition from stationary to migration mode, a third transition mode is used to enlarge the covariance of the position. This mode also uses a constant position model but with a much larger process noise as for the stationary mode.

By modeling the process noise $\mathbf{w}_k \sim \mathcal{N}(0, Q^{\delta_k})$ to be white Gaussian for the all modes, the transition density for \mathbf{x}_k and δ_k can be described as

$$p(\mathbf{x}_{k+1}, \delta_{k+1} | \mathbf{x}_k, \delta_k) = \prod_k^{(\delta_{k+1}, \delta_k)} p(\mathbf{x}_{k+1} | \mathbf{x}_k, \delta_k) \quad (11)$$

where

$$p(\mathbf{x}_{k+1} | \mathbf{x}_k, \delta_k) = \begin{cases} \mathcal{N}(F_{CP}\mathbf{x}_k, G_{CP}Q^sG_{CP}^T), & \delta_k = \text{stationary mode} \\ \mathcal{N}(F_{CP}\mathbf{x}_k, G_{CP}Q^tG_{CP}^T), & \delta_k = \text{transition mode} \\ \mathcal{N}(F_{CV}\mathbf{x}_k, G_{CV}Q^mG_{CV}^T), & \delta_k = \text{migration mode} \end{cases}$$

where Q^s , Q^t and Q^m is the process noise covariance for the three modes. Note that we will choose $Q^t \gg Q^s$ in order to capture the character of the transition mentioned above.

3 State estimation

The nonlinear filtering problem (1) will here be solved using a marginalized particle filter. For this application (including future extensions) this is a sound approach due to many reasons:

- Like any filter, it can handle partial information of the position, so it can process sunrises and sunsets separately.

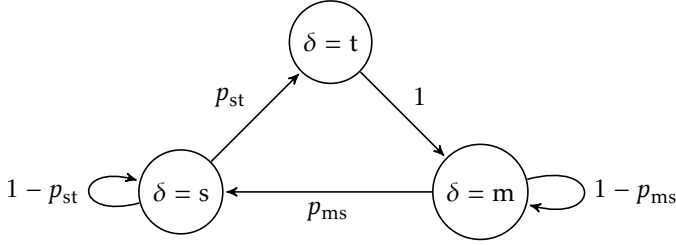


Figure 5: The Markov chain for the mode parameter δ . The mode $\delta = s$ is a the stationary mode, where \mathbf{x}_k constant position model is used, $\delta = m$ corresponds to the migration mode using a constant velocity model, $\delta = t$ corresponds to a transition state from $\delta = s$ to $\delta = m$ where a faster constant position model is used.

- Also like any filter, it can handle multiple modes by running two or more filters in parallel, and fusing their states according to their performance.
- In contrast to other filters, it can handle multiple modes by augmenting the state vector with the mode parameter. This approach will be used in this work.
- The particle filter can handle multi-modal position distributions better than any other filter, which is useful for robust filtering where a lot of outliers in data occur (false and missed detections from the logged light data).
- It can handle position dependent noise, like ground vegetation type and local weather dependent noise distributions.
- It can easily include state constraints, such as maximum speed.

The time update of the position in the particle filter consists here of the following steps:

1. Simulate N noise vectors $\mathbf{w}_k^i \sim \mathcal{N}(0, \mathbf{Q}^{\delta_k})$.
2. Propagate the set of particles according to (10) or (9b) depending on δ_k .

We will here make use of the fact that the sensor model (6) depends on the position and the time only,

$$\mathbf{y}_k = \mathbf{h}(t_k, \mathbf{x}_k, y_k) + \mathbf{e}_k. \quad (12)$$

Since the motion models (10) and (9b) are linear in the state and noise, the marginalized particle filter applies, so the velocity component can be handled in a numerically very efficient way.

Let $\mathbf{r}_k = (x_k, y_k)^\top$ and $\mathbf{v}_k = (\dot{x}_k, \dot{y}_k)^\top$. Then, constant velocity model (9b) and the sensor model (12) can be rewritten as

$$\mathbf{r}_{k+1} = \mathbf{r}_k + T\mathbf{v}_k + \frac{T^2}{2}\mathbf{w}_k, \quad (13a)$$

$$\mathbf{y}_k = \mathbf{h}(t_k, \mathbf{r}_k) + \mathbf{e}_k, \quad (13b)$$

$$\mathbf{v}_{k+1} = \mathbf{v}_k + T\mathbf{w}_k, \quad (13c)$$

$$\mathbf{r}_{k+1} - \mathbf{r}_k = T\mathbf{v}_k + \frac{T^2}{2}\mathbf{w}_k. \quad (13d)$$

We here use the particle filter for (13ab) and the Kalman filter for (13cd). Note that (13ad) are the same two equations, interpreted in two different ways. The time update in the particle filter becomes

$$\mathbf{w}_k^i \sim \mathcal{N}(0, \mathbf{Q}_k), \quad (14a)$$

$$\mathbf{r}_{k+1}^i = \mathbf{r}_k^i + T\mathbf{v}_k^i + \frac{T^2}{2}\mathbf{w}_k^i. \quad (14b)$$

Conversely, we use the position as a measurement in the Kalman filter. For this particular structure, the general result given in Theorem 2.1 in Schön et al. (2005) simplifies a lot, and we get a combined update

$$\hat{\mathbf{v}}_{k+1|k}^i = \frac{\mathbf{r}_{k+1}^i - \mathbf{r}_k^i}{T} \quad (14c)$$

$$\mathbf{P}_{k+1|k} = \mathbf{P}_{k|k-1} - \mathbf{P}_{k|k-1} \left(\mathbf{P}_{k|k-1} + \frac{T^2}{4}\mathbf{Q}_k \right)^{-1} \mathbf{P}_{k|k-1}. \quad (14d)$$

Note that each particle has an individual velocity estimate $\hat{\mathbf{v}}_{k|k-1}^i$ but a common covariance $\mathbf{P}_{k|k-1}$. Further, for a time-invariant $\mathbf{Q}_k = \mathbf{Q}$, the covariance matrix converges quite quickly to $\mathbf{P}_{k|k-1} = 0$, and the Kalman filter is in fact not needed and can be replaced with a deterministic update of the velocity.

In a similar manner we get the same velocity update (14c) when using the constant position model (9b). Note that this velocity update is not needed affect the position if the particle is in δ_k = "stationary mode". However, in the mode δ_k = "transition mode" it is crucial since that velocity will be used in the time update in the next time instance when being in δ_k = "migration mode". The estimation framework is presented in Algorithm 1.

4 Results from Real World Data

The proposed tracking framework has been validated on real world data. This section presents this data as well as the tracking results.

4.1 The data

A light logger was mounted on a swift which was released from the very south of Sweden. Ten months later it was captured again at its own nest and the light logger was removed from the bird. The recorded data consists of light intensity measurements during a period of 298 days from 5th of August 2010 to 29th of May 2011. From this data the universal time of sunrise and sunset has been extracted by thresholding the data on a light level corresponding to a sun altitude of -3.7° , see Fox (2010) for further details on how this has been done. Thus, the

Algorithm 1 Migrating bird tracking using particle filter

Choose number of particles N .

Initialization: Generate $\mathbf{r}_1^i \sim \mathbf{r}_{\mathbf{r}_0}$, $\mathbf{v}_1^i \sim \mathbf{r}_{\mathbf{v}_0}$ and $\delta_1^i \sim \mathbf{r}_{\delta_0}$, $i = 1, \dots, N$, encode the augmented state as $\bar{\mathbf{x}}_1^i = [\mathbf{x}_1^i, \delta_1^i] = [\mathbf{r}_1^i, \mathbf{v}_1^i, \delta_1^i]$, let $\omega_0 = 1/N$ and $k = 1$.

Iteration over the days:

For $t = 1, 2, \dots$

Iteration over sunrise and sunset:

For $m = \{\text{sunrise, sunset}\}$

1. *Measurement update:*

For $i = 1 : N$

$$\omega_k^i = \frac{\omega_{k-1}^i p^m(\mathbf{y}_k | \bar{\mathbf{x}}_k^i, t_k)}{\sum_{j=1}^N \omega_{k-1}^j p^m(\mathbf{y}_k | \bar{\mathbf{x}}_k^j, t_k)} \quad (15)$$

where $\mathbf{y}_k = y^m(t)$ is the time of sunrise/sunset at day t , measured in hours, and $t_k = t + \mathbf{y}_k/24$ is the time, measured in days.

2. *Estimation:* The state and covariance is estimated by

$$\hat{\mathbf{x}}_k = \sum_{i=1}^N \omega_k^i \mathbf{x}_k^i \quad (16)$$

$$\hat{\mathbf{P}}_k = \sum_{i=1}^N \omega_k^i (\mathbf{x}_k^i - \hat{\mathbf{x}}_k)(\mathbf{x}_k^i - \hat{\mathbf{x}}_k)^\top \quad (17)$$

3. *Resample:* Take N samples with replacement from the set $\{\bar{\mathbf{x}}_k^i\}_{i=1}^N$ where the probability to take sample i is ω_k^i and let $\omega_k^i = 1/N$.

4. *Time update:*

Compute the sampling interval:

$$T_k = t_k - t_{k-1}$$

For $i = 1 : N$

For each part of the state vector $\bar{\mathbf{x}}_k^i = [\mathbf{r}_k^i, \mathbf{v}_k^i, \delta_k^i]$ do the following:

(a) Generate predictions of the position depending on the mode

$$\mathbf{w}_k^i \sim \mathcal{N}(0, \mathbf{Q}^{\delta_k^i})$$

If $\delta_k^i = \text{"stationary mode"}$ **or** $\delta_k^i = \text{"transition mode"}$

$$\mathbf{r}_{k+1}^i = \mathbf{r}_k^i + T_k \mathbf{w}_k^i$$

elseif $\delta_k^i = \text{"migration mode"}$

$$\mathbf{r}_{k+1}^i = \mathbf{r}_k^i + T_k \mathbf{v}_k^i + \frac{T_k^2}{2} \mathbf{w}_k^i$$

(b) Generate predictions of the mode

$$\delta_{k+1}^i \sim p(\delta_{k+1}^i | \delta_k^i)$$

(c) Generate predictions of the velocity

$$\mathbf{v}_{k+1}^i = \frac{\mathbf{r}_{k+1}^i - \mathbf{r}_k^i}{T_k}$$

5. Set $k := k + 1$

preprocessed data consists of the universal time of 298 sunrises and 298 sunsets as depicted in Figure 6.

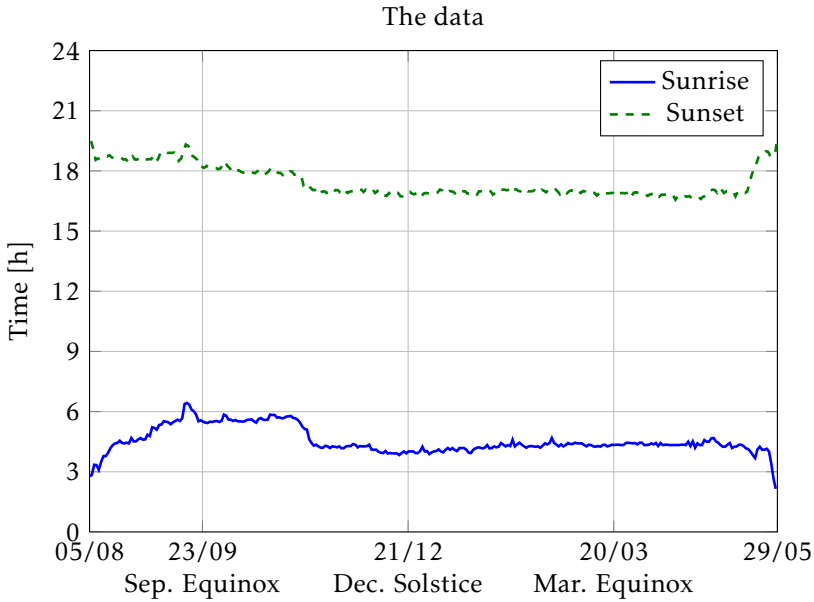


Figure 6: Universal time of the sunrise and the sunset during the 10 months journey of the swift

From this information the daylength and midday can easily be extracted as presented in Figure 7. The state of the art algorithm is to use this information to convert to longitude and latitude using (2) and (5). However, with Algorithm 1 we propose to use time of sunrise and sunset to prevent the bias that would occur in fast day transitions.

From the data in Figure 6 the variance of the measurement noise can be estimated. During the period from the 10th of December to the 25th of April the data is fairly constant. (As we later will see in Figure 9 this corresponds to when the swift is at its wintering site in Africa.) This data has been detrended and is visualized as a histograms in Figure 8 for sunrise and sunset, respectively. From this data the standard deviation of the measurement noise can be estimated to approximately 5 minutes for both sunrise and sunset.

4.2 Results

Algorithm 1 using $N = 500$ particles has been implemented and evaluated on the data presented in Figure 6. For the mode parameter δ_k the Markov chain in Figure 5 has been used with the transition probabilities

$$p_{st} = p(\delta_{k+1} = \text{stat. m.} | \delta_k = \text{trans. m.}) = 0.2 \quad (18a)$$

$$p_{ms} = p(\delta_{k+1} = \text{mig. m.} | \delta_k = \text{stat. m.}) = 0.05 \quad (18b)$$

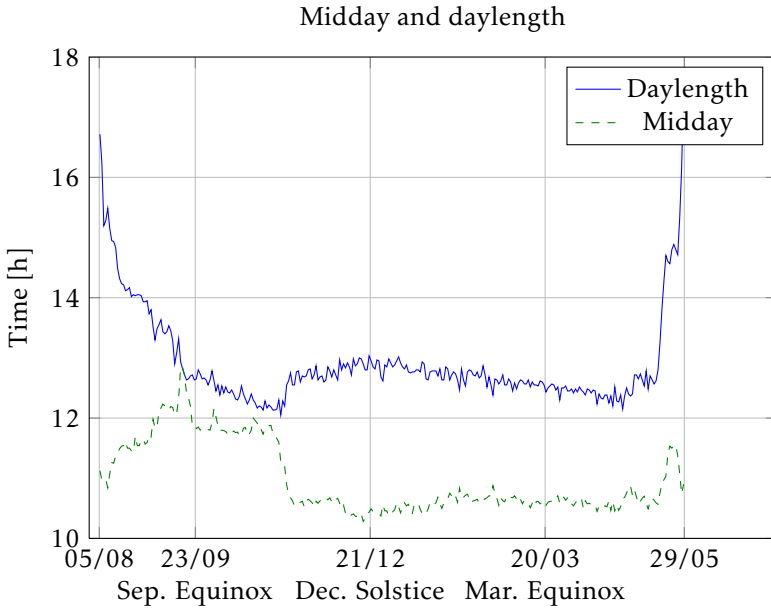


Figure 7: The daylength and the time of the midday during the 10 months journey of the swift.

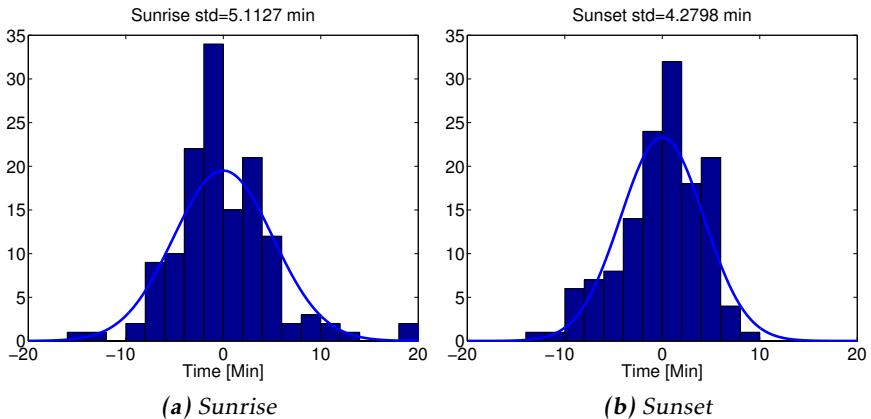


Figure 8: Histograms for the detrended sunrise and sunset measurements from the 10th of December to the 25th of April together with a Gaussian approximation.

and

$$Q^{\delta_k=\text{stat. mode}} = 1^2 \cdot I_2 \quad (19a)$$

$$Q^{\delta_k=\text{trans. mode}} = 10^2 \cdot I_2 \quad (19b)$$

$$Q^{\delta_k=\text{mig. mode}} = 2^2 \cdot I_2 \quad (19c)$$

Furthermore, according to Figure 8, the measurement noise has a standard deviation of approximately 5 minutes. However, in order to compensate for modeling errors, a standard deviation of 10 minutes has been used in the filter

$$e^{\text{set}} \sim \mathcal{N}(0, (10/60)^2), \quad e^{\text{rise}} \sim \mathcal{N}(0, (10/60)^2). \quad (20)$$

Finally, a sun altitude of $h_0 = -3.7^\circ$ has been chosen in accordance with how the light intensity data has been thresholded, see Section 4.1.

The tracking performance is presented in Figure 9. The tracking result will also be compared with a non-filtering solution where we assume that the bird has not moved during the period from sunset to sunrise. Then, by using (6) and assuming $(x_k, y_k) = (x_l, y_l)$ the longitude and latitude can be solved uniquely each day separately. By using inverse mapping we also get a corresponding covariance

$$\mathbf{x}_k = \mathbf{h}^{-1}(\mathbf{y}_k)$$

$$\text{Cov}(\mathbf{x}_k) = \left(\nabla \mathbf{h}^\top(\mathbf{x}_k) R^{-1} \nabla \mathbf{h}(\mathbf{x}_k) \right)^{-1}$$

where

$$\mathbf{h} = \begin{pmatrix} h^{\text{sunrise}} \\ h^{\text{sunset}} \end{pmatrix}, \quad \mathbf{y}_k = \begin{pmatrix} y^{\text{sunrise}}(t_k) \\ y^{\text{sunset}}(t_k) \end{pmatrix} \quad \text{and} \quad \mathbf{x}_k = \begin{pmatrix} x_k \\ y_k \end{pmatrix}.$$

In Figure 10 the estimated position for the two methods is presented with a 90% confidence interval together with the estimated mode parameter from the particle filter implementation.

In Figure 11 two periods are zoomed in order to point out the differences between the two methods. According to Figure 11a, the particle filter implementation manages to mitigate the singularity due to the September equinox. The variance is still increasing for the particle filter implementation, however not as much as for the inverse mapping method. This is mainly due to the fact that we use a motion model.

As explained earlier, fast transitions in east-west direction will give rise to shorter or longer measured daylength. This will lead to a bias in the latitude estimation using the inverse mapping method since it wrongly assumes that the light logger measures the sunrise and sunset at the same position. In Figure 11b such a bias for the latitude can be seen during a period around May where the swift is making a fast transition from Africa back to Europe. The movement in west direction will make the measured daylength longer than the actual daylength at the corresponding latitude. For the inverse mapping method this will give a bias

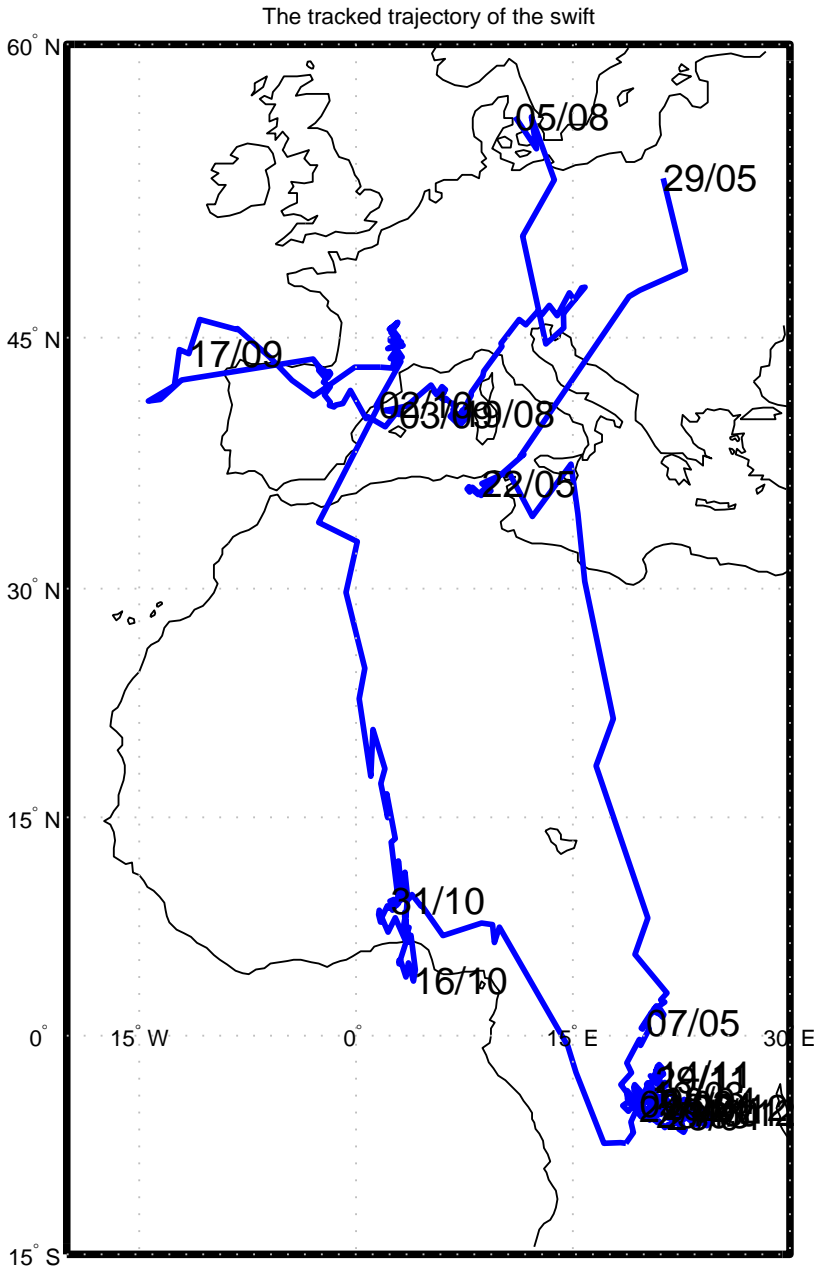


Figure 9: The trajectory of the swift during a period of 298 days. The positions are estimated at each sunrise and sunset.

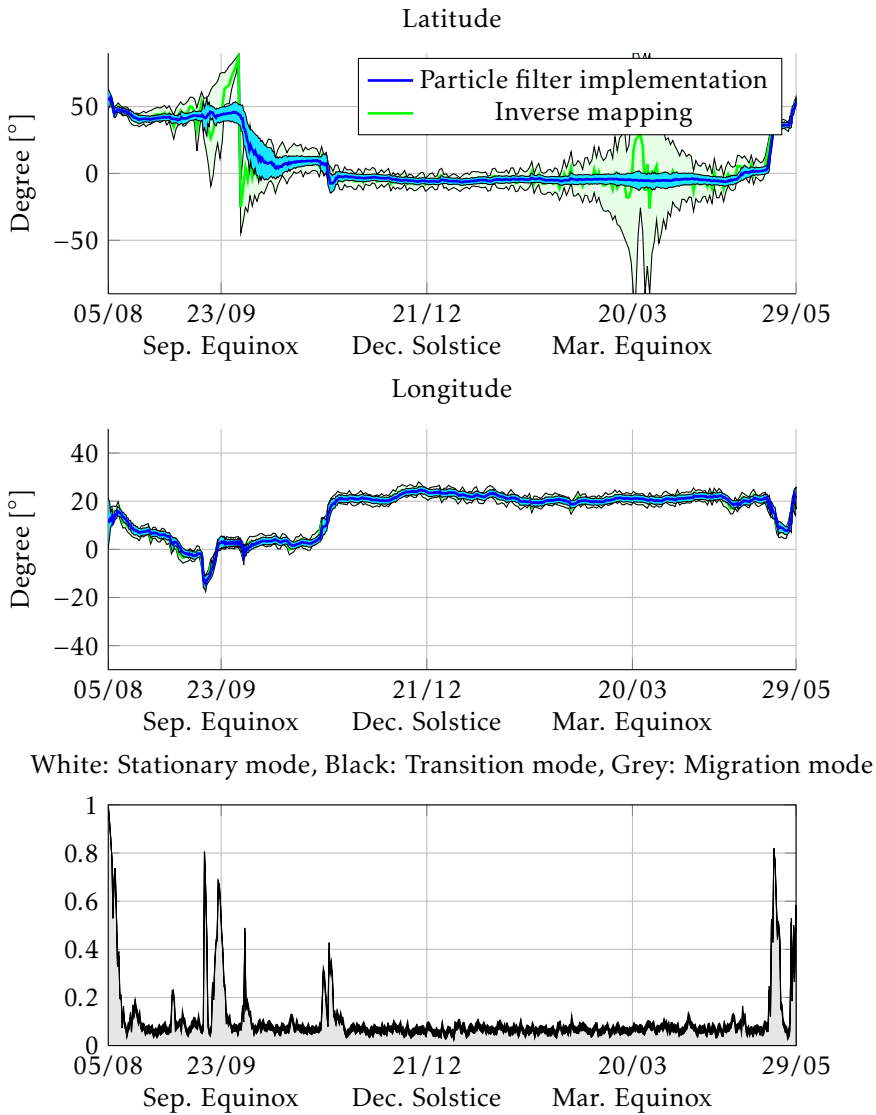


Figure 10: The estimated position and mode of the swift during a period of 298 days. The presented particle filter implementation is here compared with using inverse mapping. The estimates are presented with a 90% confidence interval.

towards north since the daylength is longer on the northern hemisphere during the summer.

Finally in Figure 12 the trajectories for the particle filter implementation is presented together with covariance ellipses representing the estimation uncertainty. Here also the position of the start and end point of the journey is depicted.

5 Conclusion and Future Work

In this paper, a particle filter solution has been presented estimating the trajectory of a migrating bird using light logger data. A sensor model has been presented based on astronomical formulas consisting of a measurement update at sunrise and sunset respectively, and a suitable motion describing the flying pattern of migrating birds. The implementation has been validated on real data and compared with the state of the art algorithm based on a purely deterministic approach. The proposed solution outperforms the existing method in reliability during the equinoxes and removes problem with bias due to fast day transitions. In addition, the proposed method provides an estimate of the migration mode suitable for further analysis of the flying pattern of the bird. In the future, the framework will be extended to process the light intensity data directly as well as including position and weather dependent noise and bias.

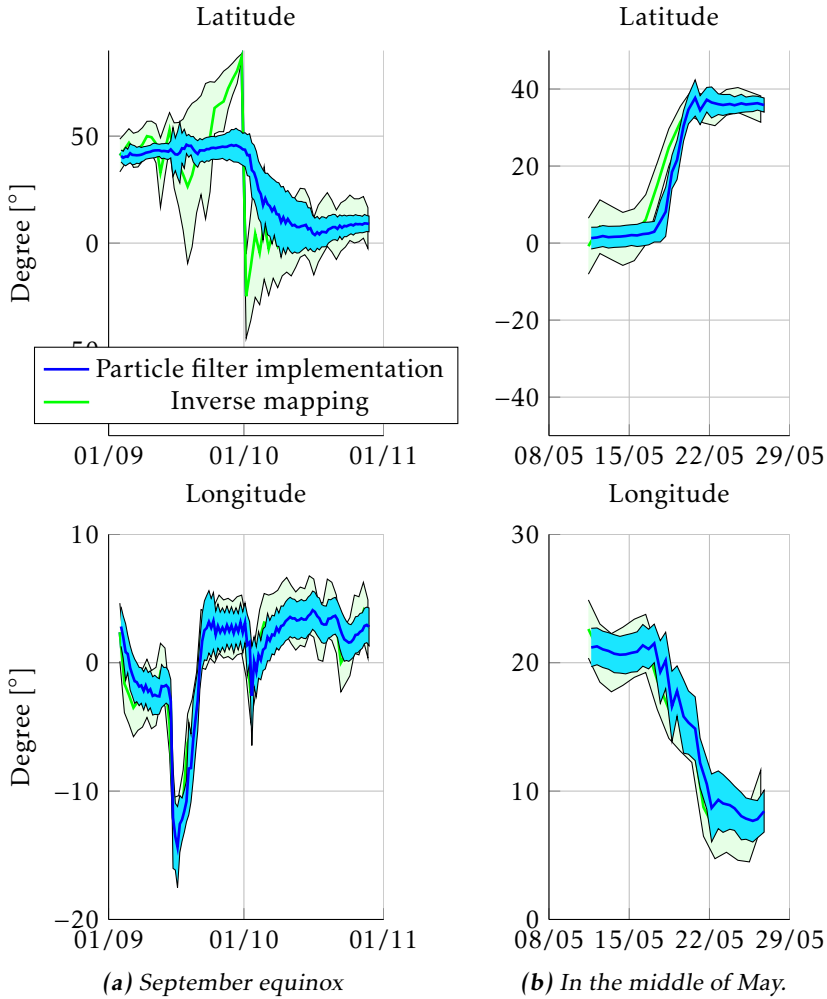


Figure 11: The estimated position of the swift during a month around the fall equinox when the swift is migrating from Europe to the east of Africa as well as two weeks in the middle of May. The presented particle filter implementation (blue) is here compared with using inverse mapping (green). The estimates are presented with a 90% confidence interval.

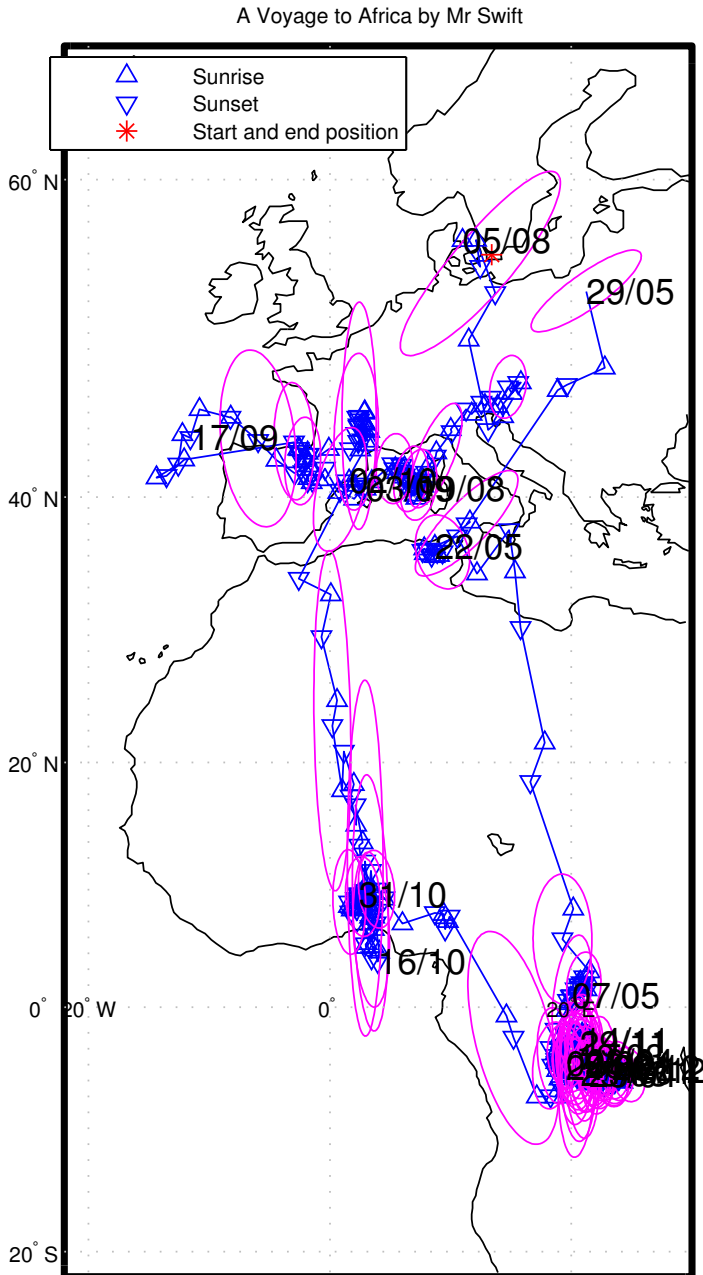


Figure 12: The trajectory of the swift during a period of 298 days. The positions are estimated at each sunrise and sunset. At every 5th day, the accuracy of position estimate is visualized together with a 90% confidence interval.

Bibliography

- S. Åkesson, R. Klaassen, J. Holmgren, J. W. Fox, and A. Hedenström. Migration Route and Strategies in a Highly Aerial Migrant, the Common Swift *Apus apus*, Revealed by Light-Level Geolocators. *Plos One*, 7(7), 2012.
- P.A. Ekstrom. An advance in geolocation by light. *Memoirs of the National Institute of Polar Research*, 58:210–226, 2004.
- J. Fox. Geocator manual, 2010.
- R.D. Hill. Theory of geolocation by light levels. In *Elephant seals: population ecology, behavior, and physiology*. University of California Press, Berkeley, pages 227–236. University of California Press, 1994.
- J.H. Meeus. *Astronomical algorithms*. Willmann-Bell, Incorporated, 1991.
- O. Montenbruck and T. Pflieger. *Astronomy on the personal computer*, volume 1. Springer Verlag, 1991.
- I. Newton. *The migration ecology of birds*. Academic Pr, 2008.
- T. Schön, F. Gustafsson, and P.-J. Nordlund. Marginalized particle filters for mixed linear/nonlinear state-space models. *IEEE Transactions on Signal Processing*, 53(7):2279–2289, July 2005.
- P. Smith and D. Goodman. Determining fish movements from an "archival" tag: Precision of geographical positions made from a time series of swimming temperature and depth. Technical report, US National Oceanic and Atmospheric Administration, 1986.
- B.J.M. Stutchbury, S.A. Tarof, T. Done, E. Gow, P.M. Kramer, J. Tautin, J.W. Fox, and V. Afanasyev. Tracking long-distance songbird migration by using geolocators. *Science*, 323(5916):896, 2009.
- N. Wahlström, F. Gustafsson, and S. Åkesson. A Voyage to Africa by Mr Swift. In *Proceedings of the 15th International Conference on Information Fusion (FUSION)*, pages 808–815, Singapore, July 2012.
- R.P. Wilson, J.J. Ducamp, W.G. Rees, B.M. Culik, and K. Niekamp. Estimation of location: global coverage using light intensity. *Wildlife telemetry: Remote monitoring and tracking of animals*, pages 131–134, 1992.

Licentiate Theses
Division of Automatic Control
Linköping University

- P. Andersson:** Adaptive Forgetting through Multiple Models and Adaptive Control of Car Dynamics. Thesis No. 15, 1983.
- B. Wahlberg:** On Model Simplification in System Identification. Thesis No. 47, 1985.
- A. Isaksson:** Identification of Time Varying Systems and Applications of System Identification to Signal Processing. Thesis No. 75, 1986.
- G. Malmberg:** A Study of Adaptive Control Missiles. Thesis No. 76, 1986.
- S. Gunnarsson:** On the Mean Square Error of Transfer Function Estimates with Applications to Control. Thesis No. 90, 1986.
- M. Viberg:** On the Adaptive Array Problem. Thesis No. 117, 1987.
- K. Ståhl:** On the Frequency Domain Analysis of Nonlinear Systems. Thesis No. 137, 1988.
- A. Skeppstedt:** Construction of Composite Models from Large Data-Sets. Thesis No. 149, 1988.
- P. A. J. Nagy:** MaMiS: A Programming Environment for Numeric/Symbolic Data Processing. Thesis No. 153, 1988.
- K. Forsman:** Applications of Constructive Algebra to Control Problems. Thesis No. 231, 1990.
- I. Klein:** Planning for a Class of Sequential Control Problems. Thesis No. 234, 1990.
- F. Gustafsson:** Optimal Segmentation of Linear Regression Parameters. Thesis No. 246, 1990.
- H. Hjalmarsson:** On Estimation of Model Quality in System Identification. Thesis No. 251, 1990.
- S. Andersson:** Sensor Array Processing; Application to Mobile Communication Systems and Dimension Reduction. Thesis No. 255, 1990.
- K. Wang Chen:** Observability and Invertibility of Nonlinear Systems: A Differential Algebraic Approach. Thesis No. 282, 1991.
- J. Sjöberg:** Regularization Issues in Neural Network Models of Dynamical Systems. Thesis No. 366, 1993.
- P. Pucar:** Segmentation of Laser Range Radar Images Using Hidden Markov Field Models. Thesis No. 403, 1993.
- H. Fortell:** Volterra and Algebraic Approaches to the Zero Dynamics. Thesis No. 438, 1994.
- T. McKelvey:** On State-Space Models in System Identification. Thesis No. 447, 1994.
- T. Andersson:** Concepts and Algorithms for Non-Linear System Identifiability. Thesis No. 448, 1994.
- P. Lindskog:** Algorithms and Tools for System Identification Using Prior Knowledge. Thesis No. 456, 1994.
- J. Plantin:** Algebraic Methods for Verification and Control of Discrete Event Dynamic Systems. Thesis No. 501, 1995.
- J. Gunnarsson:** On Modeling of Discrete Event Dynamic Systems, Using Symbolic Algebraic Methods. Thesis No. 502, 1995.
- A. Ericsson:** Fast Power Control to Counteract Rayleigh Fading in Cellular Radio Systems. Thesis No. 527, 1995.
- M. Jirstrand:** Algebraic Methods for Modeling and Design in Control. Thesis No. 540, 1996.
- K. Edström:** Simulation of Mode Switching Systems Using Switched Bond Graphs. Thesis No. 586, 1996.

J. Palmqvist: On Integrity Monitoring of Integrated Navigation Systems. Thesis No. 600, 1997.

A. Stenman: Just-in-Time Models with Applications to Dynamical Systems. Thesis No. 601, 1997.

M. Andersson: Experimental Design and Updating of Finite Element Models. Thesis No. 611, 1997.

U. Forssell: Properties and Usage of Closed-Loop Identification Methods. Thesis No. 641, 1997.

M. Larsson: On Modeling and Diagnosis of Discrete Event Dynamic systems. Thesis No. 648, 1997.

N. Bergman: Bayesian Inference in Terrain Navigation. Thesis No. 649, 1997.

V. Einarsson: On Verification of Switched Systems Using Abstractions. Thesis No. 705, 1998.

J. Blom, F. Gunnarsson: Power Control in Cellular Radio Systems. Thesis No. 706, 1998.

P. Spångéus: Hybrid Control using LP and LMI methods – Some Applications. Thesis No. 724, 1998.

M. Norrlöf: On Analysis and Implementation of Iterative Learning Control. Thesis No. 727, 1998.

A. Hagenblad: Aspects of the Identification of Wiener Models. Thesis No. 793, 1999.

E. Tjärnström: Quality Estimation of Approximate Models. Thesis No. 810, 2000.

C. Carlsson: Vehicle Size and Orientation Estimation Using Geometric Fitting. Thesis No. 840, 2000.

J. Löfberg: Linear Model Predictive Control: Stability and Robustness. Thesis No. 866, 2001.

O. Härkegård: Flight Control Design Using Backstepping. Thesis No. 875, 2001.

J. Elbornsson: Equalization of Distortion in A/D Converters. Thesis No. 883, 2001.

J. Roll: Robust Verification and Identification of Piecewise Affine Systems. Thesis No. 899, 2001.

I. Lind: Regressor Selection in System Identification using ANOVA. Thesis No. 921, 2001.

R. Karlsson: Simulation Based Methods for Target Tracking. Thesis No. 930, 2002.

P.-J. Nordlund: Sequential Monte Carlo Filters and Integrated Navigation. Thesis No. 945, 2002.

M. Östring: Identification, Diagnosis, and Control of a Flexible Robot Arm. Thesis No. 948, 2002.

C. Olsson: Active Engine Vibration Isolation using Feedback Control. Thesis No. 968, 2002.

J. Jansson: Tracking and Decision Making for Automotive Collision Avoidance. Thesis No. 965, 2002.

N. Persson: Event Based Sampling with Application to Spectral Estimation. Thesis No. 981, 2002.

D. Lindgren: Subspace Selection Techniques for Classification Problems. Thesis No. 995, 2002.

E. Geijer Lundin: Uplink Load in CDMA Cellular Systems. Thesis No. 1045, 2003.

M. Enqvist: Some Results on Linear Models of Nonlinear Systems. Thesis No. 1046, 2003.

T. Schön: On Computational Methods for Nonlinear Estimation. Thesis No. 1047, 2003.

F. Gunnarsson: On Modeling and Control of Network Queue Dynamics. Thesis No. 1048, 2003.

S. Björklund: A Survey and Comparison of Time-Delay Estimation Methods in Linear Systems. Thesis No. 1061, 2003.

M. Gerdin: Parameter Estimation in Linear Descriptor Systems. Thesis No. 1085, 2004.

A. Eidehall: An Automotive Lane Guidance System. Thesis No. 1122, 2004.

E. Wernholt: On Multivariable and Nonlinear Identification of Industrial Robots. Thesis No. 1131, 2004.

J. Gillberg: Methods for Frequency Domain Estimation of Continuous-Time Models. Thesis No. 1133, 2004.

G. Hendeby: Fundamental Estimation and Detection Limits in Linear Non-Gaussian Systems. Thesis No. 1199, 2005.

D. Axehill: Applications of Integer Quadratic Programming in Control and Communication. Thesis No. 1218, 2005.

J. Sjöberg: Some Results On Optimal Control for Nonlinear Descriptor Systems. Thesis No. 1227, 2006.

D. Törnqvist: Statistical Fault Detection with Applications to IMU Disturbances. Thesis No. 1258, 2006.

H. Tedefelt: Structural algorithms and perturbations in differential-algebraic equations. Thesis No. 1318, 2007.

S. Moberg: On Modeling and Control of Flexible Manipulators. Thesis No. 1336, 2007.

J. Wallén: On Kinematic Modelling and Iterative Learning Control of Industrial Robots. Thesis No. 1343, 2008.

J. Harju Johansson: A Structure Utilizing Inexact Primal-Dual Interior-Point Method for Analysis of Linear Differential Inclusions. Thesis No. 1367, 2008.

J. D. Hol: Pose Estimation and Calibration Algorithms for Vision and Inertial Sensors. Thesis No. 1370, 2008.

H. Ohlsson: Regression on Manifolds with Implications for System Identification. Thesis No. 1382, 2008.

D. Ankelhed: On low order controller synthesis using rational constraints. Thesis No. 1398, 2009.

P. Skoglar: Planning Methods for Aerial Exploration and Ground Target Tracking. Thesis No. 1420, 2009.

C. Lundquist: Automotive Sensor Fusion for Situation Awareness. Thesis No. 1422, 2009.

C. Lyzell: Initialization Methods for System Identification. Thesis No. 1426, 2009.

R. Falkeborn: Structure exploitation in semidefinite programming for control. Thesis No. 1430, 2010.

D. Petersson: Nonlinear Optimization Approaches to \mathcal{H}_2 -Norm Based LPV Modelling and Control. Thesis No. 1453, 2010.

Z. Sjanic: Navigation and SAR Auto-focusing in a Sensor Fusion Framework. Thesis No. 1464, 2011.

K. Granström: Loop detection and extended target tracking using laser data. Thesis No. 1465, 2011.

J. Callmer: Topics in Localization and Mapping. Thesis No. 1489, 2011.

F. Lindsten: Rao-Blackwellised particle methods for inference and identification. Thesis No. 1480, 2011.

M. Skoglund: Visual Inertial Navigation and Calibration. Thesis No. 1500, 2011.

S. Khoshfetrat Pakazad: Topics in Robustness Analysis. Thesis No. 1512, 2011.

P. Axelsson: On Sensor Fusion Applied to Industrial Manipulators. Thesis No. 1511, 2011.

A. Carvalho Bittencourt: On Modeling and Diagnosis of Friction and Wear in Industrial Robots. Thesis No. 1516, 2012.

P. Rosander: Averaging level control in the presence of frequent inlet flow upsets. Thesis No. 1527, 2012.